Retroreflex Ellipsometry for Nonplanar Surfaces

Zur Erlangung des akademischen Grades eines

Doktors der Ingenieurwissenschaften

von der KIT-Fakultät für Informatik
des Karlsruher Instituts für Technologie (KIT)

genehmigte

Dissertation

von

M.Sc.

Chia-Wei Chen

aus Taipei City, Taiwan

Tag der mündlichen Prüfung:	11.01.2024
Erster Gutachter:	Prof. Dr.-Ing. habil. Jürgen Beyerer
Zweiter Gutachter:	Prof. Dr.-Ing. habil. Andreas Fischer

Abstract

Objects with physical properties that must be tightly controlled (e.g., dimensions, transmittance, reflectance and concentrations) are common in industrial production processes in the automobile, semiconductor and biological industries. An industrial measurement system for quality assurance must feature high precision and accuracy to allow 100 percent control over the properties of objects for the manufacturing process. Ellipsometry is a reliable and very sensitive method for characterizing materials and thin films. It features high precision and sensitivity and allows nondestructive measurement for process monitoring of optical elements, displays and semiconductors. Ellipsometry uses the changes in polarization when polarized light is reflected (or transmitted) from a sample at an oblique (or normal) angle of incidence (AOI).

Measurements with conventional ellipsometers are only possible on plane surfaces or plane surface elements (with respect to the size of the measurement beam). A signal is only detected if the angle and height of the polarization state generator (PSG) and polarization state analyzer (PSA) in relation to the surface normals are aligned in such a way that they comply with the laws of reflection. Even slight misalignments from the ideal reflection or transmission settings can result in significant experimental errors. For larger misalignments, it is not possible to generate any meaningful signals. For nonplanar samples, the curvature of the surface alters the AOI and the vertical position of the reflected light, so the ideal reflection condition for the ellipsometer cannot be achieved. The angle settings for the PSG and the PSA must be very precisely adjusted relative to the surface normals. The height of the surface relative to the optical components must also be adjusted very accurately. These conditions are necessary for ellipsometry measurements. Nonplanar samples must be adjusted to allow the PSA to receive a sufficient

signal. The process of the alignment and adjustment for the ellipsometer and sample is time-consuming. Therefore, inline inspection of curved surfaces is almost impossible using a standard ellipsometry configuration. However, many applications require quality monitoring or characterization for nonplanar surfaces.

To overcome the geometric limitation, retroreflex ellipsometry is proposed for nonplanar surfaces, including a prototype, polarization ray tracing and two analysis methods for two-phase and three-phase systems. The retroreflex ellipsometer measures Mueller matrices for nonplanar surfaces. This uses the concept of the retroreflector, which returns the light beam from the sample on the same beam path with a fixed phase difference of 180°. The polarization effect is the same as that for an ideal mirror within an angular range of approximately ±30°. For optically isotropic two-phase systems (ambient/ substrate), the proposed ellipsometer simultaneously measures the AOI, the tilt angle and the refractive index with calibrated reflectance values. For optically isotropic three-phase systems (ambient/ thin film/ substrate), the system measures the AOI, the tilt angle and the film thickness using the refractive indices of the film and substrate.

In order to verify the proposed method and the retroreflex ellipsometer, several experiments are conducted. The accuracy and precision of the retroreflex ellipsometer are determined using straight-through measurements in air and a reference sample. The refractive index of an off-axis parabolic mirror is measured and the result is compared with that of a commercial ellipsometer. The film thickness of a protected gold-coated concave mirror is measured and the results are compared with those of a commercial ellipsometer. The surface of the concave mirror is reconstructed using calculated angles of incidence and tilt.

Overall, retroreflex ellipsometry addresses the geometric restrictions of conventional ellipsometry, whereupon samples are no longer limited to flat surfaces. Hence, ellipsometric measurements can be used comprehensively for many industrial production processes for the first time, e.g., the characterization of optical properties of freeform optics and defect inspection for samples with almost arbitrary shapes. Retroreflex ellipsometry has high flexibility for

different shapes of surfaces and the complexity of the system is simple. Moreover, it has great potential for use inline and in situ quality control systems because of the large acceptable angular range for the reflection or refraction of beams at the sample.

Kurzfassung

Objekte mit physikalischen Eigenschaften, die streng kontrolliert werden müssen (z. B. Abmessungen, Transmissionsgrad, Reflexionsgrad und Konzentrationen), sind in industriellen Produktionsprozessen wie in der Automobil-, Halbleiter- und Bioindustrie üblich. Ein industrielles Messsystem für die Qualitätssicherung muss eine hohe Präzision und Genauigkeit aufweisen, um eine hochgenaue Kontrolle der Eigenschaften der Objekte für den Herstellungsprozess zu ermöglichen. Die Ellipsometrie ist eine zuverlässige und sehr empfindliche Methode zur Charakterisierung von Materialien und dünnen Schichten. Sie zeichnet sich durch hohe Präzision und Empfindlichkeit aus und ermöglicht zerstörungsfreie Messungen zur Prozessüberwachung von optischen Elementen, Displays und Halbleitern. Die Ellipsometrie nutzt die Änderungen der Polarisation, wenn polarisiertes Licht von einer Probe unter einem schrägen (oder normalen) Einfallswinkel (AOI) reflektiert (oder durchgelassen) wird.

Messungen mit herkömmlichen Ellipsometern sind nur an ebenen Flächen oder ebenen Flächenelementen (bezogen auf die Größe des Messstrahls) möglich. Ein Signal wird nur dann erkannt, wenn Winkel und Höhe des Polarisationszustandsgenerators (PSG) und des Polarisationszustandsanalysators (PSA) in Bezug auf die Oberflächennormalen so ausgerichtet sind, dass sie den Gesetzen der Reflexion entsprechen. Schon geringe Abweichungen von den idealen Reflexions- oder Transmissionseinstellungen können zu erheblichen Messfehlern führen. Bei größeren Ausrichtungsfehlern ist es nicht möglich, aussagekräftige Signale zu erzeugen. Bei nicht ebenen Proben verändert die Krümmung der Oberfläche den AOI und die vertikale Position des reflektierten Lichts, so dass die ideale Reflexionsbedingung für das Ellipsometer nicht erreicht werden kann. Die Winkeleinstellungen für das PSG und

das PSA müssen sehr genau auf die Oberflächennormalen abgestimmt werden. Auch die Höhe der Oberfläche relativ zu den optischen Komponenten muss sehr genau eingestellt werden. Diese Bedingungen sind für ellipsometrische Messungen erforderlich. Nicht planare Proben müssen justiert werden, damit die PSA ein ausreichendes Signal empfangen kann. Der Prozess der Ausrichtung und Justierung von Ellipsometer und Probe ist zeitaufwändig. Daher ist die Inline-Inspektion gekrümmter Oberflächen mit einer Standard-Ellipsometriekonfiguration fast unmöglich. Viele Anwendungen erfordern jedoch eine Qualitätsüberwachung oder Charakterisierung von nicht ebenen Oberflächen.

Zur Überwindung der geometrischen Beschränkung wird die Retroreflex-Ellipsometrie für nichtplanare Oberflächen vorgeschlagen, einschließlich eines Prototyps, Polarisationsstrahlverfolgung und zwei Analysemethoden für zwei- und dreiphasige Systeme. Das Retroreflex-Ellipsometer misst Mueller-Matrizen für nichtplanare Oberflächen. Dabei wird das Konzept des Retroreflektors verwendet, der den Lichtstrahl von der Probe auf demselben Strahlengang mit einer festen Phasendifferenz von 180° zurückwirft. Der Polarisationseffekt ist derselbe wie bei einem idealen Spiegel innerhalb eines Winkelbereichs von etwa 30°. Für optisch isotrope Zweiphasensysteme (Umgebung/Substrat) misst das vorgeschlagene Ellipsometer gleichzeitig den AOI, den Neigungswinkel und den Brechungsindex mit kalibrierten Reflexionswerten. Bei optisch isotropen Dreiphasensystemen (Umgebung/Dünnschicht/Substrat) misst das System den AOI, den Kippwinkel und die Schichtdicke unter Verwendung der Brechungsindizes von Schicht und Substrat.

Insgesamt überwindet die Retroreflex-Ellipsometrie die geometrischen Einschränkungen der konventionellen Ellipsometrie, wodurch die Proben nicht mehr auf ebene Flächen beschränkt sind. Damit können ellipsometrische Messungen erstmals umfassend für viele industrielle Produktionsprozesse genutzt werden, z.B. zur Charakterisierung der optischen Eigenschaften von Freiformoptiken und zur Defektkontrolle bei nahezu beliebig geformten Proben. Die Retroreflex-Ellipsometrie hat eine hohe Flexibilität für unterschiedliche Oberflächenformen und die Komplexität des Systems ist gering. Darüber hinaus

bietet sie aufgrund des großen zulässigen Winkelbereichs für die Reflexion oder Brechung der Strahlen an der Probe ein großes Potenzial für den Einsatz in Inline- und In-situ-Qualitätskontrollsystemen.

Acknowledgements

I would like to express my sincere gratitude to Prof. Dr.-Ing. habil. Jürgen Beyerer for providing me with the opportunity to work under his guidance and supervision at the Vision and Fusion Laboratory (IES) of the Karlsruhe Institute of Technology (KIT) in cooperation with the Fraunhofer Institute of Optronics, System Technologies and Image Exploitation IOSB. His unwavering support and insightful feedback were invaluable at every stage of my research. This doctoral thesis would not have been achievable without his constant encouragement and support. I would also like to extend my heartfelt thanks to Prof. Dr.-Ing. habil. Andreas Fischer from the Bremen Institute for Metrology, Automation and Quality Science (BIMAQ) of the University of Bremen for serving as the second reviewer and for his valuable comments and suggestions, which significantly enriched my thesis.

Furthermore, I would like to express my special thanks to Matthias Hartrumpf for his extensive experience and constructive advice, which guided my research from ideas into practice. Big thanks are given to my colleagues at the Visual Inspection Systems department (SPR, Fraunhofer IOSB), particularly Prof. Dr.-Ing. habil. Thomas Längle, for providing support and an excellent working environment. I am also grateful to all the members at IES for the fruitful discussions and all the interesting moments in these years. Moreover, to everyone who has been a part of my journey, thank you for your encouragement and support.

Last but not least, I would like to thank my family for giving me their unconditional love and support throughout my life. Without their unconditional dedication, I could not accomplish this work.

Karlsruhe, January 2024 *Chia-Wei Chen*

Contents

Notation

This chapter introduces the notation and symbols which are used in this thesis.

General notation

Scalars	italic Roman letters	x, X
	italic Greek letters	α, Ψ
Vectors	bold Roman lowercase letters	$\mathbf{k}$
Matrices	bold Roman uppercase letters	$\mathbf{M}$

Symbols

$\arg(\cdot)$	argument of a complex number
$(\cdot)^\dagger$	Hermitian adjoint of a matrix
$(\cdot)^+$	Moore–Penrose inverse
$(\cdot)^\mathrm{T}$	transpose of a matrix
$\hat{(\cdot)}$	unit vector
$\prod$	product operator
$\|\cdot\|$	Euclidean distance
$\mathfrak{Im}(\cdot)$	imaginary part of a complex number
$\mathfrak{Re}(\cdot)$	real part of a complex number
$\otimes$	Kronecker product

$:=$	defined as
α	azimuthal rotation angle
β	film phase thickness
Δ	phase change
$\delta_{\mathrm{rp}}, \delta_{\mathrm{rs}}$	phase of p- and s-polarized light
δ	retardance
δ_i	phase of the wave
ε_0	permittivity of free space
$\boldsymbol{\eta}$	surface normal
γ	deflection angle
λ	wavelength
Ψ	amplitude ratio
ρ	ratio of the amplitude reflection coefficients
σ	standard deviation
θ_{max}	maximum incident angle
$\delta\theta$	included angle
θ_0	angle of incidence
θ_0'	nominal angle of incidence
θ_{B}	Brewster's angle
ϕ	tilt angle
χ^2	squared error function
$\mathbf{B}$	magnetic induction
c	speed of light
$\mathbb{C}$	set of complex numbers
$\exp(x)$	exponential function, $\exp(x) = e^x$
$\mathbf{E}$	electric field
$\tilde{E}$	amplitude of the electric wave
$\lvert E_x \rvert, \lvert E_y \rvert$	normalized electric field amplitudes
d	film thickness

D_θ	thickness cycle
d_{offset}	offset for the reflected beam
$DI(\mathbf{M})$	depolarization index of a Mueller matrix
h	offset along the surface normal
I	intensity
i	imaginary unit
$\mathbf{J}$	Jones matrix
j_{ij}	elements of a Jones matrix
$\mathbf{J}^{(3)}$	3D Jones matrix
$j_{ij}^{(3)}$	elements of a 3D Jones matrix
$\mathbf{k}$	propagation vector
k	extinction coefficient
$\mathbf{M}$	Mueller matrix
M_{ij}	elements of a Mueller matrix
$\hat{\mathbf{M}}$	normalized Mueller matrix
m_{ij}	normalized elements of a Mueller matrix
$\mathbf{n}$	surface normal
N	complex refractive index
n	refractive index
N_M,S_M,C_M	NSC parameters for a Mueller matrix
$\mathbf{O}$	3D transformation matrix
$\mathbf{P}$	polarization transfer matrix
P	irradiance
$\mathbb{R}$	set of real numbers
$\mathbb{R}_{>0}$	set of positive real numbers
r	radius
$\mathbf{r}$	coordinates in vector form
$r_{\text{p}}, r_{\text{s}}$	reflection amplitude coefficients
$R_{\text{p}}, R_{\text{s}}$	magnitude of the reflection amplitude coefficients

R	reflectance
$\mathbf{S}$	Stokes vector
S_0, S_1, S_2, S_3	Stokes parameters
$\hat{\mathbf{S}}$	normalized Stokes vector
s_1, s_2, s_3	normalized Stokes parameters
$\mathbf{s}, \mathbf{p}$	local coordinate system
t	time
$t_\mathrm{p}, t_\mathrm{s}$	transmission amplitude coefficients
$T_\mathrm{p}, T_\mathrm{s}$	magnitude of the transmission amplitude coefficients
u	uncertainty
x, y, z	world coordinates
$\mathbb{Z}$	set of integers

Acronyms

2D	two-dimensional
3D	three-dimensional
AOI	angle of incidence
BFP	back focal plane
CCD	charge-coupled device
CMOS	complementary metal-oxide semiconductor
DI	depolarization index
DOP	degree of polarization
IES	Lehrstuhl für Interaktive Echtzeitsysteme
IOSB	Fraunhofer-Institut für Optronik, Systemtechnik und Bildauswertung
KIT	Karlsruher Institut für Technologie
LCVR	liquid crystal variable retarder
LP	linear polarizer

NA	numerical aperture
NPBS	non-polarizing beamsplitter
NRMSE	normalized root-mean-squared error
PDF	probability density function
PEM	photoelastic modulator
POI	plane of incidence
PSA	polarization state analyzer
PSG	polarization state generator
QWP	quarter-waveplate
RMSE	root-mean-squared error
SD	standard deviation

1 Introduction

1.1 Motivation

Objects with physical properties that must be tightly controlled (e.g., dimensions, transmittance, reflectance and concentrations) are common in industrial production processes in the automobile, semiconductor and biological industries. An industrial measurement system for quality assurance must feature high precision and accuracy to allow 100 percent control over the properties of objects for the manufacturing process.

Ellipsometry is a reliable and very sensitive method for characterizing materials and thin films [Fuj07]. It features high precision and sensitivity and allows nondestructive measurement for process monitoring of optical elements, displays and semiconductors. Ellipsometry uses the changes in polarization when polarized light is reflected (or transmitted) from a sample at an oblique (or normal) angle of incidence (AOI). Figure 1.1 shows an ellipsometer in the reflection configuration. A collimated beam of light is emitted from a polarization state generator (PSG), reflected by the sample in accordance with the law of reflection and detected by a polarization state analyzer (PSA). By using a model which includes the physical structure and optical properties of the test object and measuring the changes in polarization states after reflection or transmission, the optical properties (refractive indices) or film thickness of the test object can be calculated. The object model shows the physical structure of the test object, such as the substrate, the number and types of films and the roughness of the surface. These known and measured parameters are used to determine the unknown physical properties of the observed object using an optimization process.

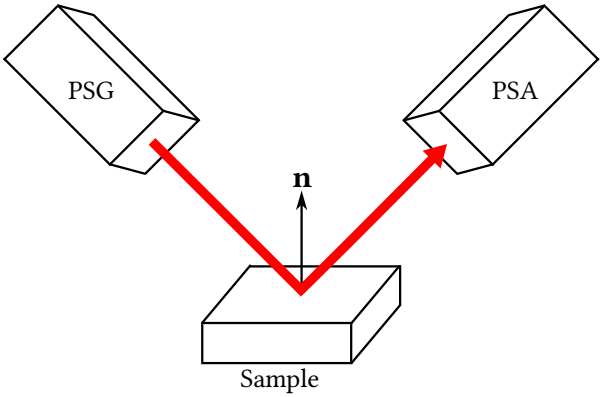

Figure 1.1: Schematic diagram of a general ellipsometer in the reflection configuration: **n** is the surface normal of the sample. A PSG emits light with different polarization states and a PSA detects the polarization states of light that is reflected from the sample.

Ellipsometry is a standard laboratory tool for special applications in biology and medicine [Arw98] and for accurately measuring the thickness of thin films from sub-nanometers to a few micrometers [Tom16]. It can also be used to characterize materials, detect contaminants [Ped82], determine the degree of crystallinity [Shi97] or to monitor the corrosion of alloys [Kot09]. However, it is rarely used in industrial applications because of the geometrical limitations of conventional ellipsometry. Measurements with conventional ellipsometers are only possible on plane surfaces or plane surface elements (with respect to the size of the measurement beam). A signal is only detected if the angle and height of the PSG and PSA in relation to the surface normals are aligned in such a way that they comply with the laws of reflection. Even slight misalignments from the ideal reflection or transmission settings can result in significant experimental errors. For larger misalignments, it is not possible to generate any meaningful signals (see Figure 1.2). For nonplanar samples, the curvature of the surface alters the incidence angle and the vertical position of the reflected light, so the ideal reflection condition for the ellipsometer cannot be achieved.

The angle settings for the PSG and the PSA must be very precisely adjusted relative to the surface normals (typical deviations $< \pm 0.1°$) [Hil11]. The height

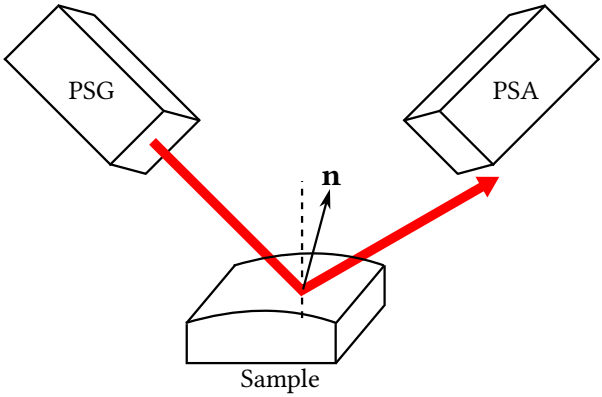

Figure 1.2: Schematic diagram of a conventional ellipsometer measuring a nonplanar sample. The surface normal **n** is changed by the curvature of the surface.

of the surface relative to the optical components must also be adjusted very accurately (typical deviations < 0.2 mm). These conditions are necessary for ellipsometry measurements. Nonplanar samples must be adjusted to allow the PSA to receive a sufficient signal. The process of the alignment and adjustment for the ellipsometer and sample is time-consuming. Therefore, inline inspection of curved surfaces is almost impossible using a standard ellipsometry configuration.

However, many applications require quality monitoring or characterization for nonplanar surfaces, e.g., the uniformity of metallic coatings [Sha19], multilayer coatings on extreme ultraviolet mirrors for high reflectance [Gra22], functional coatings on lenses for anti-reflection and self-cleaning [Sar20] and the oxide layer on a Si-enriched sphere for volume evaluation [Fuj17]. For most semiconductor processes, samples must be rotated to produce uniform layers, e.g., plasma-enhanced chemical vapor deposition and epitaxial growth process. Rotating samples inevitably produces a wobble effect because the rotational axis and the surface normal for the sample are not parallel. A holistic approach is required to overcome the geometric limitation. The measurement system must also be pertinent to different shapes of surfaces and must feature minimal complexity to allow use in real industrial applications.

1.2 Research topics

This study is concerned with ellipsometry measurements of nonplanar surfaces. The problems of nonplanar surfaces are quantified by the following calculation.

Figure 1.3 shows a planar surface (dotted line) that defines the xy plane ($z = 0$). The z axis (0,0,1) is the surface normal $\mathbf{n}$. If beam $\mathbf{k}_0$ is incident on the yz plane and the incidence angle is θ_0, the incident beam $\mathbf{k}_0$ and the reflected beam $\mathbf{k}_1$ are expressed as:

$$\mathbf{k}_0 = (0, \sin\theta_0, -\cos\theta_0), \tag{1.1}$$

$$\mathbf{k}_1 = (0, \sin\theta_0, \cos\theta_0). \tag{1.2}$$

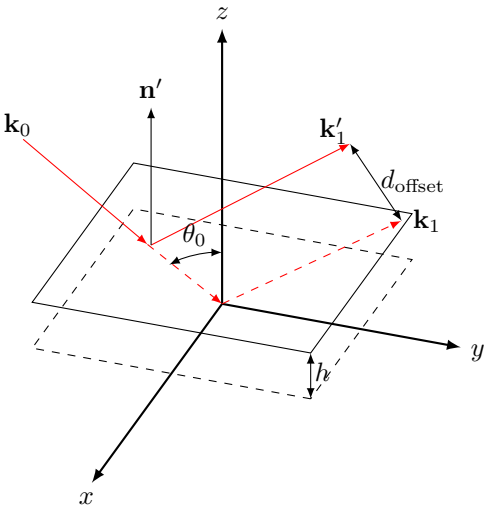

Figure 1.3: The position of the reflected beam is changed due to the offset of the sample along the surface normal $\mathbf{n}$.

If the surface has an offset h along the surface normal $\mathbf{n}$, then the surface normal and the reflected beam become $\mathbf{n}'$ and $\mathbf{k}_1'$, so d_{offset} is the offset for the reflected beam:

$$d_{\text{offset}} = 2h \sin\theta_0. \tag{1.3}$$

For an incidence angle of 70° and an offset along $\mathbf{n}$ of 1 mm, the beam offset d_{offset} on the detector is about 1.9 mm.

Figure 1.4 illustrates a tilt surface (solid line) and a reference surface (dashed line) on the xy plane. If the reference surface rotates around the y axis, the surface normal for the sample becomes $\mathbf{n}' = (\sin\phi, 0, \cos\phi)$. Using the law of reflection, the angle of incidence θ' and the reflected beam $\mathbf{k}_1'$ after tilting are calculated as:

$$\cos\theta_0' = \cos\theta_0 \cos\phi, \tag{1.4}$$

$$\mathbf{k}_1' = (\cos\theta_0 \sin 2\phi, \sin\theta_0, \cos\theta_0 \cos 2\phi). \tag{1.5}$$

The included angle $\delta\theta$ between the original reflected beam $\mathbf{k}_1$ and the reflected beam $\mathbf{k}_1'$ after tilting is calculated using the scalar product:

$$\cos\delta\theta = \sin^2\theta_0 + \cos^2\theta_0 \cos 2\phi. \tag{1.6}$$

For an incidence angle of 70°, if a surface tilts 5° around the y axis, the angular deviation is 3.4° for the detector. If the distance between the surface and the detector is 150 mm, the offset is 8.9 mm.

For nonplanar surfaces, sample offset and tilt must be considered. A photodiode is used for intensity measurements in ellipsometry and the diameter of the photosensitive area is usually less than 5 mm. Therefore, using the calculation results, sample offset and tilt produce a significant displacement in the detector, especially at large angles of incidence. The beam displacement also

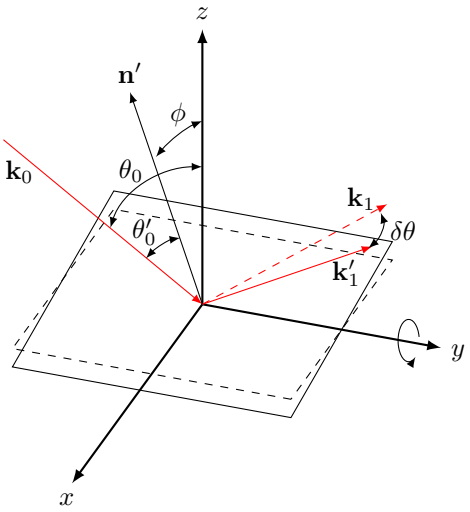

Figure 1.4: The position of the reflected beam when the sample is tilted around the y axis.

decreases the measurement accuracy. In the worst case, the detector does not receive any signal. The angular deviation of the reflected beam also causes unexpected polarization effects in optical elements. Waveplates (retarders) are very sensitive to the angle of incidence so a change in the AOI changes the retardance of the waveplates, which causes measurement errors for the PSA.

For analysis of ellipsometry measurements, the AOI must be known. The accuracy of the AOI determines the accuracy of measurement results for refractive indices and film thickness. A full measurement of a nonplanar surface requires a raster scan. A curved surface also changes its surface normal during the scanning. An accurate value for the AOI increases the accuracy of the results. A special optical design, measurement methods and data analysis for the AOI are necessary for ellipsometry measurements of nonplanar surfaces.

1.3 Main contribution

This study develops an ellipsometer with a holistic approach for nonplanar surfaces. The main contributions are:

A return-path Mueller matrix ellipsometer with a retroreflector is designed and constructed, which is named retroreflex ellipsometer.

- The retroreflex ellipsometer measures Mueller matrices for nonplanar surfaces. This uses the concept of the retroreflector, whose polarization characteristics are the same as those for an ideal mirror within an angular range of approximately $\pm 30°$ [Che20].
- The polarization model for nonplanar surfaces is derived by polarization ray tracing. The model is used to analyze measured Mueller matrices to calculate the ellipsometry parameters and the angles for coordinate rotation [Che23a].

Several methods that use retroreflex ellipsometry have been proposed to determine the angle of incidence. A Monte Carlo uncertainty analysis of these methods is simulated. The effect of a spherical shape on the measurement of ellipsometric parameters is analyzed.

- For optically isotropic two-phase systems (ambient/ substrate), the proposed ellipsometer simultaneously measures the angle of incidence, the tilt angle and the refractive index with calibrated reflectance values [Har20, Che21b].
- For optically isotropic three-phase systems (ambient/ thin film/ substrate), the system measures the angle of incidence, the tilt angle and the film thickness using the refractive indices of the film and substrate [Che23a].

In order to verify the proposed method and the retroreflex ellipsometer, several experiments are conducted.

- The Mueller matrix for the retroreflector is analyzed and measured at different angles of incidence using a commercial, in order to determine the polarization characteristics ellipsometer [Che20].
- The accuracy and precision of the retroreflex ellipsometer is determined using straight-through measurements in air and reference samples [Che20, Che23a].
- The refractive index of an off-axis parabolic mirror is measured and the result is compared with that for a commercial ellipsometer [Che20].
- The film thickness of a protected gold-coated concave mirror is measured and the results are compared with those for a commercial ellipsometer. The surface of the concave mirror is reconstructed using calculated angles of incidence and tilt [Che23a].

1.4 Thesis outline

The outline of this thesis is shown as follows:

Chapter 2 Related work
This chapter presents related work on methods of measuring thin films and the optical properties of curved surfaces using ellipsometry.

Chapter 3 Polarized light and ellipsometry
The fundamental knowledge of polarized light, polarization ray tracing and ellipsometry are introduced in this chapter.

Chapter 4 Retroreflex ellipsometry
This chapter explains the principle of retroreflex ellipsometry. The system design and the retroreflex ellipsometry prototype are demonstrated. A polarization analysis of the retroreflector is also presented.

Chapter 5 Measurement methods and uncertainty analysis for non-planar surfaces
Using retroreflex ellipsometry, several methods are proposed to calculate the incident angle, tilt angle and the angle of the coordinate rotation for optically

isotropic two-phase and three-phase systems. The Monte Carlo uncertainty for these methods and analysis of ellipsometric measurements of nonplanar surfaces are also calculated.

Chapter 6 Results and discussion
Several experiments are conducted and the results are analyzed to verify the proposed method and the retroreflex ellipsometer.

Chapter 7 Conclusion and outlook
Conclusions are drawn and proposals for future research are presented.

2 Related work

This study develops an ellipsometer and analysis methods for nonplanar surface measurements. This chapter presents an extensive overview of related work in three sections. Section 2.1 shows the variety of ellipsometers that can be used to measure nonplanar surfaces. Section 2.2 shows different methods to characterize nonplanar surfaces using ellipsometric measurements. The features and challenges of these methods are discussed in Section 2.3.

2.1 Ellipsometry for nonplanar surfaces

Ellipsometry is usually used for planar surfaces but some ellipsometers measure nonplanar surfaces. There are three types: microellipsometry, imaging ellipsometry and return-path ellipsometry. In this section, the basic principles and the main features of these approaches are described.

2.1.1 Microellipsometry

Microellipsometry is a special configuration of ellipsometry that uses an objective lens to focus the input light on the sample and collects the reflected light at the sensor. The objective lens is placed perpendicularly to the surface. Microellipsometry uses high numerical aperture (NA) objective lenses to enhance spatial resolution for measurements of microstructures. The measurements are single-point or whole-field, depending on the configuration. This technique has been widely used since the 1980s. The spot size (a few mm) for traditional ellipsometry is much larger than that for microellipsometry, which

is several microns with a high-NA objective lens. Therefore, microellipsometry produces high-resolution 2D maps of polarimetric parameters from the sample.

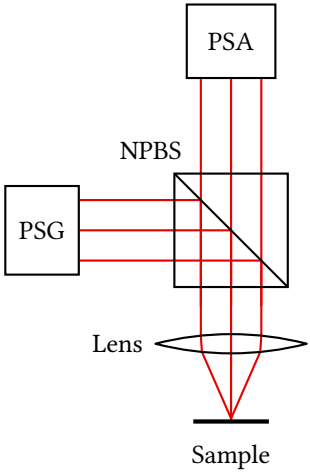

Figure 2.1: Schematic diagram of a microellipsometer.

The first microellipsometer was proposed by Stevens in 1980 [Ste80]. The schematic diagram of typical microellipsometers is shown in Figure 2.1. Collimated light from the polarization state generator (PSG) is focused using the objective and reflected light is collected by the same objective. The light then traverses the non-polarizing beamsplitter (NPBS) and is received by the polarization state analyzer (PSA). The angles of incidence on the sample vary depending on the position of light rays on the objective. The NA for the objective determines the maximum incidence angle θ_{max} on the sample. The definition of NA is shown in Figure 2.2 and is calculated as:

$$\text{NA} = n \sin \theta_{\text{max}}, \tag{2.1}$$

where n is the refractive index of the medium next to the objective lens and θ_{max} is half the angular aperture.

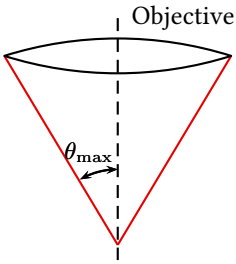

Figure 2.2: Numerical aperture of an objective. The dashed line is the optical axis of the objective.

In an air environment ($n = 1$), for an objective lens with a NA value of 0.9, the maximum incident angle is 64.16° and the minimum incident angle is 0°. For a planar sample that is aligned with the optical axis, the distribution of incidence angles exhibits radial symmetry. Therefore, microellipsometry is also called angle-resolved ellipsometry. The ellipsometric parameters can be calculated by the intensity distribution on the sensor. Similar setups can be found in the studies of See et al. [See96], Feke et al. [Fek98], Zhan and Leger [Zha02], Ye et al. [Ye07] and Otsuki et al. [Ots13].

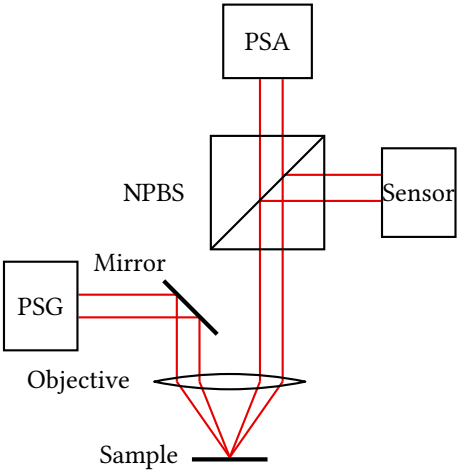

Figure 2.3: Schematic diagram of a microellipsometer with off-axis illumination.

Another variation of microellipsometry is shown in Figure 2.3. Instead of on-axis illumination, off-axis illumination was used by Leonhardt et al. [Leo91] to improve lateral resolution. This configuration decreases the effect of beam focusing if the input beam from the PSG is much smaller than the diameter of the aperture of the objective [Hol96]. Therefore, the angle of incidence is fixed for a planar surface. This setup measures surface topography and ellipsometry parameters simultaneously by scanning the surface. The surface profile is determined using a variety of sensors or methods, such as a charge-coupled device (CCD) array [Leo91] or a change in the input azimuth angle [Hol96].

To reduce the mechanical scanning time, imaging back focal plane (BFP) microellipsometry is used. The schematic diagram is shown in Figure 2.4. The off-axis illumination is focused onto the BFP of the objective. If the objective fulfills Abbe's law, the illumination is parallel and impinges on the surface at an oblique incident angle. The light is then recollected by the objective lens and is received by the PSA. Surface topography is also measured using microscopic fringe projection [Leo98] and interferometry [Leo03].

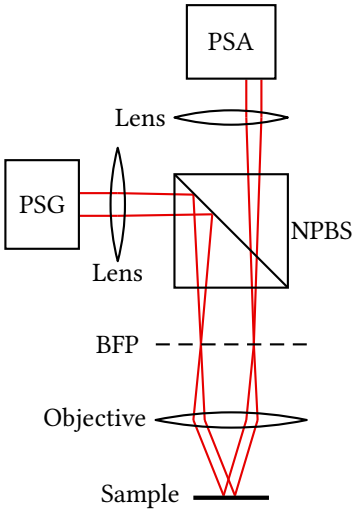

Figure 2.4: Schematic diagram of back focal plane microellipsometry.

2.1.2 Imaging ellipsometry

Microellipsometry gives high lateral resolution but the entire sample must be scanned in vertical and lateral directions to obtain the ellipsometry parameters and topography. The scanning process is time-consuming and requires high-precision stages and auto-focusing sensors to adjust the sample to the focus plane. Imaging ellipsometry uses imaging sensors, such as a CCD sensor or a complementary metal-oxide-semiconductor (CMOS) sensor, to measure an area instead of a single point. Each pixel on the imaging sensor represents a single ellipsometric measurement and the lateral resolution depends on the pixel size and the lens system. Therefore, imaging ellipsometry gives high lateral resolution (up to 1 µm [Che21a]) with area measurements. Different configurations have been developed for the spatial characterization of samples by Löschke [Lös79], Cohn et al. [Coh88], Jin et al. [Jin96], Han and Chao [Han06], Wurstbauer et al. [Wur10], Arteaga and Kuntman [Art14] and Jin et al. [Jin21].

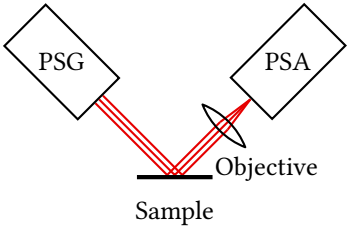

Figure 2.5: Schematic diagram of imaging ellipsometry.

A typical configuration of imaging ellipsometry is shown in Figure 2.5. Collimated beams impinge on the surface and the reflected light passes through the imaging lens system to the PSA, which contains an imaging sensor. To increase the field of view, low-NA objectives are used for imaging ellipsometry. However, the lateral resolution is proportional to the NA of the objective. A high-NA objective results in higher-resolution images and allows a large angular deviation for deflected beams from a nonplanar sample. Therefore, for nonplanar surfaces, a high-NA objective is essential. Kajihara et al. measured

a non-polar lubricant on a magnetic disk using two-stage imaging ellipsometry microscopy (NA = 0.9) [Kaj11]. Duwe et al. used imaging ellipsometry with an objective numerical aperture of 0.45 to measure a micro-lens array with a radius of curvature of 6.5 mm [Duw19].

2.1.3 Return-path ellipsometry

Figure 2.6 shows a schematic diagram for return-path ellipsometry. The light beam that is reflected from the surface is reflected back to the same position on the surface by a reflecting element, such as a planar mirror, a spherical mirror or a retroreflector. This configuration features a simple construction, is suitable for process monitoring and has a higher sensitivity to the optical properties of surfaces than conventional ellipsometers [Azz77].

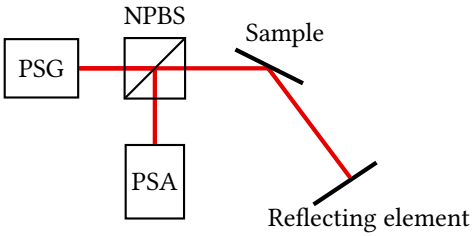

Figure 2.6: Schematic diagram showing return-path ellipsometry.

The planar mirror configuration for return-path ellipsometry uses a planar mirror to reflect light back to the PSA so it can only be used for flat surfaces because there is an optical lever. Any small angular or offset in the sample is greatly magnified in the displacement of the reflected beam [Ale89] so reflected light can only be received by the PSA when the planar mirror is perpendicular to the reflected ray. Slight misalignments or curved surfaces can cause significant experimental errors. Planar mirror types for return-path ellipsometry for different applications are described in the studies of O'Bryan [OBr36], Yamamoto [Yam74], Yamaguchi and Takahashi [Yam76], Azzam [Azz77], Wang and Arwin [Wan04], and Watkins et al. [Wat10].

For most coating processes in semiconductor manufacturing, samples are usually rotated by a rotary stage to obtain uniform layers, such as plasma-enhanced chemical vapor deposition and the epitaxial growth process. The rotation of samples inevitably produces a wobble because the rotational axis and the surface normal for the sample are not parallel. As mentioned in Section 1.2, ellipsometry is very sensitive to the angle of incidence and the sample position. To obtain accurate measurements, Haberland et al. used return-path ellipsometry and replaced the planar mirror with a spherical mirror [Hab98]. In terms of geometric optics and paraxial approximation, every ray that passes the center of curvature of the spherical mirror is reflected back along its original path. If the sample is placed in the geometrical center of the spherical mirror, the incident ray is always perpendicular to the spherical mirror so no polarization distortion is induced by the mirror [Fu95]. This configuration reduces the error from the angular deviation induced by sample wobbling during rotation but non-polarizing beamsplitters have a narrow wavelength range (e.g., 400-700 nm, 700-1100 nm or 1100-1600 nm) and polarization distortion [Art14] because they have multilayer dielectric coatings which have very strong polarization-dependent properties. Because of the optical properties of the NPBS, they are not suitable for spectroscopic ellipsometry. Johs and He modified the design of Haberland et al. by replacing the NPBS with two right-angle prisms [Joh11]. The prisms have a wide wavelength range and produce no polarization distortion because the double reflection from the prisms cancels the change in the polarization state. However, mechanical constraints mean that there is an offset between the incident beam and the reflected beam from the sample. A spherical mirror configuration is used for return-path ellipsometry because there is a high angular tolerance if the sample is rotated or curved. However, the alignment condition is not fulfilled for large sample offsets because the sample is not positioned in the center of the spherical mirror.

To solve the alignment problem for nonplanar samples, Hartrumpf and Negara developed a laser scanner using a retroreflector (retroreflective sheet) at Fraunhofer IOSB [Har17]. A retroreflector is used as a reflector. A retroreflector returns the light beam from the sample on the same beam path with a fixed phase difference of 180°, so the polarization effect is the same as that for

an ideal mirror [Li19]. In this configuration, the alignment condition for the sample and the detector is fulfilled at an angular deviation up to 30° [Neg20]. This design also addresses the problem of large sample offsets because the size of the retroreflector is flexible, so deflected beams are covered during scanning. In 2020, Negara et al. used return-path imaging ellipsometry with a rotating reflector that consists of a mirror and a retroreflector to determine surface inclination and refractive index [Neg20].

2.2 Characterization of nonplanar surfaces using ellipsometric measurements

This section describes different approaches to characterize nonplanar samples or to reduce the effect of nonplanar surfaces on ellipsometric measurements.

The surface normal from a nonplanar sample changes during scanning measurements. For conventional ellipsometry (see Figure 1.2), the change in the surface normal is seen in the misalignment of the PSA with respect to the plane of incidence (POI) [Asp71]. The misalignment affects the measurement accuracy for ellipsometry parameters. Many methods minimize the alignment error [Asp71, Zei74, Rie79, Joh93, An03, Men16].

Lee and Chao determined that the azimuthal deviation in the polarizer is the same as the deviation in the surface normal for a calibrated rotating-analyzer ellipsometer [Lee05]. The study used the three-intensity technique to measure a SiO_2/Si sample with a $\pm 2°$ tilt angle at an incidence angle of 70°. The measured azimuthal deviation for the polarizer is similar to the tilt angle. Further experiments verified the high degree of accuracy (0.03°) for tilt angle measurements by tilting a well-calibrated sample with a spacer [Han09]. However, the three-intensity measurement is only valid for small tilt angles (a few degrees) [Duw19] because deviation in the incident angle must be considered for large tilt angles [Li16]. Prior knowledge of the incident angle for a reference measurement is also required.

Neuschaefer-Rube and Holzapfel proposed a method to measure surface geometry and material distribution using microellipsometry [Neu03]. The study used an objective lens to focus and recollect a light beam on the sample, which is described in Section 2.1. The surface inclination is determined directly using the polarization model without other topometric measurement methods, such as interferometry, deflectometry and laser triangulation. The angle of incidence and the surface orientation are determined using the eight-zone-measurement algorithm. When the entire surface is scanned, the surface profile is reconstructed using the surface inclination (gradient data). However, the focusing beam (60 µm) induces a greater deviation in the phase difference than in the amplitude ratio. For transparent samples, the error in the phase difference is several degrees. Decreasing the spot size even increases the measurement error.

In 2016, Li et al. used a conventional ellipsometer to measure nonplanar surfaces [Li16]. The study determined the effect of deviation in the incident plane and proposed a Mueller matrix model with two azimuthal rotation matrices to describe the Mueller matrix for the tilted surface. The angles of two rotation matrices have the same absolute values but different signs. Mueller matrix ellipsometry was used to measure the thickness of the oxide layer on a convex lens and the radius of curvature was calculated by the scanning result. In 2019, Duwe et al. modified the Muller matrix model proposed by Li et al. because there is a significant mismatch at greater tilt angles [Duw19]. They showed that the two rotation angles have different signs and values and that there is no analytical form for the exit side of the rotation matrix. This was verified using a spectroscopic imaging ellipsometer to measure a tilted sample. The experimental results feature a lower root-mean-squared error (RMSE) for a large tilt angle (8°) than the result for the study by Li et al. The patent that was awarded to Duwe [Duw22] demonstrates the analytical form for the incident side of the rotation matrix and the approximated rotation matrix for the exit side.

Johs and He used a return-path Mueller matrix ellipsometer to measure samples with a wobble effect [Joh11] and showed that if an optically isotropic sample is tilted with regard to the plane of incidence, there is optical anisotropy.

The study established a Mueller matrix model to describe the measurement system and compensated for wobble using two azimuthal rotation matrices for the receiver and source optics. The rotational matrices are determined by fitting the measured Mueller matrix numerically. The proposed return-path ellipsometer measures samples with a ±0.8° substrate wobble and a sample path length of 1 m to the ellipsometer. The variation in the intensity is less than 2%. However, this setup is only suitable for pure angular deviation because sample offsets produce a large displacement in the reflected beam, so the center and height of the sample must be aligned and adjusted carefully. Using a similar configuration of Johs and He, Negara et al. proposed a Mueller matrix model with two azimuthal rotation matrices that have the same values and signs [Neg20]. The study measured an uncoated gold parabolic mirror. The respective mean absolute errors for incidence angle, tilt angle and height are 0.33°, 0.72° and 24.8 µm, respectively.

Křepelka used geometrical ray tracing and polarization optics to analyze ellipsometric measurements using a convex mirror [Kre11]. Three averaging methods were used to reduce measurement errors. A small spot size with a suitable convergent angle reduces measurement errors that are induced by spherical shape. Another approach to reduce the mixed polarization effect from nonplanar surfaces was proposed by Zhang et al. [Zha12], who used an aperture to allow central rays to pass and block the remainder of the rays. An aperture size of 4 mm minimizes the deviation in the incidence angle to a range of ±0.15° and the error in the phase difference is reduced to 0.024°.

2.3 Summary

Table 2.1 summarizes the features and challenges of nonplanar surface measurements for different types of ellipsometry. Microellipsometry is a straightforward method to measure ellipsometry parameters and surface topometry. Microellipsometry uses a high numerical aperture microscope objective to collect the reflected light to increase the lateral resolution. A high-NA objective is also used for measuring nonplanar surfaces. The acceptable gradient

for a sample is equal to the half maximum incidence angle θ_{max} for the objective [Tho20]. For samples with a steep gradient, high-NA objectives lenses are required. An objective lens with a NA of 0.8 can receive a change in reflected light up to 26.6°. However, the working distance for high-NA objectives is usually short: an objective (CFI Achromat 60X, Nikon) with a NA of 0.8 has a working distance of 0.3 mm. This limits the practical applications of nonplanar surfaces because the short working distance increases the danger of collision between the objective and the sample. The hardware for topometric measurements also increases the system complexity, especially in terms of system alignment and calibration. To increase accuracy, the planes of the measurement beam must be accurately focused so vertical and area scanning of all surface points is necessary and this is very time-consuming.

Table 2.1: Comparison of four different types of RPE.

Configuration	Features	Challenges
Microellipsometry	High lateral resolution Surface profile	Complex system Vertical and area scanning Short working distance
Imaging ellipsometry	Medium lateral resolution Large field of view Area measurements	Focus scanning Spectral scanning Limited spectral range
Return-path ellipsometry	Simple setup High sensitivity Large slope and offset*	High-intensity illumination Low lateral resolution Limited spectral range Polarization distortion

*The reflecting element is a retroreflective sheet.

Imaging ellipsometry using high-NA objectives is used to measure nonplanar surfaces but the distance between the sample and the objective is limited. As mentioned in Section 1.2, the offset in the deflected beams is proportional to the distance between the sample and the objective. To measure surfaces with a steep gradient, the objective must be close to the surface. Only a small range of gradients can be measured because the PSA is sensitive to the incidence angle. A PSA comprises a linear polarizer and a waveplate that is made of bi-refringent materials and is designed for a normal incidence angle. Thus, the retardance of a waveplate is changed to a different degree when the incident angle is not normal. A large incidence angle for the waveplate induces significant errors in retardance. The depth of focus of objectives is also limited

so only the center region of the image is focused. Therefore, focus stacking is necessary to get a wider field of view. This combines multiple images that are taken at different focal planes into a single image. The spectral range of cameras and optical components is usually between 250 nm and 1700 nm so imaging ellipsometry is suited for use in laboratory tools.

Return-path ellipsometry has a high sensitivity to the optical properties of materials because there is a double reflection from the sample. The sensor and illumination units are on the same side so in-situ measurements are possible because only one observing window is required. Special reflectors (spherical mirror or retroreflector) allow ellipsometric measurements for nonplanar surfaces but this configuration requires a high-power light source because the NPBS, which has a split ratio of reflectance and transmittance of 50:50, loses a large amount of power from the light source (more than 75% by a reflection and transmission). The system also requires careful calibration for the polarization distortion that is induced by the non-polarizing beamsplitter because the NPBS is not an ideal component for polarization optics. The beamsplitter must be accurately aligned and calibrated [Che20]. The spectral range of a NPBS is limited to a certain range because there are anti-reflection coatings, so they have a range in the visible (400-700 nm), near-infrared (700-1100 nm) and infrared (1100-1600 nm) spectra. Prisms can be used instead of NPBS to give a larger spectral range but system complexity increases and beams are offset on the sample. A return-path ellipsometer measures steep gradient slopes (maximum angle deviation $\pm 30°$) and large offsets (no limitation) in samples if a retroreflective sheet is used as a reflecting element [Har17, Neg20, Che20]. Return-path ellipsometers use collimated beams, which have a low lateral resolution. Imaging sensors increase resolution but multiple reflections and scattering in the retroreflector can degrade image quality. In general, return-path ellipsometry is suitable for inline or in-situ measurements because installation is flexible and large angular deviations and offsets are acceptable.

Ellipsometric measurements are described using Jones or Mueller matrices and the calibrated system is associated with a particular plane of incidence, which is defined by the incident ray and the surface normal. However, if the sample is curved or tilted, the POI changes because the curvature of the

surface and optical anisotropy occurs in the measured Jones or Mueller matrix for optically isotropic materials. If coordinates are not transformed correctly for the changed POI to the measured results, experimental errors increase significantly, especially for large tilt angles. Therefore, the transformation must be accurately determined.

The azimuthal deviation in the polarizer is used to determine the tilt angle for surface geometry. This method is easily applied using ellipsometers without the need for extra hardware. However, for conventional ellipsometers with two rotating arms, there is no expression for the coordinate transformation matrix for the exit side (PSA). An approximation must be made, which causes calculation errors in the analysis. Return-path ellipsometry expresses the coordinate transformation matrices of the incident and exit sides in analytical form without any approximation [Che23a].

3 Polarized light and ellipsometry

This chapter presents the details of polarized light and ellipsometry. The notation and formulae for polarized light and ellipsometry are those in the volumes by Azzam and Bashara [Azz87], Fujiwara [Fuj07] and DIN 50989 Part 1-3 [DIN 5098918, DIN 5098921, DIN 5098922]. The polarization of light waves is firstly described by mathematical representation in Section 3.1. The reflection and transmission of light for two-phase and three-phase systems are described using Fresnel equations in Section 3.2. Jones calculus and Mueller calculus are used to mathematically describe optical components and measurements in Sections 3.3 and 3.4. Section 3.5 uses polarization ray tracing to calculate the path and polarization state of light rays through optical systems described in the book of Chipman et al. [Chi18]. The principle of ellipsometry and Mueller matrix measurements is demonstrated in Section 3.6.

3.1 The polarization of light waves

Light is an electromagnetic wave that is described by Maxwell's equations [Bor16]. Figure 3.1 shows the propagation of an electromagnetic wave, where the electric field **E** and magnetic induction **B** are perpendicular to each other. The electric field for a plane monochromatic wave at a fixed point in a space is expressed as:

The electric field of a monochromatic wave at a fixed point in a space can be expressed as:

$$\begin{aligned} \mathbf{E} &= E_x\hat{\mathbf{x}} + E_y\hat{\mathbf{y}} + E_z\hat{\mathbf{z}}, \\ E_i &= \tilde{E}_i \cos(\omega t + \delta_i), \qquad i = x, y, z, \end{aligned} \tag{3.1}$$

where $\hat{\mathbf{x}}$, $\hat{\mathbf{y}}$ and $\hat{\mathbf{z}}$ denote unit vectors of the cartesian coordinate; ω is the angular frequency and $\tilde{E}_i$ and δ_i are defined as the amplitude and phase of the wave which vibrates along with the ith axis at time t. For this thesis, all unit vectors are denoted by a lowercase letter with a hat symbol.

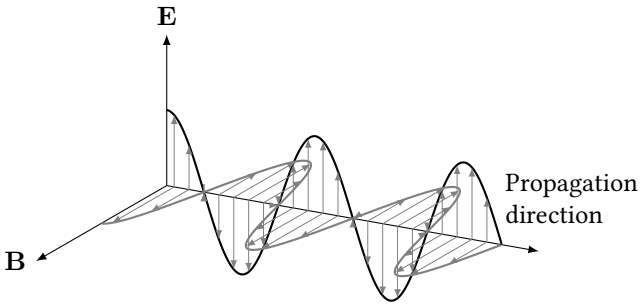

Figure 3.1: Propagation of an electromagnetic wave.

In terms of ellipsometry, polarized light is approximated by a uniform transverse-electric plane wave that travels along the propagation vector $\hat{\mathbf{k}}$ at position $\mathbf{r}$ and time t as:

$$\mathbf{E}(\mathbf{r},t) = [\tilde{E}\cos(\omega t - \frac{2\pi}{\lambda}\hat{\mathbf{k}}\cdot\mathbf{r} + \delta_u)]\hat{\mathbf{u}} + [\tilde{E}'\cos(\omega t - \frac{2\pi}{\lambda}\hat{\mathbf{k}}\cdot\mathbf{r} + \delta_{u'})]\hat{\mathbf{u}}', \quad (3.2)$$

where $\tilde{E}$ and $\tilde{E}'$ are the amplitudes of the electric vectors, which are independent of position $\mathbf{r}$ and time t, $\hat{\mathbf{u}}$ and $\hat{\mathbf{u}}'$ are the directions of the linear polarization, which are orthogonal to each other and $\hat{\mathbf{k}}$, and δ_u and $\delta_{u'}$ are phases. If a wave propagates along the z axis and $\hat{\mathbf{u}}$ and $\hat{\mathbf{u}}$ are parallel to the x and y axes, Equation 3.2 is written as:

$$\mathbf{E}(z,t) = [\tilde{E_x}\cos(\omega t - \frac{2\pi}{\lambda}z + \delta_x)]\hat{\mathbf{x}} + [\tilde{E_y}\cos(\omega t - \frac{2\pi}{\lambda}z + \delta_y)]\hat{\mathbf{y}}. \quad (3.3)$$

The Poynting vector represents the instantaneous flow of energy for an electromagnetic field and the irradiance P of a light beam is the magnitude of the

time average of the Poynting vector:

$$P = \frac{\varepsilon_0 c}{2} \mathbf{E}^\dagger \cdot \mathbf{E}, \tag{3.4}$$

where c and ε_0 are the speed of light and the permittivity of free space. The dagger superscript represents a Hermitian adjoint of a vector. However, the term intensity I is more commonly used. If the constant $\varepsilon_0 c/2$ is neglected, I is defined in a simple form as:

$$I = \mathbf{E}^\dagger \cdot \mathbf{E}. \tag{3.5}$$

3.2 Reflection and transmission of light

3.2.1 Fresnel equations

Figure 3.2 shows an incident ray in direction $\mathbf{k}_\mathrm{i}$ impinging on a homogeneous and optically isotropic interface (two-phase system), where N, $\boldsymbol{\eta}$ and $\mathbf{k}$ are the complex refractive index, the surface normal and the propagation vector, respectively. The complex refractive index is defined as:

$$N = n - \mathrm{i}k, \qquad (n, k) \in \mathbb{R} \tag{3.6}$$

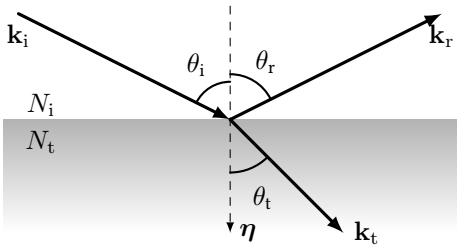

Figure 3.2: Light reflection and transmission at an oblique angle of incidence for a two-phase system.

The surface normal $\mathbf{n}$ is usually represented in outward orientation but the surface normal $\boldsymbol{\eta}$ here is defined as the inward orientation for polarization ray tracing in Section 3.5. The relationship between these two surface normals is $\hat{\mathbf{n}} = -\hat{\boldsymbol{\eta}}$.

The reflected ray propagates in direction $\mathbf{k}_\mathrm{r}$ and the refracted ray propagates in direction $\mathbf{k}_\mathrm{t}$. The propagation vectors $\mathbf{k}_\mathrm{i}$, $\mathbf{k}_\mathrm{r}$ and $\mathbf{k}_\mathrm{t}$ are coplanar and the plane they open is called the plane of incidence. The law of reflection states that the angle of incidence equals the angle of reflection ($\theta_\mathrm{i} = \theta_\mathrm{r}$) and this is written in vector form as:

$$\hat{\mathbf{k}}_\mathrm{r} = \hat{\mathbf{k}}_\mathrm{i} - 2(\hat{\mathbf{k}}_\mathrm{i} \cdot \hat{\boldsymbol{\eta}})\hat{\boldsymbol{\eta}}. \tag{3.7}$$

The law of refraction (or Snell's law) describes the propagation direction of light when light enters a medium at an oblique angle of incidence, which is described as:

$$N_\mathrm{i} \sin\theta_\mathrm{i} = N_\mathrm{t} \sin\theta_\mathrm{t}. \tag{3.8}$$

The laws of reflection and refraction are explained by electromagnetic theory. As mentioned in Section 3.1, a uniform transverse-electric plane wave that is transverse along the $\mathbf{k}$ direction is described as the superposition of two linearly polarized waves (p- and s-polarized light waves) whose propagation vectors are orthogonal, which is written as:

$$\mathbf{E} = \mathbf{E}_\mathrm{p} + \mathbf{E}_\mathrm{s} = E_\mathrm{p}\hat{\mathbf{p}} + E_\mathrm{s}\hat{\mathbf{s}}, \tag{3.9}$$

where E_p and E_s are the amplitudes of p- and s-polarized waves. The p-polarized light $\mathbf{E}_\mathrm{p}$ oscillates in the plane of incidence while the s-polarized light $\mathbf{E}_\mathrm{s}$ oscillates perpendicular to the plane of incidence. $\hat{\mathbf{p}}$ and $\hat{\mathbf{s}}$ directions can be formulated as:

$$\hat{\mathbf{s}} = \frac{\mathbf{k} \times \boldsymbol{\eta}}{|\mathbf{k} \times \boldsymbol{\eta}|}, \qquad \hat{\mathbf{p}} = \hat{\mathbf{k}} \times \hat{\mathbf{s}}. \tag{3.10}$$

The Fresnel equations describe the reflection and transmission of light using amplitude coefficients r_p, r_s, t_p and t_s as:

$$\begin{aligned} r_\mathrm{p} &:= \frac{E_\mathrm{rp}}{E_\mathrm{ip}} = \frac{N_\mathrm{t}\cos\theta_\mathrm{i} - N_\mathrm{i}\cos\theta_\mathrm{t}}{N_\mathrm{t}\cos\theta_\mathrm{i} + N_\mathrm{i}\cos\theta_\mathrm{t}}, \\ r_\mathrm{s} &:= \frac{E_\mathrm{rs}}{E_\mathrm{is}} = \frac{N_\mathrm{i}\cos\theta_\mathrm{i} - N_\mathrm{t}\cos\theta_\mathrm{t}}{N_\mathrm{i}\cos\theta_\mathrm{i} + N_\mathrm{t}\cos\theta_\mathrm{t}}, \end{aligned} \tag{3.11}$$

$$\begin{aligned} t_\mathrm{p} &:= \frac{E_{tp}}{E_{tp}} = \frac{2N_\mathrm{i}\cos\theta_\mathrm{i}}{N_\mathrm{t}\cos\theta_\mathrm{i} + N_\mathrm{i}\cos\theta_\mathrm{t}}, \\ t_\mathrm{s} &:= \frac{E_{ts}}{E_{ts}} = \frac{2N_\mathrm{i}\cos\theta_\mathrm{i}}{N_\mathrm{i}\cos\theta_\mathrm{i} + N_\mathrm{t}\cos\theta_\mathrm{t}}. \end{aligned} \tag{3.12}$$

Equations 3.11 and 3.12 can be transformed to polar coordinate representation as:

$$\begin{aligned} r_\mathrm{p} &= |r_\mathrm{p}|\exp(\mathrm{i}\delta_\mathrm{rp}), \qquad & r_\mathrm{s} &= |r_\mathrm{s}|\exp(\mathrm{i}\delta_\mathrm{rs}), \\ t_\mathrm{p} &= |t_\mathrm{p}|\exp(\mathrm{i}\delta_\mathrm{tp}), \qquad & t_\mathrm{s} &= |t_\mathrm{s}|\exp(\mathrm{i}\delta_\mathrm{ts}). \end{aligned} \tag{3.13}$$

For a reflected beam, the reflectance for p- and s- polarized waves equals the square of the magnitude of the amplitude reflection coefficients as:

$$\begin{aligned} R_\mathrm{p} &= |r_\mathrm{p}|^2, \\ R_\mathrm{s} &= |r_\mathrm{s}|^2. \end{aligned} \tag{3.14}$$

For a transmitted beam, the transmittance for p- and s- polarized waves is expressed as:

$$\begin{aligned} T_\mathrm{p} &= \frac{N_\mathrm{t}\cos\theta_\mathrm{t}}{N_\mathrm{i}\cos\theta_\mathrm{i}}|t_\mathrm{p}|^2, \\ T_\mathrm{s} &= \frac{N_\mathrm{t}\cos\theta_\mathrm{t}}{N_\mathrm{i}\cos\theta_\mathrm{i}}|t_\mathrm{s}|^2. \end{aligned} \tag{3.15}$$

The reflectance R and transmittance T for natural or unpolarized light are the average of the reflectance and transmittance for p- and s- polarized waves:

$$R = \frac{R_\mathrm{p} + R_\mathrm{s}}{2}, \qquad T = \frac{T_\mathrm{p} + T_\mathrm{s}}{2}. \tag{3.16}$$

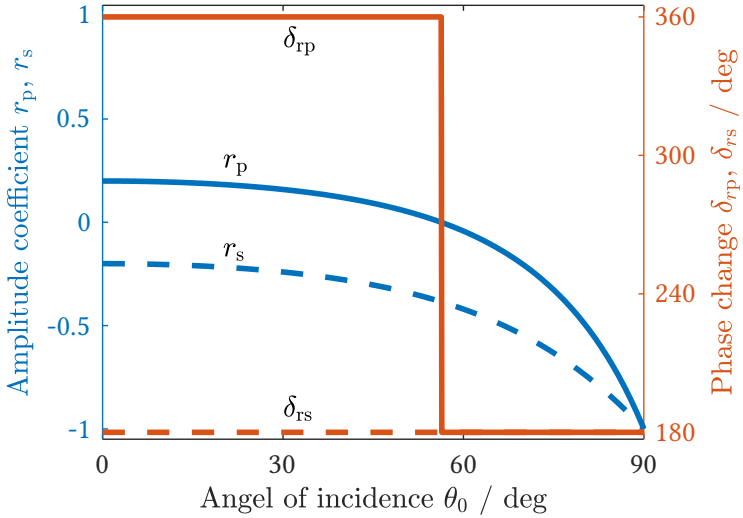

Figure 3.3: Amplitude coefficient and phase change at an air/glass interface ($N_\mathrm{i} = 1$ and $N_\mathrm{t} = 1.5$).

Using these equations, light reflection is interpreted using amplitude reflection coefficients for p- and s- polarizations. Figure 3.3 shows the amplitude coefficient and the phase change at an air/glass interface ($N_\mathrm{i} = 1$ and $N_\mathrm{t} = 1.5$). The value of r_s is negative and the phase change δ_rs is 180°. For a large incidence angle (over Brewster's angle), r_p becomes negative and the phase change δ_rp becomes 180°. If the refractive indices of the mediums are real numbers ($k = 0$), Brewster's angle θ_B is the angle of incidence if r_p equals

0, which is defined as:

$$\theta_B = \tan^{-1} \frac{N_t}{N_i}. \tag{3.17}$$

The Brewster's angle for the air/glass interface is 56.3°.

Figure 3.4 shows the reflectance value at an air/glass interface ($N_i = 1$ and $N_t = 1.5$). The value of R increases as the incident angle increases. At a normal angle of incidence, R equals 0.04. At a glancing angle, R equals 1.

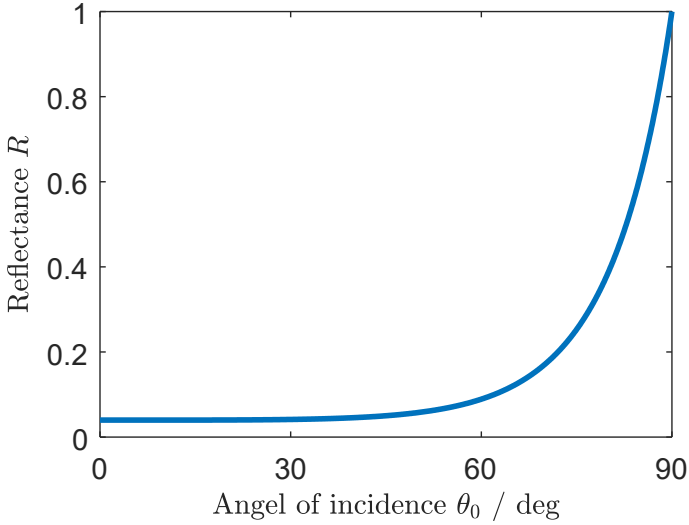

Figure 3.4: Reflectance at at an air/glass interface ($N_i = 1$ and $N_t = 1.5$).

3.2.2 Optical interference in a three-phase system

If a light ray impinges on a three-phase system (ambient/ thin film/ substrate), interference occurs if the absorption of the film is weak. Figure 3.5 shows the optical model of a three-phase system, where N_0, N_1 and N_2 are the complex refractive indices of the ambient, the film and the substrate. θ_0 and d are the angle of incidence and the film thickness. In this case, the light waves

are reflected from the ambient/thin film interface and the thin film/substrate interface. Constructive and destructive interference occur.

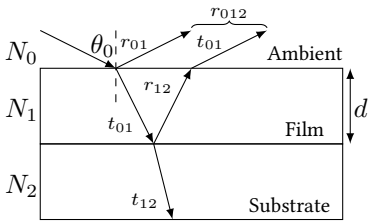

Figure 3.5: Optical model for an ambient(0)-film(1)-substrate(2) system.

For multi-layer analysis, the Fresnel equations 3.11 and 3.12 are written in a general form as:

$$\begin{aligned} r_{jk,\mathrm{p}} &= \frac{N_k \cos\theta_j - N_j \cos\theta_k}{N_k \cos\theta_j + N_j \cos\theta_k}, \\ r_{jk,\mathrm{s}} &= \frac{N_j \cos\theta_j - N_k \cos\theta_k}{N_j \cos\theta_j + N_k \cos\theta_k}, \end{aligned} \tag{3.18}$$

$$\begin{aligned} t_{jk,\mathrm{p}} &= \frac{2N_j \cos\theta_j}{N_k \cos\theta_j + N_j \cos\theta_k}, \\ t_{jk,\mathrm{s}} &= \frac{2N_j \cos\theta_j}{N_\mathrm{i} \cos\theta_k + N_\mathrm{t} \cos\theta_k}, \end{aligned} \tag{3.19}$$

where r_{jk} and t_{jk} represent the amplitude reflection and transmission coefficients at the jth interface. The p- and s-polarized light waves of the sum of all the reflected waves are expressed as:

$$\begin{aligned} r_{012,\mathrm{p}} &= \frac{r_{01,\mathrm{p}} + r_{12,\mathrm{p}} \exp(-\mathrm{i}2\beta)}{1 + r_{01,\mathrm{p}} + r_{12,\mathrm{p}} \exp(-\mathrm{i}2\beta)}, \\ r_{012,\mathrm{s}} &= \frac{r_{01,\mathrm{s}} + r_{12,\mathrm{s}} \exp(-\mathrm{i}2\beta)}{1 + r_{01,\mathrm{s}} + r_{12,\mathrm{s}} \exp(-\mathrm{i}2\beta)}, \end{aligned} \tag{3.20}$$

where β is the film phase thickness, which is defined as:

$$\beta = \frac{2\pi d}{\lambda}(N_1^2 - N_0^2 \sin^2 \theta_0)^{1/2}. \tag{3.21}$$

3.3 Jones vector and Jones matrix

In Section 3.2, Fresnel equations are used to analyze light that is reflected or transmitted at an interface at an oblique angle of incidence. However, this method is only suitable for a single interface. It is difficult to apply to the propagation of an optical wave with several polarizing components because of the complicated calculation. R. Clark Jones developed a mathematical model for the polarization of coherent light to simplify the calculation. This is called Jones calculus [Jon41].

In a Cartesian coordinate system, a light beam that travels along the z axis is expressed as the superposition of the electric fields $\mathbf{E}_x$ and $\mathbf{E}_y$, as shown in Equation 3.3, which is written in a matrix form as:

$$\mathbf{E}(z,t) = \begin{bmatrix} \tilde{E}_x \cos(\omega t - \frac{2\pi}{\lambda} z + \delta_x) \\ \tilde{E}_y \cos(\omega t - \frac{2\pi}{\lambda} z + \delta_y) \end{bmatrix}. \tag{3.22}$$

The temporal information is suppressed because waves are assumed to be monochromatic so Equation 3.22 is simplified using phasor notation [Azz87] as:

$$\mathbf{E}(z) = e^{-\mathrm{i}2\pi z/\lambda} \begin{bmatrix} \tilde{E}_x e^{\mathrm{i}\delta_x} \\ \tilde{E}_y e^{\mathrm{i}\delta_y} \end{bmatrix}. \tag{3.23}$$

Jones calculus considers only relative changes in amplitude and phase so the constant term $\exp[-\mathrm{i}2\pi z/\lambda]$ is omitted and the relative phase difference $(\delta_x - \delta_y)$ and the normalized light intensity are used. Equation 3.23 is then written as:

$$\mathbf{E} = \begin{bmatrix} E_x \\ E_y \end{bmatrix} = \begin{bmatrix} |E_x| e^{\mathrm{i}(\delta_x - \delta_x)} \\ |E_y| \end{bmatrix}, \qquad |E_x|^2 + |E_y|^2 = 1, \tag{3.24}$$

where $|E_x|$ and $|E_y|$ are normalized electric field amplitudes for the normalized light intensity ($I = 1$). This form of the electric field is called normalized Jones vector $\mathbf{E}$. Table 3.1 summarizes the Jones and Stokes vectors for some states of polarization. The Stokes vectors are described in Section 3.4.

The polarization characteristics of optical elements or the interaction at the boundaries are described by Jones Matrices $\mathbf{J}$, which are 2×2 matrices with complex elements. If a light source interacts with an optical element, this relationship can be written as:

$$\mathbf{E}' = \mathbf{J} \cdot \mathbf{E} = \begin{bmatrix} j_{11} & j_{12} \\ j_{21} & j_{22} \end{bmatrix} \cdot \begin{bmatrix} E_x \\ E_y \end{bmatrix} = \begin{bmatrix} E'_x \\ E'_y \end{bmatrix}, \tag{3.25}$$

where $\mathbf{E}$ and $\mathbf{E}'$ are the Jones vectors of the incident and exit beams and $\mathbf{J}$ is the Jones matrix for the optical element. Table 3.2 summarizes the Jones matrices for some optical elements. If light propagates through Q polarization elements $\mathbf{J}_q$, the total polarization effect $\mathbf{J}_{\text{Total}}$ of cascading Q optical elements is expressed using matrix multiplication as:

$$\mathbf{J}_{\text{Total}} = \prod_{q=1}^{Q} \mathbf{J}_{Q-q+1} = \mathbf{J}_Q \cdot \mathbf{J}_{Q-1} \cdots \mathbf{J}_q \cdots \mathbf{J}_2 \cdot \mathbf{J}_1. \tag{3.26}$$

Jones vectors and Jones matrices provide a mathematical method to describe polarization elements. Jones calculus is used for fully polarized light. For partially polarized light, a 2×2 coherence matrix is used [Bor16] but Mueller calculus uses a convenient method to describe fully polarized, partially polarized, or unpolarized state of light, which is presented in Section 3.4.

Table 3.1: The Jones and Stokes vectors for some states of polarization.

Polarization state	Jones vector	Normalized Stokes vector
Linear polarization at 0°	$\begin{bmatrix}1\\0\end{bmatrix}$	$\begin{bmatrix}1\\1\\0\\0\end{bmatrix}$
Linear polarization at 90°	$\begin{bmatrix}0\\1\end{bmatrix}$	$\begin{bmatrix}1\\-1\\0\\0\end{bmatrix}$
Linear polarization at 45°	$\frac{1}{\sqrt{2}}\begin{bmatrix}1\\1\end{bmatrix}$	$\begin{bmatrix}1\\0\\1\\0\end{bmatrix}$
Linear polarization at 135°	$\frac{1}{\sqrt{2}}\begin{bmatrix}1\\-1\end{bmatrix}$	$\begin{bmatrix}1\\0\\-1\\0\end{bmatrix}$
Right-circular polarization	$\frac{1}{\sqrt{2}}\begin{bmatrix}1\\\mathrm{i}\end{bmatrix}$	$\begin{bmatrix}1\\0\\0\\1\end{bmatrix}$
Left-circular polarization	$\frac{1}{\sqrt{2}}\begin{bmatrix}1\\-\mathrm{i}\end{bmatrix}$	$\begin{bmatrix}1\\0\\0\\-1\end{bmatrix}$

Table 3.2: The Jones matrices for some optical elements.

Optical element	Jones matrix
Free space propagation	$\begin{bmatrix} 1 & 0 \\ 0 & 1 \end{bmatrix}$
Polarizer at angle α	$\begin{bmatrix} \cos^2\alpha & \cos\alpha\sin\alpha \\ \cos\alpha\sin\alpha & \sin^2\alpha \end{bmatrix}$
Compensator*	$\begin{bmatrix} e^{i\delta}\cos^2\alpha + \sin^2\alpha & (e^{i\delta}-1)\cos\alpha\sin\alpha \\ (e^{i\delta}-1)\cos\alpha\sin\alpha & e^{i\delta}\sin^2\alpha + \cos^2\alpha \end{bmatrix}$
Ideal mirror	$\begin{bmatrix} 1 & 0 \\ 0 & -1 \end{bmatrix}$
Sample	$\begin{bmatrix} \sin\Psi\, e^{i\Delta} & 0 \\ 0 & \cos\Psi \end{bmatrix}$
Coordinate rotation	$\begin{bmatrix} \cos\alpha & \sin\alpha \\ -\sin\alpha & \cos\alpha \end{bmatrix}$

*Compensator (or linear retarder) with fast axis at angle α and retardance δ.

3.4 Stokes vectors and Mueller matrices

Jones vectors only describe completely polarized light. In 1852, George Gabriel Stokes showed that the polarization state of light can be described by four measurable quantities (Stokes parameters) [Sto52]. Stokes vectors describe fully polarized light and unpolarized or partially polarized light. Stokes vectors are expressed in terms of the intensity of polarized light as:

$$\mathbf{S} = \begin{bmatrix} S_0 \\ S_1 \\ S_2 \\ S_3 \end{bmatrix} = \begin{bmatrix} I_x + I_y \\ I_x - I_y \\ I_{+45^\circ} - I_{-45^\circ} \\ I_\mathrm{R} - I_\mathrm{L} \end{bmatrix}. \tag{3.27}$$

S_0 is the total intensity of the light beam, I_x and I_y represent the intensity of linear polarized light in the x (0°) and y (90°) directions, I_{+45° and I_{-45° are the intensity of linear polarized light at 45° and −45° and I_R and I_L represent the intensity of right- and left-circular polarization. The Stokes parameters describe unpolarized or partially polarized light, which is characterized by the degree of polarization (DOP) as

$$DOP(\mathbf{S}) = \frac{\sqrt{S_1^2 + S_2^2 + S_3^2}}{S_0}, \qquad 0 \leq DOP \leq 1. \tag{3.28}$$

The DOP for fully polarized light is 1 and the DOP for unpolarized light is 0.

Stokes vectors are normalized to represent polarization states using only polarization-dependent information. The normalized Stokes vector $\hat{\mathbf{S}}$, which

is independent of the absolute intensity, is defined as:

$$\hat{\mathbf{S}} = \frac{\mathbf{S}}{S_0} = \begin{bmatrix} 1 \\ s_1 \\ s_2 \\ s_3 \end{bmatrix}, \qquad 0 \leq s_i \leq 1. \tag{3.29}$$

Table 3.1 shows the Stokes parameters for some polarization states. The normalized Stokes vector for unpolarized light is $[1, 0, 0, 0]^{\mathrm{T}}$, which cannot be described using Jones vectors.

The Mueller matrix was developed by Hans Mueller in the early 1940s. Mueller matrices $\mathbf{M}$ (4×4 matrix) characterize the interaction between polarization elements and polarized light [Shu62]. If a light source interacts with an optical element, this relationship can be written as:

$$\mathbf{S}' = \mathbf{M} \cdot \mathbf{S} = \begin{bmatrix} M_{11} & M_{12} & M_{13} & M_{14} \\ M_{21} & M_{22} & M_{23} & M_{24} \\ M_{31} & M_{32} & M_{33} & M_{34} \\ M_{41} & M_{42} & M_{43} & M_{44} \end{bmatrix} \cdot \begin{bmatrix} S_0 \\ S_1 \\ S_2 \\ S_3 \end{bmatrix} = \begin{bmatrix} S_0' \\ S_1' \\ S_2' \\ S_3' \end{bmatrix}, \tag{3.30}$$

where $\mathbf{S}$ and $\mathbf{S}'$ are the Stokes vectors of the incident and exit beams and $\mathbf{M}$ is the Mueller matrix of the optical element. Table 3.3 summarizes the Mueller matrices for some optical elements. Similarly to Jones calculus, the total polarization effect $\mathbf{M}_{\text{Total}}$ of cascading Q optical elements is described as:

$$\mathbf{M}_{\text{Total}} = \prod_{q=1}^{Q} \mathbf{M}_{Q-q+1} = \mathbf{M}_Q \cdot \mathbf{M}_{Q-1} \cdots \mathbf{M}_q \cdots \mathbf{M}_2 \cdot \mathbf{M}_1. \tag{3.31}$$

Similarly to Stokes vectors, Mueller matrices are normalized to represent polarization states using only polarization-dependent information. The normalized Mueller matrix $\hat{\mathbf{M}}$ is defined as:

$$\begin{aligned}\mathbf{M} &= M_{11}\hat{\mathbf{M}} = M_{11}\begin{bmatrix} 1 & m_{12} & m_{13} & m_{14} \\ m_{21} & m_{22} & m_{23} & m_{24} \\ m_{31} & m_{32} & m_{33} & m_{34} \\ m_{41} & m_{42} & m_{43} & m_{44} \end{bmatrix}, \\ 0 \leq m_{ij} &= \frac{M_{ij}}{M_{11}} \leq 1,\end{aligned} \tag{3.32}$$

where $\hat{\mathbf{M}}$ is the normalized Mueller matrix and M_{11} is the reflectance or transmittance of the optical element for unpolarized light. In terms of the reflection of light, M_{11} equals R:

$$M_{11} = R = \frac{R_\mathrm{p} + R_\mathrm{s}}{2}. \tag{3.33}$$

The normalized Mueller matrix $\hat{\mathbf{M}}$ is used for sample analysis because the elements in the matrix are independent of intensity.

A depolarizer reduces the degree of polarization for light. The Mueller matrix of an ideal depolarizer $\mathbf{M}_\mathrm{ID}$ is expressed as:

$$\mathbf{M}_\mathrm{ID} = \begin{bmatrix} 1 & 0 & 0 & 0 \\ 0 & 0 & 0 & 0 \\ 0 & 0 & 0 & 0 \\ 0 & 0 & 0 & 0 \end{bmatrix}. \tag{3.34}$$

The depolarization index (DI) is used to describe the degree of depolarization for a Mueller matrix. DI is defined as the Euclidean distance, denoted as $\|\cdot\|$,

between the normalized Mueller matrix and ideal depolarizer [Chi18]:

$$DI(\mathbf{M}) := \left\| \frac{\mathbf{M}}{M_{11}} - \mathbf{M}_{\mathrm{ID}} \right\| = \frac{\sqrt{(\sum_{ij} M_{ij}^2) - M_{11}^2}}{\sqrt{3} M_{11}}, \quad 0 \leq DI \leq 1. \tag{3.35}$$

For non-depolarizing Mueller matrices, DI equals 1. If DI for an optical element is 0, the element is an ideal depolarizer and its exit beam becomes unpolarized light.

Figure 3.6 shows the different domains of 4×4 matrices. Mueller matrices are a subset of real 4×4 matrices because Mueller matrices describe physical properties (polarization). Mueller-Jones matrices are matrices that are derived from Jones matrices.

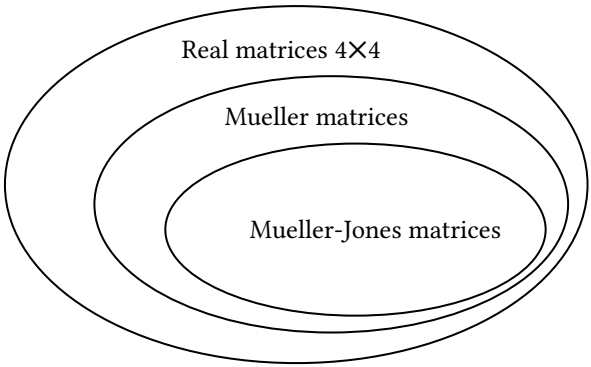

Figure 3.6: Different domains of 4×4 matrices.

A Jones matrix is converted to a Mueller matrix using the transformation [Fuj07]:

$$\mathbf{M} = \mathbf{A}(\mathbf{J} \otimes \mathbf{J}^*)\mathbf{A}^{-1}, \tag{3.36}$$

where $\otimes$ denotes the Kronecker product, the asterisk denotes complex conjugation, and $\mathbf{A}$ is the transformation matrix:

$$\mathbf{A} = \begin{bmatrix} 1 & 0 & 0 & 1 \\ 1 & 0 & 0 & -1 \\ 0 & 1 & 1 & 0 \\ 0 & \mathrm{i} & -\mathrm{i} & 0 \end{bmatrix}. \tag{3.37}$$

In contrast, only non-depolarizing Mueller matrices can be transformed into Jones matrices because Jones matrices only pertain to non-depolarized systems.

Table 3.3: Mueller matrices for some optical elements.

Optical element	Mueller matrix
Free space propagation	$\begin{bmatrix} 1 & 0 & 0 & 0 \\ 0 & 1 & 0 & 0 \\ 0 & 0 & 1 & 0 \\ 0 & 0 & 0 & 1 \end{bmatrix}$
Linear polarizer at angle α	$\frac{1}{2}\begin{bmatrix} 1 & \cos 2\alpha & \sin 2\alpha & 0 \\ \cos 2\alpha & \cos^2 2\alpha & \cos 2\alpha \sin 2\alpha & 0 \\ \sin 2\alpha & \cos 2\alpha \sin 2\alpha & \sin^2 2\alpha & 0 \\ 0 & 0 & 0 & 1 \end{bmatrix}$
Compensator[a]	$\begin{bmatrix} 1 & 0 & 0 & 0 \\ 0 & 1 & 0 & 0 \\ 0 & 0 & \cos\delta & \sin\delta \\ 0 & 0 & -\sin\delta & \cos\delta \end{bmatrix}$
Ideal mirror	$\begin{bmatrix} 1 & 0 & 0 & 0 \\ 0 & 1 & 0 & 0 \\ 0 & 0 & -1 & 0 \\ 0 & 0 & 0 & -1 \end{bmatrix}$
Sample[b]	$R\begin{bmatrix} 1 & -N_\mathrm{M} & 0 & 0 \\ -N_\mathrm{M} & 1 & 0 & 0 \\ 0 & 0 & C_\mathrm{M} & S_\mathrm{M} \\ 0 & 0 & -S_\mathrm{M} & C_\mathrm{M} \end{bmatrix}$
Coordinate rotation	$\begin{bmatrix} 1 & 0 & 0 & 0 \\ 0 & \cos 2\alpha & \sin 2\alpha & 0 \\ 0 & -\sin 2\alpha & \cos 2\alpha & 0 \\ 0 & 0 & 0 & 1 \end{bmatrix}$

[a] Compensator (or linear retarder) with fast axis at 0° and retardance δ.

[b] $R = \frac{1}{2}(R_\mathrm{p} + R_\mathrm{s})$, $N_\mathrm{M} = \cos 2\Psi$, $S_\mathrm{M} = \sin 2\Psi \sin \Delta$ and $C_\mathrm{M} = \sin 2\Psi \cos \Delta$

3.5 Polarization ray tracing

A monochromatic plane electromagnetic wave that propagates along the z axis is described by Jones vectors and Jones matrices in an xy coordinate system. If the wave is not propagating along the z axis, then coordinate transformation is used for the xy coordinate system. The Jones calculus uses a local coordinate, which is determined by the propagation vector, to calculate the polarization properties of optical elements and the polarization state of beams in an optical system. If the ray propagates through many optical elements or curved surfaces (e.g., folded mirrors, corner cubes, spherical and parabolic mirrors), the local coordinate transformation can be complicated.

This section describes the use of polarization ray tracing, which was proposed by Chipman. et al. [Chi18], to analyze the polarization model in a global coordinate system (3D Cartesian coordinates), using orthogonal transformations. Polarization ray tracing calculus uses the global coordinate to analyze polarization properties mathematically. Therefore, there is no need to determine the local coordinate transformation manually, which is tedious and intricate.

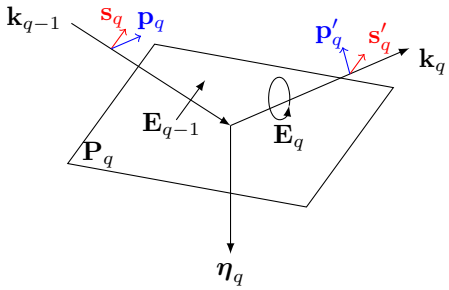

Figure 3.7: Incident and reflected rays follow the propagation vectors ($\mathbf{k}_{q-1}$, $\mathbf{k}_q$) at the qth optical interface and the polarization states ($\mathbf{E}_{q-1}$, $\mathbf{E}_q$). ($\mathbf{s}_q$, $\mathbf{p}_q$, $\mathbf{k}_{q-1}$) and ($\mathbf{s}'_q$, $\mathbf{p}'_q$, $\mathbf{k}_q$) are local coordinate bases for the incident and reflected rays. The local coordinate bases are orthogonal coordinates, as defined in Equation 3.39.

Figure 3.7 shows that an electric field vector $\mathbf{E}_{q-1}$ propagates in direction $\mathbf{k}_{q-1}$ and the exiting electric field vector $\mathbf{E}_q$ is reflected in direction $\mathbf{k}_q$, which

is expressed as:

$$\mathbf{E}_q = \begin{bmatrix} E_{x,q} \\ E_{y,q} \\ E_{z,q} \end{bmatrix} = \mathbf{P}_q \mathbf{E}_{q-1} = \begin{bmatrix} P_{xx,q} & P_{xy,q} & P_{xz,q} \\ P_{yx,q} & P_{yy,q} & P_{yz,q} \\ P_{zx,q} & P_{zy,q} & P_{zz,q} \end{bmatrix} \begin{bmatrix} E_{x,q-1} \\ E_{y,q-1} \\ E_{z,q-1} \end{bmatrix}, \tag{3.38}$$

where (x, y, z) represents the global Cartesian coordinate system, $\mathbf{P}_q$ denotes the polarization transfer matrix, which describes the polarization effect (reflection or refraction) at each interface and q is the number of interfaces. $\mathbf{s}$, $\mathbf{p}$ and $\mathbf{k}$ are local coordinate bases for the light beam. $\mathbf{s}$ and $\mathbf{p}$ are perpendicular and parallel to the POI and $\boldsymbol{\eta}$ is the surface normal. The local coordinate systems for incident and reflected light are respectively defined by $(\hat{\mathbf{s}}_q, \hat{\mathbf{p}}_q, \hat{\mathbf{k}}_{q-1})$ and $(\hat{\mathbf{s}}'_q, \hat{\mathbf{p}}'_q, \hat{\mathbf{k}}_q)$. The normalized vectors are:

$$\begin{aligned} \hat{\mathbf{s}}_q &= \frac{\hat{\mathbf{k}}_{q-1} \times \hat{\boldsymbol{\eta}}_q}{|\hat{\mathbf{k}}_{q-1} \times \hat{\boldsymbol{\eta}}_q|}, \\ \hat{\mathbf{p}}_q &= \hat{\mathbf{k}}_{q-1} \times \hat{\mathbf{s}}_q, \\ \hat{\mathbf{s}}'_q &= \hat{\mathbf{s}}_q, \\ \hat{\mathbf{p}}'_q &= \hat{\mathbf{k}}_q \times \hat{\mathbf{s}}_q, \\ \hat{\mathbf{k}}_q &= \hat{\mathbf{k}}_{q-1} - 2(\hat{\mathbf{k}}_{q-1} \cdot \hat{\boldsymbol{\eta}}_q)\hat{\boldsymbol{\eta}}_q. \end{aligned} \tag{3.39}$$

Equation 3.40 defines the polarization transfer matrix $\mathbf{P}_q$ as:

$$\begin{aligned} \mathbf{P}_q &= \mathbf{O}_{\text{out},q} \mathbf{J}_q^{(3)} \mathbf{O}_{\text{in},q}^{-1} \\ &= \begin{bmatrix} \hat{s}_{x,q} & \hat{p}'_{x,q} & \hat{k}_{x,q} \\ \hat{s}_{y,q} & \hat{p}'_{y,q} & \hat{k}_{y,q} \\ \hat{s}_{z,q} & \hat{p}'_{z,q} & \hat{k}_{z,q} \end{bmatrix} \cdot \begin{bmatrix} j_{11}^{(3)} & j_{12}^{(3)} & 0 \\ j_{21}^{(3)} & j_{22}^{(3)} & 0 \\ 0 & 0 & 1 \end{bmatrix} \cdot \begin{bmatrix} \hat{s}_{x,q} & \hat{s}_{y,q} & \hat{s}_{z,q} \\ \hat{p}_{x,q} & \hat{p}_{y,q} & \hat{p}_{z,q} \\ \hat{k}_{x,q-1} & \hat{k}_{y,q-1} & \hat{k}_{z,q-1} \end{bmatrix}, \end{aligned} \tag{3.40}$$

where $\mathbf{O}_{\text{in},q}^{-1}$ and $\mathbf{O}_{\text{out},q}$ are transformation matrices and $\mathbf{J}_q^{(3)}$ is the 3D Jones matrix (3×3) for the qth interface in local $\hat{\mathbf{s}}$ and $\hat{\mathbf{p}}$ bases. Substituting Equation

3.40 into Equation 3.38 gives the exiting electric field vector $\mathbf{E}_q$ as:

$$\mathbf{E}_q = \mathbf{O}_{\text{out},q}\mathbf{J}_q^{(3)}\mathbf{O}_{\text{in},q}^{-1} \cdot \mathbf{E}_{q-1}. \tag{3.41}$$

The transformation matrix $\mathbf{O}_{\text{in},q}^{-1}$ projects the electric field vector $\mathbf{E}_{q-1}$ onto the local coordinate system $(\hat{\mathbf{s}}_q,\ \hat{\mathbf{p}}_q,\ \hat{\mathbf{k}}_{q-1})$.

$$\mathbf{E}_{\text{sp},q-1} = \mathbf{O}_{\text{in},q}^{-1} \cdot \mathbf{E}_{q-1} = \mathbf{O}_{\text{in},q}^{-1} \begin{bmatrix} E_{x,q-1} \\ E_{y,q-1} \\ E_{z,q-1} \end{bmatrix} = \begin{bmatrix} E_{\text{s},q-1} \\ E_{\text{p},q-1} \\ 0 \end{bmatrix}. \tag{3.42}$$

The transformation matrix $\mathbf{O}_{\text{out},q}$ converts the local coordinate system to the global coordinate system $(\hat{\mathbf{s}}'_q,\ \hat{\mathbf{p}}'_q,\ \hat{\mathbf{k}}_q)$.

$$\mathbf{E}_q = \mathbf{O}_{\text{out},q} \cdot \begin{bmatrix} E_{\text{s},q} \\ E_{\text{p}',q} \\ 0 \end{bmatrix} = E_{\text{s},q}\hat{\mathbf{s}_q} + E_{\text{p}',q}\hat{\mathbf{p}'_q}. \tag{3.43}$$

$\mathbf{P}_q$ for a reflection or refraction at optically isotropic interfaces can be derived by 3D Jones matrices $\mathbf{J}_{\text{r},q}^{(3)}$ and $\mathbf{J}_{\text{t},q}^{(3)}$ as:

$$\begin{aligned} \mathbf{J}_{\text{r},q}^{(3)} &= \begin{bmatrix} r_\text{s} & 0 & 0 \\ 0 & r_\text{p} & 0 \\ 0 & 0 & 1 \end{bmatrix}, \\ \mathbf{J}_{\text{t},q}^{(3)} &= \begin{bmatrix} t_\text{s} & 0 & 0 \\ 0 & t_\text{p} & 0 \\ 0 & 0 & 1 \end{bmatrix}, \end{aligned} \tag{3.44}$$

where r and t indicate reflection and transmission. r_p, r_s, t_p and t_s are amplitude coefficients for reflection and transmission, which are defined in Equations 3.11 and 3.12. Finally, the total polarization effect $\mathbf{P}_{\text{Total}}$ of cascading isotropic optical elements is described as:

$$\mathbf{P}_{\text{Total}} = \prod_{q=1}^{Q} \mathbf{P}_{Q-q+1} = \mathbf{P}_N \mathbf{P}_{N-1} \cdots \mathbf{P}_q \cdots \mathbf{P}_2 \mathbf{P}_1. \tag{3.45}$$

3.6 Ellipsometry

3.6.1 Principles of ellipsometry

In ellipsometric measurements (reflection), polarized light beams impinge onto a sample at an oblique angle which is shown in Figure 3.8. The polarization states of reflection of light can be described by p- and s-polarizations which is introduced in Section 3.2. Ellipsometers measure the change of polarization states between the incident and reflection beams which can be defined as the ratio ρ of the amplitude reflection coefficients for p- and s- polarizations:

$$\rho := \frac{r_p}{r_s} = \left(\frac{E_{rp}}{E_{ip}}\right) / \left(\frac{E_{rs}}{E_{is}}\right) = \tan\Psi e^{i\Delta}. \tag{3.46}$$

For transmission measurements, the ratio ρ of the amplitude transmission coefficients for p- and s- polarizations is defined as

$$\rho := \frac{t_p}{t_s} = \left(\frac{E_{tp}}{E_{ip}}\right) / \left(\frac{E_{ts}}{E_{is}}\right) = \tan\Psi e^{i\Delta}. \tag{3.47}$$

In Equation 3.46, $\tan\Psi$ is the absolute value of the amplitude ratio for p- and s-polarizations ($|r_p| / |r_s|$) and Δ is the phase difference ($\delta_{rp} - \delta_{rs}$), where δ_{rp} and δ_{rs} are the phase changes for p- and s- polarizations after reflection at

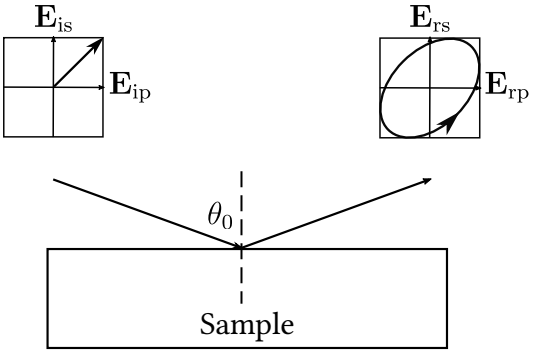

Figure 3.8: Measurement principle for ellipsometry.

the interface.

$$\begin{aligned} \Psi &= \tan^{-1}\left(\frac{|r_p|}{|r_s|}\right) \\ \Delta &= \delta_{rp} - \delta_{rs}. \end{aligned} \tag{3.48}$$

Δ is determined in terms of ρ as:

$$\Delta = \arg(\rho) = \begin{cases} \tan^{-1}[\Im(\rho)/\Re(\rho)], \text{ if } \Re(\rho) > 0 \text{ and } \Im(\rho) \geq 0 \\ \tan^{-1}[\Im(\rho)/\Re(\rho)] + 360°, \text{ if } \Re(\rho) > 0 \text{ and } \Im(\rho) < 0 \\ \tan^{-1}[\Im(\rho)/\Re(\rho)] + 180°, \text{ if } \Re(\rho) < 0 \text{ and } \Im(\rho) \geq 0 \\ \tan^{-1}[\Im(\rho)/\Re(\rho)] + 180°, \text{ if } \Re(\rho) < 0 \text{ and } \Im(\rho) < 0 \end{cases} \tag{3.49}$$

In Equation 3.49, if $\Re(\rho) = 0$, $\Delta = 90°$ ($\Im(\rho) > 0$) and $\Delta = 270°$ ($\Im(\rho) < 0$). Therefore, the ranges of Ψ and Δ are [0°,90°] and [0°,360°].

Figure 3.9 shows a two-phase system (ambient/ substrate), where N_0 and N_1 are the refractive indices of the ambient and the substrate. Usually, air is the ambient space ($N_0 = 1$) and the angle of incidence θ_0 is a known parameter.

Substituting Equation 3.11 into Equation 3.46 gives N_1 as:

$$N_1 = N_0 \tan\theta_0 \sqrt{1 - \frac{4\rho}{(1+\rho)^2} \sin^2\theta_0}. \tag{3.50}$$

After the ellipsometry measurement of Ψ and Δ, the complex refractive index of the substrate N_1 is determined.

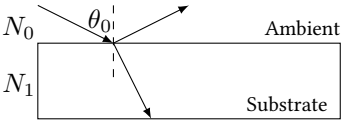

Figure 3.9: Optical model for an ambient(0)-substrate(1) system.

3.6.2 Mueller matrix measurements

Ellipsometry uses null, rotating-analyzer, rotating-compensator and phase-modulation methods, which have different measurable Stokes parameters, measurable regions and measurement times [Fuj07]. Null ellipsometry is the first ellipsometry instrument. The polarization state generator (PSG) includes a linear polarizer and compensator. Changing the rotation angle of the linear polarizer can let the reflected light become linearly polarized. Then, the polarization state analyzer (PSA) uses a rotatable linear polarizer to find the extinction or null condition, i.e., the intensity becomes zero. Finally, the ellipsometric parameters (Ψ, Δ) are determined by the rotation angles of the linear polarizers in the PSG and PSA. The rotating-analyzer method uses a fixed linear polarizer in the PSG and a rotating linear polarizer in the PSA. This configuration can only measure S_0, S_1 and S_2. The measurable regions of Ψ and Δ are $[0°, 90°]$ and $[0°, 180°]$. If a compensator is set in front of the rotating polarizer, S_3 can be measured and the measurable regions of Ψ and Δ become $[0°, 90°]$ and $[0°, 360°]$. The rotating-compensator method comprises a rotating compensator and a fixed linear polarizer in the PSA. The PSG is a fixed linear polarizer. The measured intensity is modulated by the rotating compensator. Therefore, full Stokes parameters (S_0, S_1, S_2 and S_3.)

can be calculated by the Fourier analysis. The measurable regions of Ψ and Δ are $[0°, 90°]$ and $[0°, 360°]$. Phase-modulation ellipsometry includes a PSG (a linear polarizer) and a PSA (a phase modulator and fixed linear polarizer). The measured intensity is modulated by the phase modulator. Full Stokes parameters can be determined with at least two different rotation angles of the modulator by the Fourier analysis. The measurable regions of Ψ and Δ are $[0°, 90°]$ and $[0°, 360°]$.

As described in Section 3.4, the Mueller matrix provides a mathematical method to describe the polarization properties of samples, including the depolarizing effect and anisotropic properties. Mueller matrix ellipsometry has been widely used in the last two decades to determine film thickness and optical constants.

Figure 3.10 shows a schematic diagram of conventional ellipsometry, which uses a PSG and a PSA. The PSG produces different polarization states for light and the PSA measures the polarization state after reflection at the sample. PSGs usually include rotating waveplate, liquid crystal retarders or photoelastic modulators. This study uses the rotating waveplate method for the PSG.

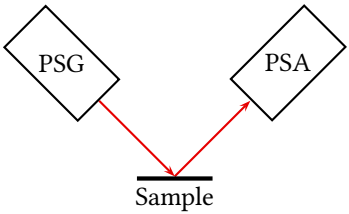

Figure 3.10: A conventional ellipsometer consists of a PSG and a PSA. $\mathbf{S}$ is the Stokes vector from the PSG and $\mathbf{S}'$ is the Stokes vector received by the PSA.

A PSG that consists of a laser, a linear polarizer (LP) and a quarter-waveplate (QWP) is shown in Figure 3.11. The Stokes vector of the laser ($\mathbf{S}_{\text{Laser}}$) is $I_0[1\ 1\ 0\ 0]^{\text{T}}$. The LP is used to extract linearly polarized light and the QWP is a compensator that generates a phase difference (retardance δ) of 90°. The output from the PSG is described using the Stoke vector and the Mueller

Matrix as:

$$\mathbf{S} = \mathbf{M}_{\mathrm{QWP}}(\alpha_{\mathrm{PSG}}) \cdot \mathbf{M}_{\mathrm{LP}} \cdot \mathbf{S}_{\mathrm{Laser}} = \frac{1}{2} I_0 \begin{bmatrix} 1 \\ \cos^2 2\alpha_{\mathrm{PSG}} \\ \cos 2\alpha_{\mathrm{PSG}} \sin 2\alpha_{\mathrm{PSG}} \\ -\sin 2\alpha_{\mathrm{PSG}} \end{bmatrix}, \tag{3.51}$$

where the transmission axis of the linear polarizer is parallel to the x axis and the fast axis orientation of the QWP is at α_{PSG} measured from the x axis. The detailed Mueller matrices for the LP and QWP are shown in Table 3.3. Rotating the QWP produces different polarization states of light.

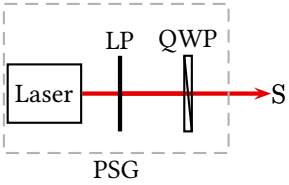

Figure 3.11: A PSG consists of a laser, a linear polarizer (LP) and a quarter-waveplate (QWP). The transmission axis of the linear polarizer is parallel to the x axis and the fast axis orientation of the QWP is α_{PSG}.

There are three types of PSA: time sequential, modulated and division of amplitude and division of aperture [Chi18]. This study uses the time sequential method (rotating waveplate), as shown in Figure 3.12. The measured Stokes vector $\mathbf{S}'$ are expressed as:

$$\mathbf{S}' = \mathbf{M}_{\mathrm{LP}} \cdot \mathbf{M}_{\mathrm{QWP}}(\alpha_{\mathrm{PSA}}) \cdot \mathbf{S}, \tag{3.52}$$

where $\mathbf{S}$ is the input Stokes vector $[S_0\ S_1\ S_2\ S_3]^{\mathrm{T}}$. The total intensity I of $\mathbf{S}'$ is written as:

$$\begin{aligned} I &= \frac{1}{2}(S_0 + \frac{1}{2}S_1 + \frac{1}{2}S_1 \cos 4\alpha_{\mathrm{PSA}} + \frac{1}{2}S_2 \sin 4\alpha_{\mathrm{PSA}} + S_3 \sin 2\alpha_{\mathrm{PSA}}) \\ &= a_0 + b_2 \sin 2\alpha_{\mathrm{PSA}} + a_4 \cos 4\alpha_{\mathrm{PSA}} + b_4 \sin 4\alpha_{\mathrm{PSA}}, \end{aligned} \tag{3.53}$$

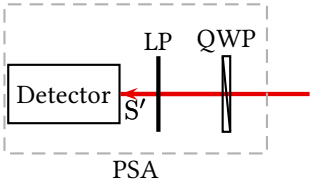

Figure 3.12: A PSA consists of a detector, a linear polarizer (LP) and a quarter-waveplate (QWP). The transmission axis of the linear polarizer is parallel to the x axis and the fast axis orientation of the QWP is α_{PSA}.

where a_0, a_4, b_2 and b_4 are Fourier coefficients. The detector measures a modulated signal (I) over one optical cycle, e.g., the QWP rotates from 0° to 180°, with 50 sample points. The signal is the superposition of sine and cosine waves. Therefore, the Stokes parameters for $\mathbf{S}'$ are determined by Fourier analysis to obtain the Fourier coefficients. A typical method for the discrete Fourier transform is Hadamard analysis. Then, the Stokes parameters can be calculated as:

$$S_0 = 2(a_0 - a_4), S_1 = 4a_4,\ S_2 = 4b_4,\ S_3 = 2b_2. \tag{3.54}$$

Ellipsometry measurements in Figure 3.10 represent the Mueller matrix measurement as:

$$\mathbf{S}' = \mathbf{M}_{\text{Sample}}\mathbf{S}, \tag{3.55}$$

where $\mathbf{S}$ is the Stokes vector for the light from the PSG and $\mathbf{S}'$ is the Stokes vector that is received by the PSA. Since there are 16 elements to be determined in the Mueller matrix for the sample, only four different Stokes vectors that are linearly independent are necessary to determine the Mueller matrix. Moreover, usually more than 4 Stokes vectors are used to calculate the Mueller matrix to obtain stable results. If the PSG generates j Stokes vectors $\mathbf{S}_j$, then

a $4 \times j$ matrix $\mathbf{C}$ is written as:

$$\mathbf{C} := \begin{bmatrix} \mathbf{S}_1 & \mathbf{S}_2 & \mathbf{S}_3 & \cdots & \mathbf{S}_j \end{bmatrix} = \begin{bmatrix} S_{0,1} & S_{0,2} & S_{0,3} & \cdots & S_{0,j} \\ S_{1,1} & S_{1,2} & S_{1,3} & \cdots & S_{1,j} \\ S_{2,1} & S_{2,2} & S_{2,3} & \cdots & S_{2,j} \\ S_{3,1} & S_{3,2} & S_{3,3} & \cdots & S_{3,j} \end{bmatrix}. \quad (3.56)$$

The PSA measures j Stokes vectors $\mathbf{S}'_j$ after j Stokes vectors $\mathbf{S}_j$ reflect from the sample. Then, a $4 \times j$ matrix $\mathbf{D}$ is written as:

$$\mathbf{D} := \begin{bmatrix} \mathbf{S}'_1 & \mathbf{S}'_2 & \mathbf{S}'_3 & \cdots & \mathbf{S}'_j \end{bmatrix} = \begin{bmatrix} S'_{0,1} & S'_{0,2} & S'_{0,3} & \cdots & S'_{0,j} \\ S'_{1,1} & S'_{1,2} & S'_{1,3} & \cdots & S'_{1,j} \\ S'_{2,1} & S'_{2,2} & S'_{2,3} & \cdots & S'_{2,j} \\ S'_{3,1} & S'_{3,2} & S'_{3,3} & \cdots & S'_{3,j} \end{bmatrix}. \quad (3.57)$$

Substituting Equations 3.56 and 3.57 into Equation 3.55 gives the matrix $\mathbf{D}$ as:

$$\mathbf{D} = \mathbf{M}_{\text{Sample}} \cdot \mathbf{C}. \quad (3.58)$$

If more than 4 Stokes vectors are measured, the system is overdetermined and can be solved as a least squares problem. If the rank of matrix $\mathbf{C}$ equals 4 (full rank), the Moore–Penrose inverse $\mathbf{C}^+$ is used to calculate the Mueller matrix for the sample as:

$$\mathbf{M}_{\text{Sample}} = (\mathbf{C}^\dagger \mathbf{C})^{-1} \mathbf{C}^\dagger \mathbf{D} = \mathbf{C}^+ \mathbf{D}. \quad (3.59)$$

4 Retroreflex ellipsometry

This chapter describes retroreflex ellipsometry and a prototype is developed accordingly. Section 4.1 presents the design and components of retroreflex ellipsometry. The polarization analysis of the retroreflector, which is the most critical component in retroreflex ellipsometry, is examined in Section 4.2. Polarization ray tracing for nonplanar surfaces is introduced in Section 4.3. The prototype and system calibration are described in Section 4.4. The development of the retroreflex ellipsometer is summarized in Section 4.5.

4.1 System design

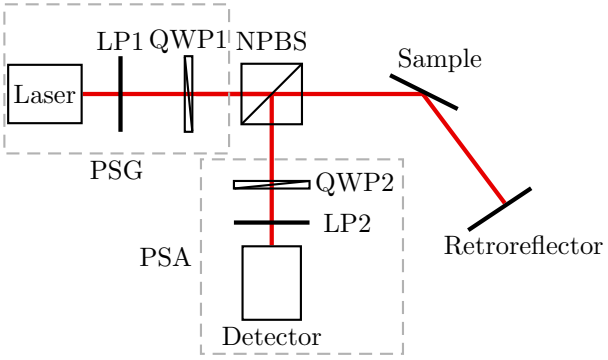

Figure 4.1: Schematic diagram of a retroreflex ellipsometer comprising of PSA, PSG, and NPBS.

Figure 4.1 schematically illustrates Mueller matrix retroreflex ellipsometry. The setup uses the principle of a return-path and dual rotating-compensator ellipsometry [Hag80], wherein a retroreflector returns the light beam from

the sample back onto itself along the same beam path with a phase difference of 180° (i.e., polarization similar to that for an ideal mirror). The light beam from the sample is reflected by the non-polarizing beamsplitter (NPBS) onto the polarization state analyzer (PSA). The polarization state generator (PSG) generates light with different polarization states and the PSA measures the polarization states of light that is reflected from the sample.

The design of the PSG uses the rotating waveplate method, which is described in Section 3.6. The combination of the fixed linear polarizer and a quarter-waveplate generates different polarization states of light. The normalized Stokes parameters (s_1, s_2 and s_3) of the PSG in Equation 3.51 are shown in Figure 4.2.

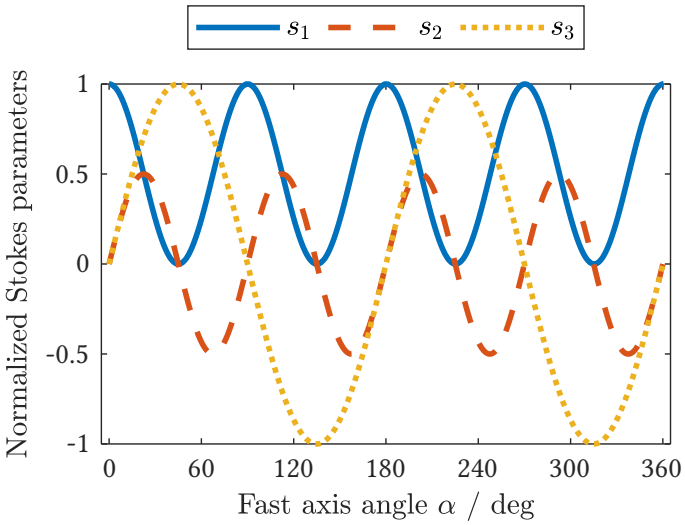

Figure 4.2: Simulation of normalized Stokes parameters generated by the PSG.

The PSA (also called a polarimeter) also uses the rotating waveplate method with a fixed linear polarizer. As described in Section 3.6, the Fourier coefficients are determined using a sequence of intensity measurements over 360°. The Stokes vector is then solved using Equation 3.54. This design of the PSA

is the most common polarimeter for full Stokes parameters determination because the optical configuration is simple and the measurement sensitivity is uniform for ellipsometry parameters (Ψ, Δ) [Fuj07]. However, a mechanical rotating element is required for the QWP. Vibration and misalignment of the rotation center induce measurement errors. The measurement time is also limited by the rotational speed of the rotary stage.

The Mueller matrix model for retroreflex ellipsometry in Figure 4.1 is written as:

$$\begin{aligned}\mathbf{S}' &= \underbrace{\mathbf{M}_{\mathrm{NPBS,r}}\mathbf{M}_{\mathrm{Sample}}\mathbf{M}_{\mathrm{Retro}}\mathbf{M}_{\mathrm{Sample}}}_{\mathbf{M}_{\mathrm{measured}}} \underbrace{\mathbf{M}_{\mathrm{NPBS,t}}\mathbf{M}_{\mathrm{QWP}}\mathbf{M}_{\mathrm{LP}} \cdot \mathbf{S}_{\mathrm{Laser}}}_{\mathbf{S}_{\mathrm{PSG}}} \\ &= \mathbf{M}_{\mathrm{measured}}\mathbf{S}_{\mathrm{PSG}},\end{aligned} \tag{4.1}$$

where $\mathbf{S}_{\mathrm{Laser}}$ and $\mathbf{S}'$ denote the Stokes vector for the laser and the Stokes vector that is measured by the PSA, respectively. $\mathbf{M}_{\mathrm{NPBS,t}}$ and $\mathbf{M}_{\mathrm{NPBS,r}}$ are the Mueller matrices of transmission and reflection of the NPBS. $\mathbf{M}_{\mathrm{Retro}}$ is the Mueller matrix for the retroreflector, which is identical to the Mueller matrix for an ideal mirror:

$$\mathbf{M}_{\mathrm{Retro}} = \mathbf{M}_{\mathrm{Mirror}} = \begin{bmatrix} 1 & 0 & 0 & 0 \\ 0 & 1 & 0 & 0 \\ 0 & 0 & -1 & 0 \\ 0 & 0 & 0 & -1 \end{bmatrix}. \tag{4.2}$$

This system is suited to inline or in-situ measurements because the PSG and the PSA can be integrated into a single unit on one arm. This device is also more sensitive to the optical properties of surfaces than conventional ellipsometers because the interaction between the light beam and the sample (reflection or transmission) occurs twice, on the path to the retroreflector and the path back to the PSA. This configuration can also be easily applied to reflection or transmission measurements because the retroreflector allows flexible installation and tolerances are loose.

4.2 Polarization characteristics of the retroreflector

To measure nonplanar surfaces, a retroreflector (retroreflective sheet) is used to return the light beam back to the sample along the same beam path. The retroreflective sheet consists of many tiny spherical glass beads that reflect the light beam. Figure 4.3 shows a microscope image of a retroreflective sheet. The spherical glass beads are placed randomly and their diameters vary between about 50 µm and 100 µm. This type of the retroreflector is also called a cat's eye retroreflector and produces an effect that is similar to the red-eye effect in flash photography. There are two types of retroreflectors: cat's eye and corner cube. However, the polarization characteristics of the latter retroreflector are strongly dependent on the incidence angle and the incidence zones [Seg03, Kal07]. For the former retroreflector, if the incident angle is less than 12°, the glass bead type (cat's eye) reflects polarized light with a phase shift of 180° [Ste85, Li19].

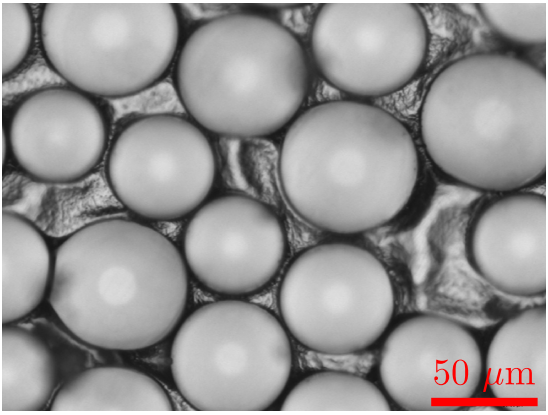

Figure 4.3: Microscopic image of the retroreflector.

The cat's eye retroreflector is widely used as a laser tracker for precision alignment [May93]. There are many studies involving wavefronts [Bee66], ray

tracing [Yan00] and efficiency analysis [Yan12] but only some studies determine the polarization properties of the cat's eye retroreflector [Zho11, Li19, Neg23].

Figure 4.4 shows a schematic diagram of a cat's eye retroreflector with radius r and the refractive index of the glass bead is 2. Two refractions and one reflection respectively occur at points A, C and B. The input beam is parallel to the z axis and the input beam height is h so the angle of incidence is calculated as:

$$\theta_0 = \sin^{-1}(\frac{h}{r}), \tag{4.3}$$

where h/r indicates the normalized incident height of the cat's eye retroreflector and the range is [0, 1].

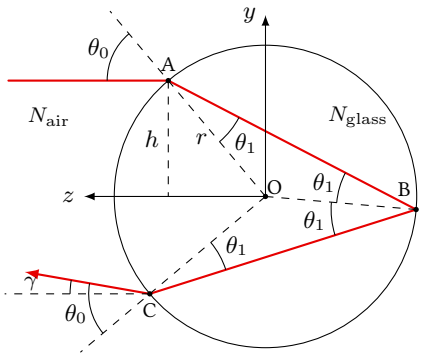

Figure 4.4: Schematic diagram of a cat's eye retroreflector. The refractive indices of air (N_{air}) and the glass bead (N_{glass}) are 1 and 2, respectively.

The deflection angle γ is derived by ray tracing as:

$$\begin{aligned}\gamma &= (4\theta_1 - \theta_0) - \theta_0 \\ &= 4\sin^{-1}(\frac{h}{2r}) - 2\sin^{-1}(\frac{h}{r}).\end{aligned} \tag{4.4}$$

Figure 4.5 illustrates the relationship between γ and h/r. The deflection angle increases with the h/r ratio. At a distance z ($z \gg r$), the offset distance along

the y direction is:

$$\text{Offset} \approx z \sin \gamma. \tag{4.5}$$

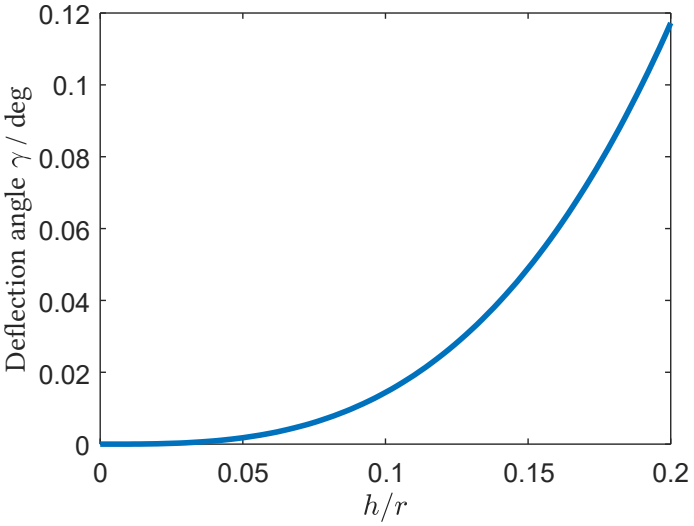

Figure 4.5: Deflection angle γ for a Cat's eye retroreflector as a function of h/r ratio.

Figure 4.6 shows the offset distance at a distance z from 0 to 200 mm for $h/r = 0.1$, $h/r = 0.15$ and $h/r = 0.2$. Table 4.1 lists the numerical values of the incident angle θ_0, the deflection angle γ and the offset distances at distances z of 100 mm and 200 mm for $h/r = 0.1$, $h/r = 0.15$ and $h/r = 0.2$.

Table 4.1: Numerical values of the incident angle θ_0, the deflection angle γ and the offset distances ($z = 100$ mm and $z = 200$ mm) for $h/r = 0.1$, $h/r = 0.15$ and $h/r = 0.2$.

h/r	AOI θ_0	γ	Offset (100 mm)	Offset (200 mm)
0.10	5.74°	0.01° (0.25 mrad)	0.03 mm	0.05 mm
0.15	8.63°	0.05° (0.85 mrad)	0.09 mm	0.17 mm
0.20	11.54°	0.12° (2.05 mrad)	0.20 mm	0.41 mm

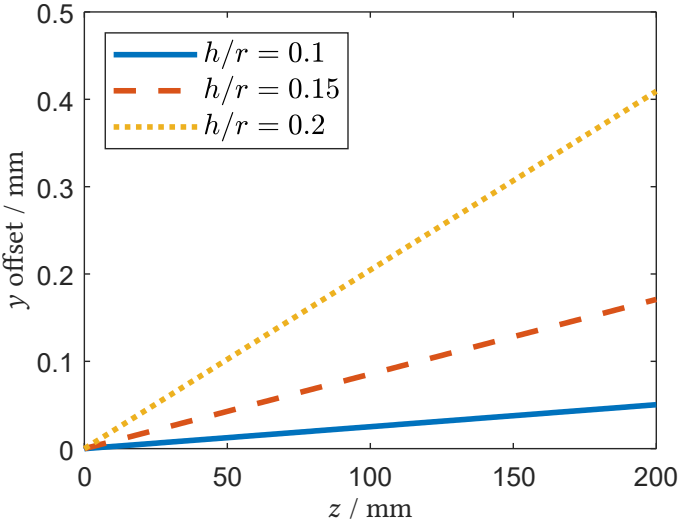

Figure 4.6: Offset y distances at a distance z from 0 to 200 mm for $h/r = 0.1$, $h/r = 0.15$ and $h/r = 0.2$

For $h/r = 0.2$, the maximum offset at a distance z of 200 mm is 0.41 mm. However, on the return path, there are two reflections due to the sample and NPBS (see Figure 4.1). There is an optical lever so the deflection angle increases 4-fold and the offset at the detector is about 1.64 mm.

In the prototype for retroreflex ellipsometry, the free space aperture for the polarimeter (PSA) is 3 mm (diameter). Therefore, it is assumed that the polarimeter receives the light beam when the height of the normalized incident beam is less than 0.2. The following analysis for polarization characteristics only considers the case of $h/r < 0.2$. Due to the intellectual property for the retroreflector, the refractive index of each interface is not known. Previous studies show that the refractive index of the glass bead is close to 2 [Yan00, Li19]. Therefore, the glass beads are assumed to have a refractive index of 2 in this analysis.

4.2.1 Small-angle approximation

For $h/r < 0.2$, the maximum incident angle is 11.54°. The small-angle approximation is used to calculate the Fresnel coefficients of the refraction and reflection at the interfaces. The approximation is listed below.

$$\begin{aligned} &\sin\theta \approx \theta, \\ &\cos\theta \approx 1. \end{aligned} \tag{4.6}$$

At an incident angle of 11.54°, the relative errors in $\sin\theta$ and $\cos\theta$ are 0.7% and 2.0%. Substituting $\sin^2\theta_t + \cos^2\theta_t = 1$ into Equation 3.8 (Snell's law) gives:

$$\cos\theta_t = \sqrt{1 - \frac{N_i^2}{N_t^2}\sin^2\theta_i}. \tag{4.7}$$

Substituting Equation 4.7 into the ratio for the amplitude transmission coefficients in Equation 3.47 gives $\rho_{\text{Refraction}}$:

$$\rho_{\text{Refraction}} = \frac{t_p}{t_s} = \frac{N_i\cos\theta_i + N_t\sqrt{1 - \frac{N_i^2}{N_t^2}\sin^2\theta_i}}{N_t\cos\theta_i + N_i\sqrt{1 - \frac{N_i^2}{N_t^2}\sin^2\theta_i}}. \tag{4.8}$$

In terms of the refraction at point A in Figure 4.4, $N_i = 1$, $N_t = 2$ and $N_i^2\sin^2\theta_i/N_t^2 \approx 0$ so the approximation of the inner term in Equation 4.8 is

$$\sqrt{1 - \frac{N_i^2}{N_t^2}\sin^2\theta_i} \approx 1. \tag{4.9}$$

Equation 4.8 can then be simplified as:

$$\begin{aligned} \rho_{\text{Refraction,A}} &= \frac{N_i + N_t}{N_t + N_i} = 1 \\ &= \tan(45°)e^{i0°}. \end{aligned} \tag{4.10}$$

Substituting the result ($\Psi = 45°$ and $\Delta = 0°$) into the Mueller matrix for the sample in Table 3.3 gives the Mueller matrix of the refraction at point A and the ellipsometric parameters (Ψ, Δ) are calculated using Equations 3.48 and 3.49:

$$\mathbf{M}_{\text{Refraction, A}} = \begin{bmatrix} 1 & 0 & 0 & 0 \\ 0 & 1 & 0 & 0 \\ 0 & 0 & 1 & 0 \\ 0 & 0 & 0 & 1 \end{bmatrix}. \tag{4.11}$$

In terms of the refraction at point C, $N_i = 2$ and $N_t = 1$, a similar approximation in Equation 4.9 is applied and the Mueller matrix for the refraction at point C is shown as:

$$\mathbf{M}_{\text{Refraction, C}} = \begin{bmatrix} 1 & 0 & 0 & 0 \\ 0 & 1 & 0 & 0 \\ 0 & 0 & 1 & 0 \\ 0 & 0 & 0 & 1 \end{bmatrix}. \tag{4.12}$$

In terms of the reflection at point B, substituting Equation 4.7 into the ratio of the amplitude reflection coefficients in Equation 3.46 gives $\rho_{\text{Reflection}}$ as:

$$\begin{aligned} \rho_{\text{Reflection,B}} &= \frac{r_p}{r_s} \\ &= \frac{N_t \cos\theta_i - N_i\sqrt{1 - \frac{N_i^2}{N_t^2}\sin^2\theta_i}}{N_t \cos\theta_i + N_i\sqrt{1 - \frac{N_i^2}{N_t^2}\sin^2\theta_i}} \frac{N_i \cos\theta_i + N_t\sqrt{1 - \frac{N_i^2}{N_t^2}\sin^2\theta_i}}{N_i \cos\theta_i - N_t\sqrt{1 - \frac{N_i^2}{N_t^2}\sin^2\theta_i}}. \end{aligned} \tag{4.13}$$

In this case, $N_i = 2$ and $N_t = 1$. The condition in Equations 4.6 and 4.9 is also applied. Then $\rho_{\text{Reflection, B}}$ can be simplified and the Mueller matrix for the reflection is shown as follows:

$$\begin{aligned} \rho_{\text{Reflection,B}} &= \frac{N_t - N_i}{N_t + N_i}\frac{N_i + N_t}{N_i - N_t} = -1 \\ &= \tan(45°)e^{i180°}. \end{aligned} \tag{4.14}$$

$$\mathbf{M}_{\text{Reflection,B}} = \begin{bmatrix} 1 & 0 & 0 & 0 \\ 0 & 1 & 0 & 0 \\ 0 & 0 & -1 & 0 \\ 0 & 0 & 0 & -1 \end{bmatrix}. \tag{4.15}$$

Finally, the Mueller matrix for the retroreflector is written as:

$$\begin{aligned} \mathbf{M}_{\text{Retroreflector}} &= \mathbf{M}_{\text{Refraction,C}} \cdot \mathbf{M}_{\text{Reflection,B}} \cdot \mathbf{M}_{\text{Refraction,A}} \\ &= \begin{bmatrix} 1 & 0 & 0 & 0 \\ 0 & 1 & 0 & 0 \\ 0 & 0 & -1 & 0 \\ 0 & 0 & 0 & -1 \end{bmatrix}. \end{aligned} \tag{4.16}$$

At small angles of incidence ($\theta_0 \leqslant 11.54°$), the refraction does not change the polarization state of the incident beam and the reflection is similar to that in an ideal mirror. The total polarization characteristics of the retroreflector are approximately the same as those for an ideal mirror.

4.2.2 Numerical simulation

In order to obtain a more accurate result, a numerical simulation without the small-angle approximation is applied. The ratio of the amplitude reflection coefficients for the retroreflector can be written as:

$$\rho_{\text{Retroreflector}} = \rho_{\text{Refraction,C}} \cdot \rho_{\text{Reflection,B}} \cdot \rho_{\text{Refraction,A}}. \tag{4.17}$$

Using the assumed refractive indices, the simulation values (Ψ and Δ) for the retroreflector are shown in Figure 4.7. The maximum error in Ψ is are $-0.88°$ at h/r of 0.2 and there is no error in Δ. A polarimeter measures light beams from $h/r = 0$ to $h/r = 0.2$ so the average values for Ψ and Δ are 44.71° and 180.00°, respectively. Substituting average values into the Mueller matrix for

the sample gives the simulated Mueller matrix for the retroreflector as:

$$\mathbf{M}_{\text{Retroreflector}} = \begin{bmatrix} 1 & -0.01 & 0 & 0 \\ -0.01 & 1 & 0 & 0 \\ 0 & 0 & -1 & 0 \\ 0 & 0 & 0 & -1 \end{bmatrix}. \tag{4.18}$$

The result of the numerical simulation is similar to the result of small-angle approximation. The maximum deviation of the Mueller matrix of an ideal retroreflector is 0.01.

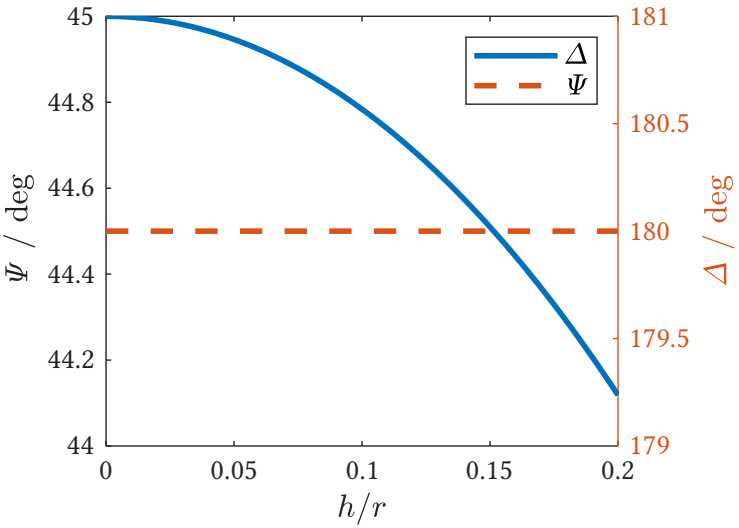

Figure 4.7: Simulation values of Ψ and Δ for the retroreflector based on the assumed refractive indices.

4.2.3 Experimental validation

In order to verify the polarization characteristics of the retroreflector, a commercial spectroscopic ellipsometer (Smart SE, HORIBA Scientific) is used to measure the retroreflector for incident angles from 0° to 30°. The accuracy of

the ellipsometer for the straight-through measurement (air) is $\Psi = 45° \pm 0.05°$ and $\Delta = 180° \pm 0.2°$.

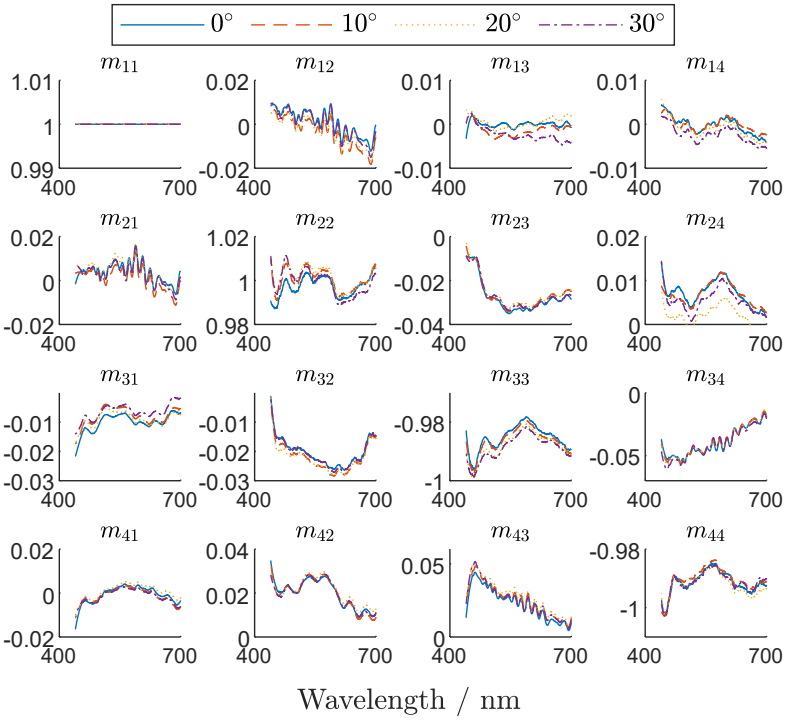

Figure 4.8: Measurement results for the retroreflector using a commercial spectroscopic ellipsometer. The incident angle ranges from 0° to 30°.

The measurement result is shown in Figure 4.8. The maximum deviation in each Mueller matrix element is less than 0.05 between 400 nm to 700 nm and the Mueller matrices are similar to the Mueller matrix for an ideal mirror for an incident angle of less than 30°. The Mueller matrix for the retroreflector

at a wavelength of 635 nm is listed as

$$\mathbf{M}_{\text{Retroreflector},635} = \begin{bmatrix} 1. & -0.008 & 0. & -0.001 \\ -0.004 & 0.993 & -0.031 & 0.006 \\ -0.010 & -0.025 & -0.984 & -0.028 \\ 0.001 & 0.016 & 0.013 & -0.993 \end{bmatrix}. \tag{4.19}$$

The standard deviation (SD) σ for the Mueller matrix elements at different incident angles for a wavelength of 635 nm is shown as:

$$\mathbf{M}_{\sigma,635} = \begin{bmatrix} 0. & 0.002 & 0.002 & 0.001 \\ 0.002 & 0.002 & 0.001 & 0.001 \\ 0.002 & 0.001 & 0.001 & 0.002 \\ 0.001 & 0.002 & 0.001 & 0.001 \end{bmatrix}. \tag{4.20}$$

The experimental results are in good agreement with the simulation results using the small-angle approximation and numerical analysis. The standard deviation shows that the retroreflector has good polarization-preserving properties at incidence angles between 0° to 30°.

4.3 Polarization ray tracing for nonplanar surfaces

Jones or Mueller calculus is used to describe ellipsometric measurements. For planar surfaces, the plane of incidence (POI), which is defined by the incident ray and the surface normal, is fixed and the ellipsometer is calibrated under this coordinate system. If the sample is curved or tilted, the POI alters because the surface normal changes. Therefore, the ellipsometric measurements for nonplanar surfaces require additional coordinate transformation to obtain correct results. In this section, polarization ray tracing, which is described in Section 3.5, is used to determine the coordinate transformation.

Figure 4.9 demonstrates a measurement schematic of retroreflex ellipsometry for a flat sample defining the xy plane whose surface normal is $(0, 0, 1)^{\mathrm{T}}$. When the sample rotates around the y axis, the surface normal $\mathbf{n}$ becomes the vector $(\sin\phi, 0, \cos\phi)^{\mathrm{T}}$. The tilt angle ϕ is defined as that between the surface normal $\mathbf{n}$ and the z axis, and the angle of incidence θ_0 as that between the surface normal $\mathbf{n}$ and the incident beam $\mathbf{k}_0$. The nominal angle of incidence θ' is the angle between the z axis and the incident beam $\mathbf{k}_0$. The relationship between θ_0, θ' and ϕ is shown as:

$$\cos\theta_0 = \cos\theta' \cos\phi. \tag{4.21}$$

If ϕ is 0, θ_0 equals θ', i.e., the sample is aligned and the measurement is under a calibrated coordinate system. In the measurement, the incident beam is reflected by the sample ($q = 1$), retroreflector ($q = 2$) and sample ($q = 3$), respectively. The net polarization transfer matrix $\mathbf{P}_{\mathrm{Total}}$ is expressed as:

$$\mathbf{P}_{\mathrm{Total}} = \mathbf{O}_{\mathrm{out},3}\mathbf{J}_3^{(3)}\mathbf{O}_{\mathrm{in},3}^{-1} \cdot \mathbf{O}_{\mathrm{out},2}\mathbf{J}_2^{(3)}\mathbf{O}_{\mathrm{in},2}^{-1} \cdot \mathbf{O}_{\mathrm{out},1}\mathbf{J}_1^{(3)}\mathbf{O}_{\mathrm{in},1}^{-1}. \tag{4.22}$$

The Jones matrices of the optically isotropic sample and retroreflector (ideal mirror) are shown in Table 3.2. It is worth mentioning that the Jones matrices $\mathbf{J}$ in Section 3.3 are defined in local x and y bases, which correspond to $\hat{\mathbf{p}}$ and $\hat{\mathbf{s}}$ bases. The 3D Jones matrix $\mathbf{J}^{(3)}$ for a reflection at an optically isotropic

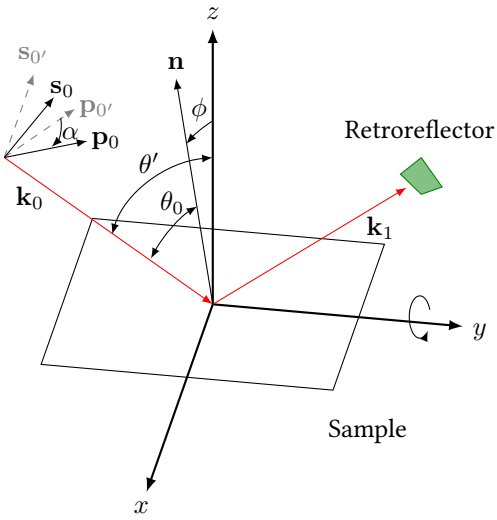

Figure 4.9: Schematic diagram of a flat sample rotates around the y axis. The incident beam follows the direction $\mathbf{k}_0$ is reflected by the sample, retroreflector and sample, respectively.

interface, defined in local $\hat{\mathbf{s}}$, $\hat{\mathbf{p}}$ and $\hat{\mathbf{k}}$ bases, is expressed as:

$$\mathbf{J}^{(3)} = \begin{bmatrix} j_{11}^{(3)} & 0 & 0 \\ 0 & j_{22}^{(3)} & 0 \\ 0 & 0 & 1 \end{bmatrix}, \tag{4.23}$$

where $j_{11}^{(3)} = j_{22}$ and $j_{22}^{(3)} = j_{11}$. Hence, the 3D Jones matrices of the optically isotropic sample and retroreflector are written as:

$$\mathbf{J}_{\text{Sample}}^{(3)} = \mathbf{J}_1^{(3)} = \mathbf{J}_3^{(3)} = \begin{bmatrix} \cos\Psi & 0 & 0 \\ 0 & \sin\Psi \exp[\mathrm{i}\Delta] & 0 \\ 0 & 0 & 1 \end{bmatrix}, \tag{4.24}$$

$$\mathbf{J}_{\text{Retro}}^{(3)} = \mathbf{J}_{\text{Mirror}}^{(3)} = \mathbf{J}_2^{(3)} = \begin{bmatrix} -1 & 0 & 0 \\ 0 & 1 & 0 \\ 0 & 0 & 1 \end{bmatrix}, \tag{4.25}$$

The 3D Jones matrix of the coordinate rotation is expressed as:

$$\mathbf{J}_{\mathrm{R}}^{(3)}(\alpha) = \begin{bmatrix} \cos\alpha & \sin\alpha & 0 \\ -\sin\alpha & \cos\alpha & 0 \\ 0 & 0 & 1 \end{bmatrix}. \tag{4.26}$$

Following the ray tracing method described in Section 3.5, the propagation vectors, surface normals and local coordinate basis vectors are listed in Table 4.2. The inner terms $\mathbf{O}_{\mathrm{in},3}^{-1}\mathbf{O}_{\mathrm{out},2}\mathbf{J}_{2}^{(3)}\mathbf{O}_{\mathrm{in},2}^{-1}\mathbf{O}_{\mathrm{out},1}$ in Equation 4.22 can be simplified as $\mathbf{J}_{\mathrm{Retro}}^{(3)}$. Then Equation 4.22 is written as:

$$\mathbf{P} = \mathbf{O}_{\mathrm{out},3}\mathbf{J}_{\mathrm{Sample}}^{(3)}\mathbf{J}_{\mathrm{Retro}}^{(3)}\mathbf{J}_{\mathrm{Sample}}^{(3)}\mathbf{O}_{\mathrm{in},1}^{-1}. \tag{4.27}$$

In addition, $\mathbf{O}_{\mathrm{in},1}^{-1}$ can be decomposed into the product of a rotation matrix $\mathbf{J}_{\mathrm{R}}^{(3)}(\alpha_1)$ and a local coordinate transformation matrix $\mathbf{O}_{\mathrm{in}(\phi=0),1}$ and $\mathbf{O}_{\mathrm{out},3}$ can be decomposed into the product of a local coordinate transformation matrix $\mathbf{O}_{\mathrm{out}(\phi=0),3}$ and a rotation matrix $\mathbf{J}_{\mathrm{R}}^{(3)}(\alpha_3)$ as following:

$$\begin{aligned}
\mathbf{O}_{\mathrm{in},1}^{-1} &= \begin{bmatrix} \frac{-\cos\phi\sin\theta'}{\sqrt{\cos^2\phi\sin^2\theta'+\sin^2\phi}} & \frac{\sin\phi\cos\theta'}{\sqrt{\cos^2\phi\sin^2\theta'+\sin^2\phi}} & \frac{\sin\phi\sin\theta'}{\sqrt{\cos^2\phi\sin^2\theta'+\sin^2\phi}} \\ \frac{\sin\phi}{\sqrt{\cos^2\phi\sin^2\theta'+\sin^2\phi}} & \frac{\cos\phi\sin\theta'\cos\theta'}{\sqrt{\cos^2\phi\sin^2\theta'+\sin^2\phi}} & \frac{\cos\phi\sin^2\theta'}{\sqrt{\cos^2\phi\sin^2\theta'+\sin^2\phi}} \\ 0 & \sin\theta' & -\cos\theta' \end{bmatrix} \\
&= \begin{bmatrix} \frac{\cos\phi\sin\theta'}{\sqrt{\cos^2\phi\sin^2\theta'+\sin^2\phi}} & \frac{\sin\phi}{\sqrt{\cos^2\phi\sin^2\theta'+\sin^2\phi}} & 0 \\ \frac{-\sin\phi}{\sqrt{\cos^2\phi\sin^2\theta'+\sin^2\phi}} & \frac{\cos\phi\sin\theta'}{\sqrt{\cos^2\phi\sin^2\theta'+\sin^2\phi}} & 0 \\ 0 & 0 & 1 \end{bmatrix} \cdot \begin{bmatrix} -1 & 0 & 0 \\ 0 & \cos\theta' & \sin\theta' \\ 0 & \sin\theta' & -\cos\theta' \end{bmatrix} \\
&= \mathbf{J}_{\mathrm{R}}^{(3)}(\alpha_1) \cdot \mathbf{O}_{\mathrm{in}(\phi=0),1},
\end{aligned} \tag{4.28}$$

$$\mathbf{O}_{\text{out},3} = \begin{bmatrix} \frac{-\cos\phi\sin\theta'}{\sqrt{\cos^2\phi\sin^2\theta'+\sin^2\phi}} & \frac{-\sin\phi}{\sqrt{\cos^2\phi\sin^2\theta'+\sin^2\phi}} & 0 \\ \frac{\sin\phi\cos\theta'}{\sqrt{\cos^2\phi\sin^2\theta'+\sin^2\phi}} & \frac{-\cos\phi\sin\theta'\cos\theta'}{\sqrt{\cos^2\phi\sin^2\theta'+\sin^2\phi}} & -\sin\theta' \\ \frac{\sin\phi\sin\theta'}{\sqrt{\cos^2\phi\sin^2\theta'+\sin^2\phi}} & \frac{-\cos\phi\sin^2\theta'}{\sqrt{\cos^2\phi\sin^2\theta'+\sin^2\phi}} & \cos\theta' \end{bmatrix}$$

$$= \begin{bmatrix} -1 & 0 & 0 \\ 0 & -\cos\theta' & -\sin\theta' \\ 0 & -\sin\theta' & \cos\theta' \end{bmatrix} \cdot \begin{bmatrix} \frac{\cos\phi\sin\theta'}{\sqrt{\cos^2\phi\sin^2\theta'+\sin^2\phi}} & \frac{\sin\phi}{\sqrt{\cos^2\phi\sin^2\theta'+\sin^2\phi}} & 0 \\ \frac{-\sin\phi}{\sqrt{\cos^2\phi\sin^2\theta'+\sin^2\phi}} & \frac{\cos\phi\sin\theta'}{\sqrt{\cos^2\phi\sin^2\theta'+\sin^2\phi}} & 0 \\ 0 & 0 & 1 \end{bmatrix}$$

$$= \mathbf{O}_{\text{out}(\phi=0),3} \cdot \mathbf{J}_{\text{R}}^{(3)}(\alpha_3), \tag{4.29}$$

where $\tan\alpha_1 = \tan\alpha_3 = \tan\phi/\sin\theta'$.

It can be observed from Equations 4.28 and 4.29 that α_1 and α_3 have the same value and sign. In addition, $\mathbf{O}_{\text{in}(\phi=0),1}$ and $\mathbf{O}_{\text{out}(\phi=0),3}$ represent the coordinate transformation when the tilt angle is 0, i.e., the calibrated ellipsometer for flat samples is based on the coordinate transformation $\mathbf{O}_{\text{in}(\phi=0),1}$ and $\mathbf{O}_{\text{out}(\phi=0),3}$. Substituting Equation 4.28 and 4.29 into Equation 4.22 gives the polarization model of tilted surfaces.

$$\mathbf{P} = \mathbf{O}_{\text{out}(\phi=0),3} \cdot \mathbf{J}_{\text{R}}^{(3)}(\alpha)\mathbf{J}_{\text{Sample}}^{(3)}\mathbf{J}_{\text{Retro}}^{(3)}\mathbf{J}_{\text{Sample}}^{(3)}\mathbf{J}_{\text{R}}^{(3)}(\alpha) \cdot \mathbf{O}_{\text{in}(\phi=0),1}, \tag{4.30}$$

where $\alpha_1 = \alpha_3 = \alpha$.

Table 4.2: Propagation vectors $\hat{\mathbf{k}}$, surface normal vectors $\hat{\boldsymbol{\eta}}$ and local coordinate basis vectors ($\hat{\mathbf{s}}$, $\hat{\mathbf{p}}$, $\hat{\mathbf{s}}'$, $\hat{\mathbf{p}}'$) associated with the measurement of the retroreflex ellipsometer.

q	$\hat{\mathbf{k}}_{q-1}$	$\hat{\boldsymbol{\eta}}_q$	$\hat{\mathbf{s}}_q$ ($\hat{\mathbf{s}}'_q$)	$\hat{\mathbf{p}}_q$	$\hat{\mathbf{k}}_q$	$\hat{\mathbf{p}}'_q$
1	$\begin{bmatrix} 0 \\ \sin\theta' \\ -\cos\theta' \end{bmatrix}$	$\begin{bmatrix} -\sin\phi \\ 0 \\ -\cos\phi \end{bmatrix}$	$\begin{bmatrix} \frac{-\cos\phi\sin\theta'}{\sqrt{\cos^2\phi\sin^2\theta'+\sin^2\phi}} \\ \frac{\sin\phi\cos\theta'}{\sqrt{\cos^2\phi\sin^2\theta'+\sin^2\phi}} \\ \frac{\sin\phi\sin\theta'}{\sqrt{\cos^2\phi\sin^2\theta'+\sin^2\phi}} \end{bmatrix}$	$\begin{bmatrix} \frac{\sin\phi}{\sqrt{\cos^2\phi\sin^2\theta'+\sin^2\phi}} \\ \frac{\cos\phi\sin\theta'\cos\theta'}{\sqrt{\cos^2\phi\sin^2\theta'+\sin^2\phi}} \\ \frac{\cos\phi\sin^2\theta'}{\sqrt{\cos^2\phi\sin^2\theta'+\sin^2\phi}} \end{bmatrix}$	$\begin{bmatrix} \cos\theta'\sin 2\phi \\ \sin\theta' \\ \cos\theta'\cos 2\phi \end{bmatrix}$	$\begin{bmatrix} \frac{\sin\phi\left(\sin^2\theta'-\cos^2\theta'\cos 2\phi\right)}{\sqrt{\cos^2\phi\sin^2\theta'+\sin^2\phi}} \\ \frac{-\cos\phi\sin\theta'\cos\theta'}{\sqrt{\cos^2\phi\sin^2\theta'+\sin^2\phi}} \\ \frac{\cos\phi\sin^2\theta'+\cos^2\theta'\sin\phi\sin 2\phi}{\sqrt{\cos^2\phi\sin^2\theta'+\sin^2\phi}} \end{bmatrix}$
2	$\begin{bmatrix} \cos\theta'\sin 2\phi \\ \sin\theta' \\ \cos\theta'\cos 2\phi \end{bmatrix}$	$\begin{bmatrix} \cos\theta'\sin 2\phi \\ \sin\theta' \\ \cos\theta'\cos 2\phi \end{bmatrix}$	$\begin{bmatrix} \frac{-\cos\phi\sin\theta'}{\sqrt{\cos^2\phi\sin^2\theta'+\sin^2\phi}} \\ \frac{\sin\phi\cos\theta'}{\sqrt{\cos^2\phi\sin^2\theta'+\sin^2\phi}} \\ \frac{\sin\phi\sin\theta'}{\sqrt{\cos^2\phi\sin^2\theta'+\sin^2\phi}} \end{bmatrix}$	$\begin{bmatrix} \frac{\sin\phi\left(\sin^2\theta'-\cos^2\theta'\cos 2\phi\right)}{\sqrt{\cos^2\phi\sin^2\theta'+\sin^2\phi}} \\ \frac{-\cos\phi\sin\theta'\cos\theta'}{\sqrt{\cos^2\phi\sin^2\theta'+\sin^2\phi}} \\ \frac{\cos\phi\sin^2\theta'+\cos^2\theta'\sin\phi\sin 2\phi}{\sqrt{\cos^2\phi\sin^2\theta'+\sin^2\phi}} \end{bmatrix}$	$\begin{bmatrix} -\cos\theta'\sin 2\phi \\ -\sin\theta' \\ -\cos\theta'\cos 2\phi \end{bmatrix}$	$\begin{bmatrix} \frac{\sin\phi\left(\cos^2\theta'\cos 2\phi-\sin^2\theta'\right)}{\sqrt{\cos^2\phi\sin^2\theta'+\sin^2\phi}} \\ \frac{\cos\phi\sin\theta'\cos\theta'}{\sqrt{\cos^2\phi\sin^2\theta'+\sin^2\phi}} \\ \frac{\cos\phi\left(\cos^2\theta'\cos 2\phi-1\right)}{\sqrt{\cos^2\phi\sin^2\theta'+\sin^2\phi}} \end{bmatrix}$
3	$\begin{bmatrix} -\cos\theta'\sin 2\phi \\ -\sin\theta' \\ -\cos\theta'\cos 2\phi \end{bmatrix}$	$\begin{bmatrix} -\sin\phi \\ 0 \\ -\cos\phi \end{bmatrix}$	$\begin{bmatrix} \frac{-\cos\phi\sin\theta'}{\sqrt{\cos^2\phi\sin^2\theta'+\sin^2\phi}} \\ \frac{\sin\phi\cos\theta'}{\sqrt{\cos^2\phi\sin^2\theta'+\sin^2\phi}} \\ \frac{\sin\phi\sin\theta'}{\sqrt{\cos^2\phi\sin^2\theta'+\sin^2\phi}} \end{bmatrix}$	$\begin{bmatrix} \frac{\sin\phi\left(\cos^2\theta'\cos 2\phi-\sin^2\theta'\right)}{\sqrt{\cos^2\phi\sin^2\theta'+\sin^2\phi}} \\ \frac{\cos\phi\sin\theta'\cos\theta'}{\sqrt{\cos^2\phi\sin^2\theta'+\sin^2\phi}} \\ \frac{\cos\phi\left(\cos^2\theta'\cos 2\phi-1\right)}{\sqrt{\cos^2\phi\sin^2\theta'+\sin^2\phi}} \end{bmatrix}$	$\begin{bmatrix} 0 \\ -\sin\theta' \\ \cos\theta' \end{bmatrix}$	$\begin{bmatrix} \frac{-\sin\phi}{\sqrt{\cos^2\phi\sin^2\theta'+\sin^2\phi}} \\ \frac{-\cos\phi\sin\theta'\cos\theta'}{\sqrt{\cos^2\phi\sin^2\theta'+\sin^2\phi}} \\ \frac{-\cos\phi\sin^2\theta'}{\sqrt{\cos^2\phi\sin^2\theta'+\sin^2\phi}} \end{bmatrix}$

Substituting $\tan\alpha = \tan\phi/\sin\theta'$ into Equation 4.21 gives the relationship between the tilt angle ϕ, incident angle θ_0 and rotation angle α as:

$$\sin\phi = \sin\theta_0 \sin\alpha. \tag{4.31}$$

If θ_0 and α are known, the tilt angle ϕ can be calculated by Equation 4.31.

The term $\mathbf{J}_{\mathrm{R}}^{(3)}(\alpha)\mathbf{J}_{\mathrm{Sample}}^{(3)}\mathbf{J}_{\mathrm{Retro}}^{(3)}\mathbf{J}_{\mathrm{Sample}}^{(3)}\mathbf{J}_{\mathrm{R}}^{(3)}(\alpha)$ in Equation 4.30 indicates the measured 3D Jones matrix by retroreflex ellipsometry. It can be transformed to the representation of Mueller calculus as

$$\mathbf{M} = \mathbf{M}_{\mathrm{R}}(\alpha)\mathbf{M}_{\mathrm{Sample}}\mathbf{M}_{\mathrm{Retro}}\mathbf{M}_{\mathrm{Sample}}\mathbf{M}_{\mathrm{R}}(\alpha). \tag{4.32}$$

The Mueller matrix of an isotropic sample $\mathbf{M}_{\mathrm{Sample}}$ can be expressed by the NSC representation:

$$\mathbf{M}_{\mathrm{Sample}} = R\begin{bmatrix} 1 & -N_{\mathrm{M}} & 0 & 0 \\ -N_{\mathrm{M}} & 1 & 0 & 0 \\ 0 & 0 & C_{\mathrm{M}} & S_{\mathrm{M}} \\ 0 & 0 & -S_{\mathrm{M}} & C_{\mathrm{M}} \end{bmatrix}, \tag{4.33}$$

where $N_{\mathrm{M}} := \cos 2\Psi$, $S_{\mathrm{M}} := \sin 2\Psi \sin\Delta$, and $C_{\mathrm{M}} := \sin 2\Psi \cos\Delta$. Ψ and Δ, which are functions of the angle of incidence and the refractive index of the sample, represent amplitude ratio and phase difference. If the sample does not depolarize the light, then $N_{\mathrm{M}}^2 + S_{\mathrm{M}}^2 + C_{\mathrm{M}}^2 = 1$ is fulfilled. The Mueller matrix of a coordinate rotation $\mathbf{M}_{\mathrm{R}}(\alpha)$ is expressed as:

$$\mathbf{M}_R(\alpha) = \begin{bmatrix} 1 & 0 & 0 & 0 \\ 0 & \cos 2\alpha & -\sin 2\alpha & 0 \\ 0 & \sin 2\alpha & \cos 2\alpha & 0 \\ 0 & 0 & 0 & 1 \end{bmatrix}, \tag{4.34}$$

When a flat sample is measured with a calibrated POI ($\alpha = 0$), the measured Mueller matrix is written as:

$$\mathbf{M}_{\mathrm{Meas},\alpha=0} = R^2 \begin{bmatrix} 1+N_\mathrm{M}^2 & -2N_\mathrm{M} & 0 & 0 \\ -2N_\mathrm{M} & 1+N_\mathrm{M}^2 & 0 & 0 \\ 0 & 0 & S_\mathrm{M}^2 - C_\mathrm{M}^2 & -2C_\mathrm{M}S_\mathrm{M} \\ 0 & 0 & 2C_\mathrm{M}S_\mathrm{M} & S_\mathrm{M}^2 - C_\mathrm{M}^2 \end{bmatrix}. \tag{4.35}$$

If the sample is tilted ($\alpha \neq 0$), then the measured Mueller matrix is written as:

$$\mathbf{M}_{\mathrm{Meas}} = R^2 \begin{bmatrix} 1+N_\mathrm{M}^2 & -2N_\mathrm{M}\cos 2\alpha & 2N_\mathrm{M}\sin 2\alpha & 0 \\ -2N_\mathrm{M}\cos 2\alpha & g_2 + g_1\cos 4\alpha & -g_1 \sin 4\alpha & 2g_3 \sin 2\alpha \\ -2N_\mathrm{M}\sin 2\alpha & g_1 \sin 4\alpha & -g_2 + g_1 \cos 4\alpha & -2g_3\cos 2\alpha \\ 0 & 2g_3 \sin 2\alpha & 2g_3 \cos 2\alpha & g_1 - g_2 \end{bmatrix}, \tag{4.36}$$

$$g_1 := 1 - C_\mathrm{M}^2,$$
$$g_2 := 1 - S_\mathrm{M}^2,$$
$$g_3 := C_\mathrm{M}S_\mathrm{M}.$$

In Equation 4.36, the measured Mueller matrix for an isotropic sample $\mathbf{M}_{\mathrm{Sample}}$ becomes anisotropic wherein the off-diagonal 2×2 blocks are nonzero elements because the plane of incidence is changed.

The normalized Mueller matrix $\hat{\mathbf{M}}_{\mathrm{Meas}}$ is shown as:

$$\hat{\mathbf{M}}_{\mathrm{Meas}} = \begin{bmatrix} 1 & \frac{-2N_\mathrm{M}\cos 2\alpha}{1+N_\mathrm{M}^2} & \frac{2N_\mathrm{M}\sin 2\alpha}{1+N_\mathrm{M}^2} & 0 \\ \frac{-2N_\mathrm{M}\cos 2\alpha}{1+N_\mathrm{M}^2} & \frac{g_2+g_1\cos 4\alpha}{1+N_\mathrm{M}^2} & \frac{-g_1\sin 4\alpha}{1+N_\mathrm{M}^2} & \frac{2g_3\sin 2\alpha}{1+N_\mathrm{M}^2} \\ \frac{-2N_\mathrm{M}\sin 2\alpha}{1+N_\mathrm{M}^2} & \frac{g_1\sin 4\alpha}{1+N_\mathrm{M}^2} & \frac{-g_2+g_1\cos 4\alpha}{1+N_\mathrm{M}^2} & \frac{-2g_3\cos 2\alpha}{1+N_\mathrm{M}^2} \\ 0 & \frac{2g_3\sin 2\alpha}{1+N_\mathrm{M}^2} & \frac{2g_3\cos 2\alpha}{1+N_\mathrm{M}^2} & \frac{g_1-g_2}{1+N_\mathrm{M}^2} \end{bmatrix}, \tag{4.37}$$

The 16 elements of the normalized Mueller matrix $\hat{\mathbf{M}}_{\text{Meas}}$ are reduced to eight different elements owing to the symmetry of the matrix. Further, the off-diagonal elements of the matrix can be used for the alignment of the sample and the determination of the plane of incidence. The rotation angle and NSC parameters can be solved analytically as following:

$$
\begin{aligned}
2\alpha &= -\tan^{-1}\left(\frac{m_{13}}{m_{12}}\right) = \tan^{-1}\left(\frac{m_{31}}{m_{21}}\right) = -\tan^{-1}\left(\frac{m_{24}}{m_{34}}\right) = \tan^{-1}\left(\frac{m_{42}}{m_{43}}\right), \\
\frac{N_{\text{M}}^2}{(1+N_{\text{M}}^2)^2} &= \frac{m_{12}^2+m_{13}^2}{4} = \frac{m_{21}^2+m_{31}^2}{4}, \\
\frac{S_{\text{M}}^2}{(1+N_{\text{M}}^2)^2} &= \frac{1}{2}\left(\sqrt{m_{42}^2+m_{43}^2+m_{44}^2}+m_{44}\right) \\
&= \frac{1}{2}\left(\sqrt{m_{24}^2+m_{34}^2+m_{44}^2}+m_{44}\right), \\
\frac{C_{\text{M}}^2}{(1+N_{\text{M}}^2)^2} &= \frac{1}{2}\left(\sqrt{m_{42}^2+m_{43}^2+m_{44}^2}-m_{44}\right) \\
&= \frac{1}{2}\left(\sqrt{m_{24}^2+m_{34}^2+m_{44}^2}-m_{44}\right).
\end{aligned}
\tag{4.38}
$$

In Equation 4.37, elements m_{32} and m_{43} have a high sensitivity to the change of the tilt and incident angles, respectively [Joh11]. Figure 4.10 shows the simulation result of a gold plane mirror that rotates around the y axis (see Figure 4.10) in a range of ϕ from $-22.5°$ to $22.5°$ at an angle of incidence of 70°; whereupon m_{32} changes from -0.85 to 0.85 while m_{43} only has a difference of 0.1 during the rotation. Figure 4.11 shows the simulation data of a gold plane mirror whose angle of incidence is altered from 45° to 90° at a tilt angle of 5°; whereupon m_{32} only has a difference of 0.35 while m_{43} varies from -0.98 to 0.98. These results show the feasibility to determine the incident and tilt angles from the measured Mueller matrix.

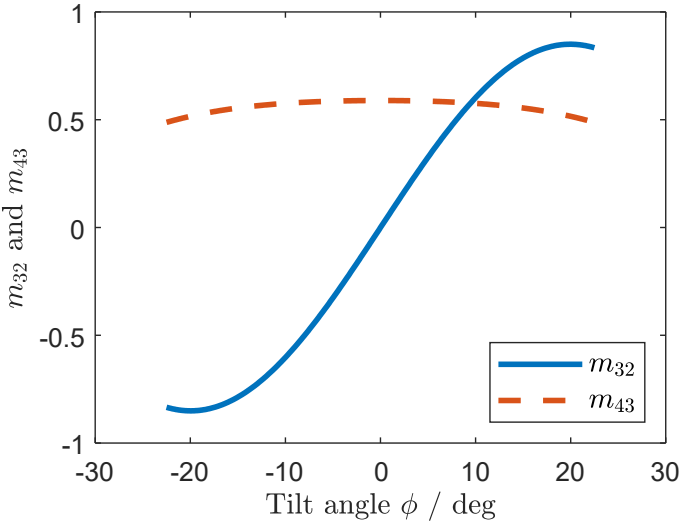

Figure 4.10: Simulation result of a gold plane mirror rotated around the y axis in a range of ϕ from $-22.5°$ to $22.5°$ at an angle of incidence of $70°$. The refractive index of the gold mirror is $0.184 - 3.431\mathrm{i}$.

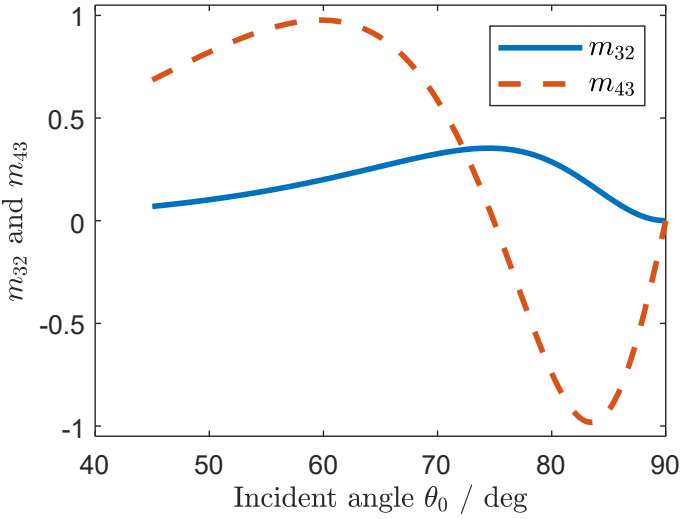

Figure 4.11: Simulation result of a gold plane mirror at angles of incidence ranging from $45°$ to $90°$ at a tilt angle ϕ of $5°$. The refractive index of the gold mirror is $0.184 - 3.431\mathrm{i}$.

4.4 Prototype, system calibration and data analysis

The prototype of the retroreflex ellipsometer is shown in Figure 4.12. It features a laser light source with a wavelength of 635 nm. The collimated laser beam passes through a linear polarizer, a quarter-waveplate and a non-polarizing beamsplitter (NPBS) and the returning beam is reflected by the NPBS and is received by a polarimeter (PAX1000, Thorlabs Inc.). The ellipsometry data is analyzed using a dual rotating-compensator Mueller matrix ellipsometry which is described in Section 3.6, so all Mueller matrix elements can be obtained.

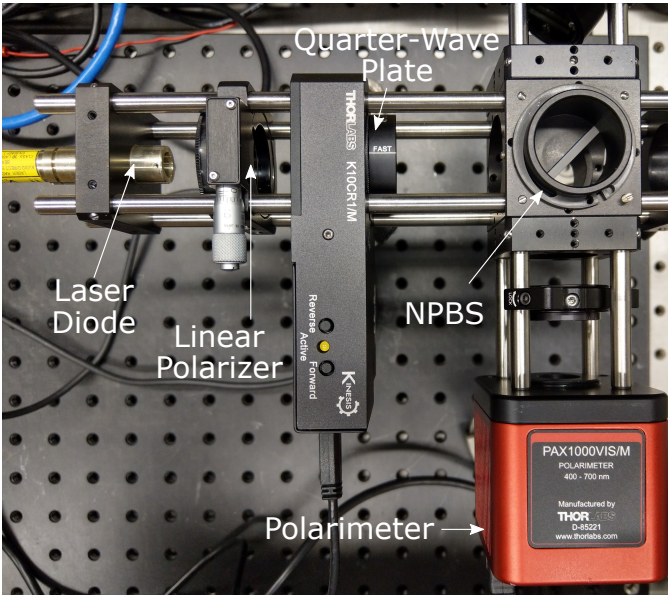

Figure 4.12: Photograph of the retroreflex ellipsometer prototype.

To ensure accurate results, every component in the prototype must be either calibrated or measured, especially the NPBS. The NPBS has strong polarization distortions, that should be taken into account [Joh11, Liu16, Zha18]. Figure

4.13 shows the calibration procedure for this study, which is similar to that of Liu et al. [Liu16]. Laser beams from the PSG are transmitted through the NPBS and are measured using a calibrated polarimeter, where the measured Stokes vectors are denoted as $\mathbf{S}_{\text{PSG}}$. A mirror then reflects the laser beam to the NPBS and the polarimeter measures the beams that are reflected from the NPBS, which is denoted as $\mathbf{S}'$. The Mueller matrix model of the calibration process is expressed as:

$$\mathbf{S}' = \mathbf{M}_{\text{NPBS,R}} \cdot \mathbf{M}_{\text{Mirror}} \cdot \mathbf{S}_{\text{PSG}}, \tag{4.39}$$

where $\mathbf{M}_{\text{NPBS,R}}$ indicates the Mueller matrix for the reflection of the NPBS. $\mathbf{M}_{\text{NPBS,R}}$ is calculated by matrix multiplication. During the assembly and the calibration procedures, it is important that all of the polarized components are aligned carefully with the axis of the polarimeter to reduce alignment errors in the system.

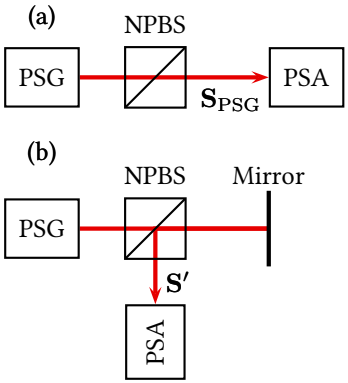

Figure 4.13: Calibration procedure for the NPBS and the corresponding setup.

After calibration, the ellipsometer is able to measure samples. To obtain the ellipsometric parameters (Ψ, Δ) and the tilt angle α from the Mueller matrix $\mathbf{M}$ in Equation 4.32, a numerical fitting method is used to find those parameters.

The squared error function χ^2 is defined as:

$$\chi^2 = \sum_{i,j=1}^{4} (m_{ij}^{\text{Exp}} - m_{ij}^{\text{Calc}})^2, \tag{4.40}$$

where m_{ij}^{Exp} and m_{ij}^{Calc} denote the experimental and calculated matrix element quantities, respectively.

4.5 Summary

Retroreflex ellipsometry overcomes the geometric limitations of standard ellipsometers by using a cat's eye retroreflector. The polarization properties of the retroreflector are analyzed using the small-angle approximation, numerical simulation and experimental validation. These results are in good agreement and verify the polarization-preserving properties at an incident angle of less than $\pm 30°$. Therefore, retroreflex ellipsometry can measure nonplanar surfaces without the need for time-consuming adjustment because the conditions for alignment between the PSA and the sample with nonplanar surfaces is automatically fulfilled by the retroreflector.

However, the PSA can receive signals when the normalized incident height h/r is less than 0.2. The light from the range of $h/r \in [0.2, 1]$ is blocked by the polarimeter's aperture. Therefore, only 4% of the light can be detected. In consequence, retroreflex ellipsometry requires longer integration time for the PSA or high-power light sources, such as lasers and Xenon light. In addition, using a high reflective coating on the reflection side of the retroreflector can increase the reflection efficiency.

The polarization model for nonplanar surfaces is derived by polarization ray tracing. The relationship between the angle of incidence θ_0, azimuthal rotation angle α and tilt angle ϕ is determined. The azimuthal rotation angle α can be obtained by the measured Mueller matrix for the sample. If the AOI is known, the tilt angle can be calculated.

A prototype based on the principle of retroreflex ellipsometry is built. The dual rotating-compensator configuration can measure the full Mueller matrix for the sample. A calibration method for the NPBS is proposed to compensate for the polarization distortion induced by the NPBS. A numerical fitting method is applied to obtain the ellipsometric parameters (Ψ, Δ) and the azimuthal rotation angle α from the measured Mueller matrix $\hat{\mathbf{M}}_{\mathrm{Meas}}$,

5 Measurement methods and uncertainty analysis for nonplanar surfaces

Retroreflex ellipsometry addresses the geometric limitations of standard ellipsometers. However, the geometric data for the portion of the sample that is within the measurement field is still necessary for accurate measurements of the refractive index or film thickness. This chapter presents two methods for two-phase and three-phase systems. Section 5.1 uses ellipsometric parameters and reflectance data to calculate the angle of incidence and the optical properties of isotropic substrates. Section 5.2 uses a numerical inverse method to calculate the angle of incidence and film thickness using ellipsometric parameters and the optical properties of the sample. A Monte Carlo simulation is used to quantify and propagate uncertainties for these methods. The effect of curved surfaces on ellipsometric measurements is determined in Section 5.3 using numerical simulation.

5.1 Analytical determination of the angle of incident and the refractive index for a two-phase system

Ellipsometry is sensitive to the angle of incidence. A slight error in determining the AOI can cause significant errors in the refractive index calculation. For a nonplanar surface, the angle of incidence changes because the surface is curved. The height and inclination of the sample are adjusted to allow the ellipsometer to measure the sample in a calibrated plane of incidence.

This alignment process is very time-consuming and the range of adjustment is limited so only some positions on the sample can be measured [Har20]. Spectroscopic ellipsometry can use a dispersion model [Fuj07], measurements at different angles [Woo99] and reflectance measurements [Del02] to determine the AOI and the refractive index. The first two methods are not suitable for in situ or inline measurements because they require a long measurement time. The reflectance can also be measured using the ellipsometric parameters if the intensity is calibrated using a known standard so ellipsometry and reflectance measurements can be used for in situ or inline measurements. However, the major disadvantage of reflectance measurements is that they are significantly affected by the stability of the illumination and the photodetector so it is difficult to calibrate an absolute intensity [Stu00].

Many studies use ellipsometric parameters and reflectance data to measure dielectric functions and thin films [Haz83, An93, Stu00, Liz13, Löp15, Liu19]. However, these assume that the samples are flat and that the angle of incidence is fixed and known. These assumptions are not valid for nonplanar surfaces and experimental errors arise if the sample is offset or tilted. In 2010, Ghosh et al. measured the reflectance for p- and s-polarized waves (R_p, R_s) to determine the refractive index of spherical balls for rendering with an LED sphere with about 150 individually controllable lights (circularly polarized) [Gho10]. The study achieved a relative error of 1.5% for the refractive index of a rubber ball. Only dielectric materials were used and additional photometric measurements were required to obtain the surface geometry but the solution represents an advance for ellipsometric measurements. To allow ellipsometric measurements for nonplanar surfaces, this study combines retroreflex ellipsometry and reflectance data to measure the optical properties of an isotropic two-phase system with nonplanar surfaces using the reflectance R and ellipsometric data (Ψ, Δ) with no prior knowledge of the angle of incidence. A two-phases system includes an ambient and a substrate. The following describes two methods to determine the AOI and the refractive index for transparent and non-transparent substrates.

5.1.1 Transparent substrates

Figure 5.1 shows the refraction and reflection of a ray of light that impinge from an ambient material with a refractive index of N_0 on a substrate with a refractive index of N_1. The roughness and the backside reflection of the substrate are not considered by this study.

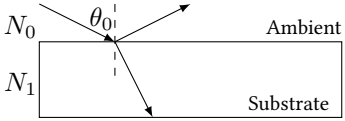

Figure 5.1: Optical model of a two phase system (ambient(0)/ substrate(1)).

If the substrate is transparent, its extinction coefficient (k) is 0, so $N_1 = n \in \mathbb{R}_{>0}$. According to Fresnel's equations in Equation 3.11, the amplitude reflection coefficient for p- and s- polarization is also a real number (r_p, $r_s \in \mathbb{R}$). Figure 5.2 shows the amplitude coefficient at an air/glass interface, which shows that r_s is negative, r_p is positive when Δ is 180°, and r_p is negative when Δ is 0°. By substituting $\tan\Psi = |r_p| / |r_s|$ and the sign condition for r_p into Equation 3.16, r_p and r_s are expressed as:

$$r_p = \begin{cases} \sqrt{2R}\sin\Psi, \text{if } \Delta = 180° \\ -\sqrt{2R}\sin\Psi, \text{if } \Delta = 0 \end{cases}, \tag{5.1}$$

$$r_s = -\sqrt{2R}\cos\Psi. \tag{5.2}$$

The direct relationship between the p- and s-polarization and the angle of incidence is shown as [Azz86]:

$$\cos 2\theta_0 = \frac{r_s^2 - r_p}{r_s - r_s r_p}. \tag{5.3}$$

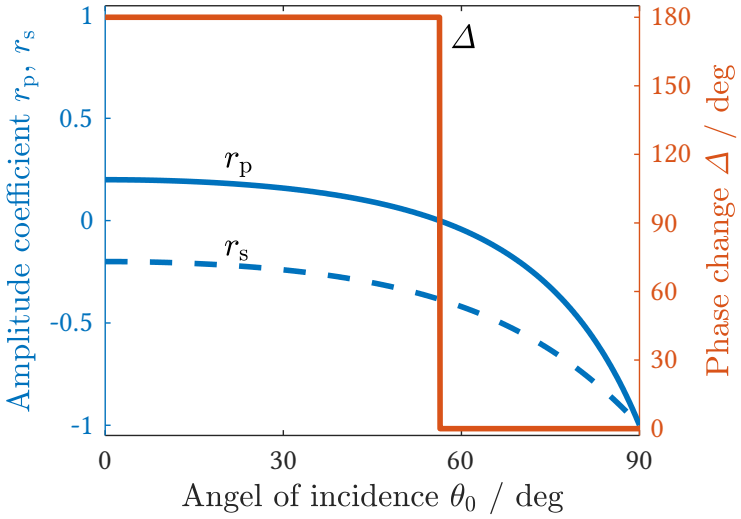

Figure 5.2: Amplitude coefficient r_p and r_s, and the phase change Δ at an air ($N_0 = 1$)/ glass ($N_1 = 1.5$) interface.

By combining Equations 5.1 and 5.2 with Equation 5.3, $\cos 2\theta_0$ is rewritten as:

$$\cos 2\theta_0 = \begin{cases} \frac{-2\sqrt{R}\cos\Psi + \sqrt{2}\tan\Psi}{\sqrt{2} - 2\sqrt{R}\sin\Psi}, \text{if } \Delta = 180° \\ \frac{-2\sqrt{R}\cos\Psi - \sqrt{2}\tan\Psi}{\sqrt{2} + 2\sqrt{R}\sin\Psi}, \text{if } \Delta = 0° \end{cases}. \tag{5.4}$$

The angle of incidence is calculated using Equation 5.4 and the refractive index is calculated using Equation 5.5 [Azz87].

$$N_1 = N_0 \tan\theta_0 \sqrt{1 - \frac{4\rho}{(1+\rho)^2}\sin^2\theta_0}. \tag{5.5}$$

By using trigonometric formulas, $\tan\theta_0$ and $\sin\theta_0$ are expressed as

$$\tan\theta_0 = \sqrt{\frac{1 - \cos 2\theta_0}{1 + \cos 2\theta_0}}, \tag{5.6}$$

$$\sin^2\theta_0 = \frac{1}{2}(1-\cos 2\theta_0). \tag{5.7}$$

Substituting Equations 5.4, 5.6 and 5.7 into Equation 5.5 gives the refractive index of the transparent substrate as:

$$N_1 = \begin{cases} N_0\sqrt{\frac{(\sqrt{2R}\sin\Psi+1)(\sqrt{2R}\cos\Psi+1)}{(\sqrt{2R}\sin\Psi-1)(\sqrt{2R}\cos\Psi-1)}}, \text{if } \Delta = 180^\circ \\ N_0\sqrt{\frac{(\sqrt{2R}\sin\Psi-1)(\sqrt{2R}\cos\Psi+1)}{(\sqrt{2R}\sin\Psi+1)(\sqrt{2R}\cos\Psi-1)}}, \text{if } \Delta = 0^\circ \end{cases}. \tag{5.8}$$

If the angle of incidence is equal to the Brewster angle, then $\Psi = 0$, $r_p = 0$ and $r_s = -\sqrt{2R}$. Substituting these values into Equations 5.4 and 5.8, the angle of incidence and the refractive index are calculated as:

$$\cos 2\theta_0 = -\sqrt{2R}, \tag{5.9}$$

$$N_1 = N_0\sqrt{\frac{1+\sqrt{2R}}{1-\sqrt{2R}}}. \tag{5.10}$$

The reflectometric and ellipsometric measurements of Hazebroek and Visser [Haz83] are used to verify the proposed method. The study by Hazebroek and Visser used a laser interferometric ellipsometer to measure the ellipsometric parameters and the reflectance of a silica disc (Heraues Ultrasil). Table 5.1 shows the experimental data and the calculated data for two angles of incidence using the nominal refractive index.

The data in Table 5.1 is used to validate the proposed method. The phase difference Δ for the experimental measurements is zero. Table 5.2 shows the experimental results and two theoretical values using the proposed method. The calculation results are almost the same as the theoretical values. Only one result shows a difference of 0.0001 in the refractive index and this may

Table 5.1: Experimental data and calculated parameters for silica with a refractive index of 1.4593 at a wavelength of 568.1 nm. The table is reproduced from [Haz83], where $R_{\parallel} = R_p$, $R_{\perp} = R_s$ and $R = \frac{1}{2}(R_{\parallel} + R_{\perp})$. The columns for Theory 1 and Theory 2 show the simulation data based on the nominal refractive index of the sample.

	Exp. 1	Theory 1	Exp. 2	Theory 2
AOI θ_0	69.78°	-	74.77°	-
Ψ	21.31°	21.32°	27.84°	27.83°
Δ	−0.03°	0.	0.05°	0.
$R_{\parallel}$	0.0397	0.0420	0.1010	0.1047
$R_{\perp}$	0.2737	0.2783	0.3683	0.3757
R	0.1567	0.1604	0.2347	0.2402
n	1.4595	1.4593	1.4590	1.4593
k	0.0004	0.	0.0011	0.

be due to a rounding error or the resolution of the experiment data. For the calculation, the maximum difference in the angle of incidence is 0.16° and in the refractive index is 0.0103. These results show satisfactory agreement and prove the utility of the derived equations. The most probable source of error in the set of measurements is the reflectance, which is smaller than the theoretical value. This is probably due to the effect of surface roughness, which can create a small amount of non-specularly scattered light. The experimental result for the phase difference Δ is not zero, in contrast to the nominal value. This is probably because stress-induced birefringence or internal strain is induced during the manufacturing process, which causes a phase change in the sample (see [Haz83] for more details).

Table 5.2: Calculation results for Table 5.1 using the proposed method.

Evaluation	AOI θ_0	Refractive index n	$\Delta\theta_0$	Δn
Exp. 1	69.62°	1.4508	−0.16°	−0.0087
Theory 1	69.78°	1.4592	0°	0.0001
Exp. 2	74.61°	1.4487	−0.16°	−0.0103
Theory 2	74.77°	1.4593	0°	0

5.1.2 Non-transparent substrates

Non-transparent materials include semi-transparent, metallic and opaque materials. The extinction coefficient (k) of these materials is non-zero, i.e, $N_1 \in$

$\mathbb{C}$, so the refractive index of a non-transparent substrate is defined as:

$$N_1 = n - ik. \tag{5.11}$$

Fresnel's equations describe reflectance R and ellipsometric parameters (Ψ,Δ) in terms of the complex refractive index N_1 and the angle of incidence θ_0. There are three unknown parameters and three equations for R, Ψ and Δ. It is possible to solve the equations for n, k and θ_0 analytically.

The Fresnel equations for the reflection r_p, r_s in phase notation is described in Equation 3.13. Substituting $\tan\Psi = |r_p| / |r_s|$ and Equation 3.14 into Equation 3.16, $|r_p|$ and $|r_s|$ gives:

$$\begin{aligned} |r_p| &= \sqrt{2R}\sin\Psi \\ |r_s| &= \sqrt{2R}\cos\Psi \end{aligned} \tag{5.12}$$

Substituting Equation 3.13 into Equation 5.3 gives $\cos 2\theta_0$ as:

$$\cos 2\theta_0 = \frac{e^{i\delta_{rs}} |r_s|^2 - e^{i(\delta_{rp}-\delta_{rs})} |r_p|}{|r_s| - e^{i\delta_{rp}} |r_p| |r_s|}. \tag{5.13}$$

The angle of incidence θ_0 is a real number so $\cos 2\theta_0$ is also a real number and the imaginary part of $\cos 2\theta_i$ is 0. The imaginary part of Equation 5.13 is written as:

$$\Im(\cos 2\theta_0) = \frac{|r_p| (|r_s|^2 - 1) \sin(\delta_{rp} - \delta_{rs}) + (|r_s|^2 - |r_p|^2) \sin\delta_{rs}}{|r_s| (|r_p|^2 - 2|r_p| \cos\delta_{rp} + 1)} = 0. \tag{5.14}$$

Then, $\sin\delta_{rs}$ is solved as:

$$\sin\delta_s = \frac{|r_p| (|r_s|^2 - 1) \sin(\delta_{rp} - \delta_{rs})}{|r_p|^2 - |r_s|^2}. \tag{5.15}$$

Substituting Equation 5.12 and $\delta_{rp} - \delta_{rs} = \Delta$ into Equation 5.15 gives $\sin\delta_{rs}$ in the form of R, Ψ and Δ as:

$$\sin\delta_{rs} = \frac{\sin\Delta\sin\Psi(1 - R - R\cos 2\Psi)}{\sqrt{2R}\cos 2\Psi}. \tag{5.16}$$

The angle of incidence is calculated using the real part of Equation 5.13:

$$\Re(\cos 2\theta_0) = \frac{(|r_s|^2 + |r_p|^2)\cos\delta_{rs} - |r_p|(1 + |r_s|^2)\cos\Delta}{|r_s|(|r_p|^2 - 2|r_p|\cos\delta_{rp} + 1)}. \tag{5.17}$$

Substituting Equation 5.12 and $\delta_{rp} = \Delta + \delta_{rs}$ into Equation 5.13, gives $\cos 2\theta_0$ in terms of R, Ψ, Δ and δ_{rs} as:

$$\cos 2\theta_0 = \frac{2R\cos\delta_{rs} - \sqrt{R - R\cos 2\Psi}(1 + R + R\cos 2\Psi)\cos\Delta}{(\sqrt{R + R\cos 2\Psi})[1 + R - R\cos 2\Psi - 2\sqrt{R - R\cos 2\Psi}\cos(\Delta + \delta_{rs})]}. \tag{5.18}$$

The angle of incidence is then calculated using Equation 5.18 and the complex refractive index is calculated using Equation 5.5.

The interval of δ_{rs} is from 0° to 360° so there are two solutions for δ_{rs} in Equation 5.16. Only one solution is in agreement with the experimental result. The refractive index of a gold mirror is $0.1838 - 3.4313i$ at a wavelength of 632.8 nm. The respective simulated parameters of Ψ,Δ and R for the mirror at an angle of incidence of 70° are 43.65°, 108.15° and 0.937, respectively. The calculation results are listed in Table 5.3. Solution 1 is wrong because the calculated angle of incidence has an error of 55° and the refractive index shows that the gold mirror is a transparent material ($k \approx 0$). Only Solution 2 is in agreement with the simulation parameters and the differences are due to rounding errors.

Table 5.3: Results for the simulation data for a gold mirror ($N = 0.1838 - 3.4313\mathrm{i}$) at an angle of incidence of 70°. The respective values for the simulated parameters Ψ, Δ and R are $43.65°, 108.15°$ and 0.937, respectively. Solutions 1 and 2 show the calculated parameters using Equations 5.16, 5.18 and 5.5.

	Sol. 1 ($\delta_{rs} < 90°$)	Sol. 2 ($\delta_{rs} > 90°$)
Phase of r_s (δ_{rs})	10.98°	169.02°
Phase of r_p (δ_{rp})	119.13°	277.16°
Angle of incidence θ_0	14.80°	69.98°
Refractive index N_1	$0.2379 - 0.0018\mathrm{i}$	$0.1834 - 3.4262\mathrm{i}$

Mathematically, δ_{rs} is a monotonically increasing function of the angle of incidence so the minimum value for δ_{rs} occurs at normal incidence and the maximum value occurs at grazing incidence ($\delta_{rs} = 180°$). The amplitude reflection coefficient for s-polarization is given by:

$$r_s(\theta_0) = \frac{N_0 \cos\theta_0 - \sqrt{N_1^2 - N_0^2 \sin^2\theta_0}}{N_0 \cos\theta_0 + \sqrt{N_1^2 - N_0^2 \sin^2\theta_0}}. \tag{5.19}$$

For $\theta_0 = 0$, $N_0 = 1$ (air) and $N_1 = n - \mathrm{i}k$,

$$r_s(0) = \frac{1 - (n^2 + k^2)}{(n+1)^2 + k^2} + \mathrm{i}\frac{2k}{(n+1)^2 + k^2}. \tag{5.20}$$

Since n and k are positive real numbers for absorbing substrates, $r_s(0)$ is in quadrant II in the complex plane if $(n^2 + k^2)$ is greater than 1. In the infrared and visible regions, either or both n or k of N_1 is greater than 1 so δ_{rs} is between 90° to 180°. This constraint is then used to calculate the AOI θ_0 and the complex refractive index. Solution 1 ($\delta_{rs} < 90°$) in Table 5.3 only exists if $(n^2 + k^2)$ is less than 1, which is at extreme ultraviolet or X-ray wavelengths.

The reflectometric and the ellipsometric measurements of Hazebroek and Visser [Haz83] are used to verify the proposed method. Table 5.5 shows the experimental data.

This data is used to verify the proposed method for non-transparent substrates. Table 5.5 shows experimental results for the lubrication oil and cast

Table 5.4: Experimental data and calculated parameters for lubrication oil and a cast iron part at a wavelength of 568.1 nm. The table is reproduced from [Haz83], where $R_\parallel = R_p$, $R_\perp = R_s$ and $R = \frac{1}{2}(R_\parallel + R_\perp)$.

	Lubrication oil	Cast iron
θ_0	75.00°	69.78°
Ψ	27.53°	29.03°
Δ	0.47°	122.24°
$R_\parallel$	0.1073	0.2529
$R_\perp$	0.3943	0.8197
R	0.2508	0.5363
n	1.4899	2.5269
k	0.0101	3.2563

iron using the proposed method and the results are compared with the original data. The calculation results are almost the same as the experimental values. For the lubrication oil, the respective difference in the AOI and n is 0.01° and 0.0007. For the cast iron, the respective difference in the AOI θ_0, 0.07°, 0.0106 and 0.0150, respectively. The most probable source of error in the set of measurements is the reflectance, which is smaller than the simulated value using ellipsometry. Surface roughness may account for this difference because the cast iron was polished with diamond paste but there is still a small amount of non-specularly scattered light. The proposed method assumes perfect specular reflection. Any difference in reflectance induces an uncertainty in the AOI and the complex refractive index. However, these results are in very good agreement so the derived equations are correct and the method is feasible for real applications.

Table 5.5: Calculation results for Table 5.4 using the proposed method.

	Lubrication oil	Cast iron
AOI θ_0	75.00°	69.71°
N_1	$1.4892 - 0.001\mathrm{i}$	$2.5163 - 3.2413\mathrm{i}$
$\Delta\theta_0$	−0.01°	−0.07°
Δn	−0.0007	−0.0106
Δk	0.	−0.0150

5.1.3 Uncertainty analysis

The proposed method determines the refractive index of the substrate using the angle of incidence and ellipsometric parameters. Hence, the accuracy of the angle of incidence has a significant effect on the refractive index. For reflectance measurements, the light source can be unpolarized or polarized. Mueller matrix ellipsometry uses a polarized light source and the first element of the Mueller matrix represents the reflectance of the sample. If an ellipsometer is calibrated properly, most systematic errors can be eliminated, such as component imperfections and azimuth errors. However, random errors due to noise from the detector and the light source are unavoidable. There is uncertainty in the angle of incidence θ_0 because there are experimental errors in the ellipsometric data and the reflectance measurement.

A Monte Carlo error analysis, which is a widely used tool to estimate uncertainty through a model by substituting a range of values, is used to determine the uncertainty in the angle of incidence. The probability density functions (PDF) for the Monte Carlo analysis are Gaussian distributions. The number of Monte Carlo trials is 10^6. The typical measurement uncertainty in ellipsometric data in spectroscopic ellipsometry is $(u(\Psi), u(\Delta)) = (0.01°, 0.02°)$, where u denotes the standard uncertainty in form of a standard deviation. For specular surfaces, the uncertainty in reflectance is 0.0001 in [Haz83], 0.002 [Lam06] and 0.003 [Hei15]. In order to demonstrate the effect of reflectance, four different parameters for reflectance $(u(R) = 0, 0.001, 0.003, 0.005)$ are used to account for uncertainty in the laboratory instruments. $u(R) = 0$ is used to show the effect of $u(\Psi)$ and $u(\Delta)$. The uncertainty in the angle of incidence is represented by the root-mean-squared error (RMSE).

$$\text{RMSE} = \sqrt{\sum_{i=1}^{T} (\frac{y_i - \hat{y}}{T})^2}, \tag{5.21}$$

where y_i, $\hat{y}_i$ and T are the ith observed values, the ith prediction value and T measurement times. The normalized root-mean-squared error (NRMSE) is

used to calculate the performance for the proposed models.

$$\mathrm{NRMSE} = \frac{\mathrm{RMSE}}{\hat{y}}. \tag{5.22}$$

5.1.3.1 Transparent substrates

Figure 5.3 shows the RMSE value for the angle of incidence θ_0 for the simulated measurements using a N-BK7 window for which the refractive index is $N_1 = 1.5151$ at a wavelength of 632.8 nm. The curve (a) shows the uncertainty in the AOI, which is induced only by the ellipsometric parameters and the RMSE for an angle of incidence that is less than 0.01° between 40° and 80°. If the uncertainty in the reflectance is 0.001 (curve (b)), the RMSE for the AOI is less than 0.09°. The curve (c) ($u(R) = 0.003$) shows that the RMSE for the AOI is less than 0.28°. In curve (d) ($u(R) = 0.005$), the RMSE for the AOI is less than 0.47°. The uncertainty decreases as the angle of incidence increases for curves (b), (c) and (d).

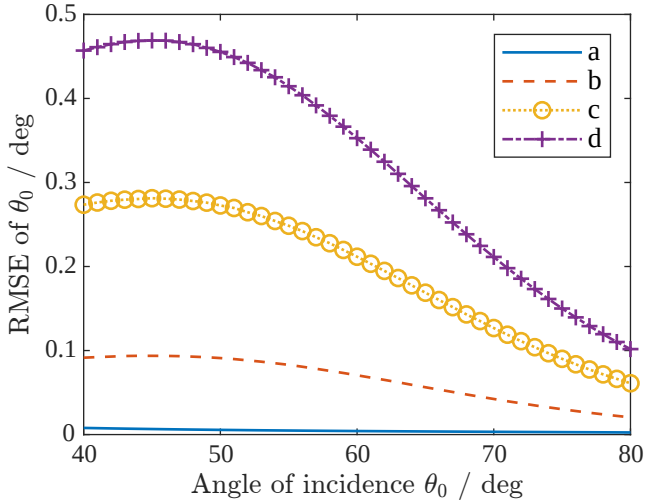

Figure 5.3: The RMSE for an angle of incidence between 40° and 80° for the N-BK7 window ($N_1 = n = 1.5151$). The uncertainty in the ellipsometric parameters ($u(\Psi)$,$u(\Delta)$) is (0.01°, 0.02°) and the uncertainty in the reflectance are (a) $u(R) = 0$, (b) $u(R) = 0.001$, (c) $u(R) = 0.003$ and (d) $u(R) = 0.005$.

An appropriate angle of incidence (large θ_0) reduces the uncertainty. For transparent substrates, a large angle of incidence decreases the RMSE for the AOI.

Figure 5.4 shows the RMSE for the refractive index (n) corresponding to Figure 5.3. Curves (a) and (b) exhibit smaller differences (NRMSE(n) $< 0.5\%$) than the nominal value between angles of incidence of 40° and 80°. In curves (c) and (d), n is better than 0.034 (2.3%) for an angle of incidence θ_0 of 40° and 80°. The simulation results show good agreement with the experiment results of Ghosh et al. [Gho10]. The uncertainty is satisfactory (NRMSE(n) $\leq 2.3\%$) for the refractive index.

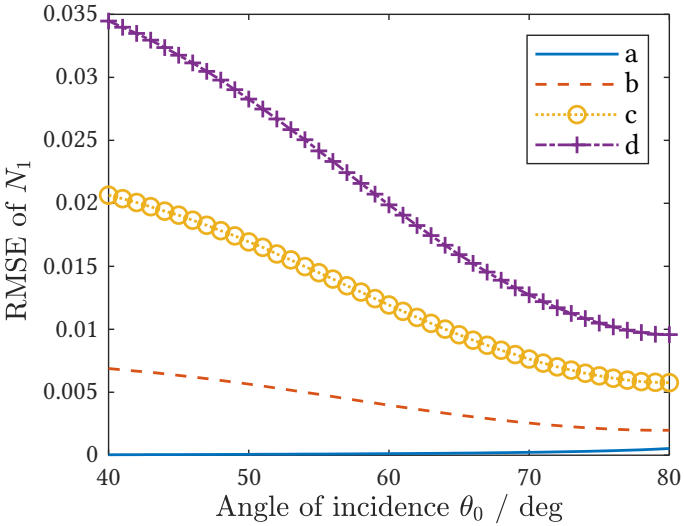

Figure 5.4: The RMSE for n between an incident angle of 40° and 80° for the N-BK7 window ($N_1 = n = 1.5151$). The uncertainty in the ellipsometric parameters ($u(\Psi)$,$u(\Delta)$) is (0.01°, 0.02°) and the uncertainty in the reflectance is (a) $u(R) = 0$, (b) $u(R) = 0.001$, (c) $u(R) = 0.003$ and (d) $u(R) = 0.005$.

To use the proposed method for different transparent materials, a simulated refractive index ($1.5 \leq n \leq 2$) is used to calculate the RMSE for n at an angle of incidence of 60°, which is a commonly used angle for ellipsometry. The calculation method is the same as that for Section 5.1.3. The uncertainty in

the ellipsometric parameters ($u(\Psi)$,$u(\Delta)$) is (0.01°, 0.02°) and the uncertainty in the reflectance is $u(R) = 0.003$. Figure 5.5 shows the result for the RMSE for the refractive index. The RMSE for n increases as n increases but the NRMSE for n is constant (0.9%) as n increases. The simulated results show that the proposed method is feasible for different transparent materials.

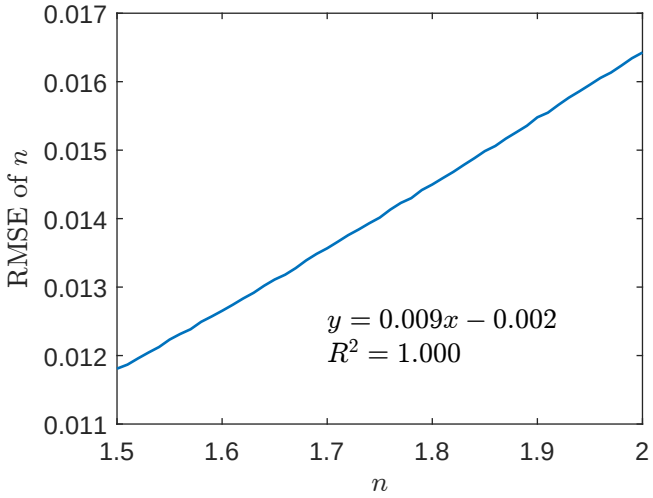

Figure 5.5: The RMSE of the refractive indices for different transparent materials ($1.5 \leq n \leq 2$) at an incident angle of 60°. The uncertainty of ellipsometric parameters ($u(\Psi)$,$u(\Delta)$) is (0.01°, 0.02°) and the uncertainty of reflectance is $u(R) = 0.003$.

5.1.3.2 Non-transparent substrates

Figure 5.6 shows the RMSE for the angle of incidence θ_0 for the simulated measurements for an aluminum mirror for which the refractive index is $N_1 = 1.4482 - 7.5367i$ at a wavelength of 632.8 nm. Curve (a) shows the uncertainty in the AOI θ_0 due only to the ellipsometric parameters and the RMSE for the AOI θ_0 is less than 0.26° between angles of incidence θ_0 of 40° and 80°. If the uncertainty in the reflectance is 0.001 (curve (b)), the RMSE for the AOI θ_0 is less than 0.37°. Curve (c) ($u(R) = 0.003$) shows that the RMSE for the

AOI θ_0 is less than 1.09°. For curve (d) ($u(R) = 0.005$), the RMSE for the AOI θ_0 is less than 1.94°.

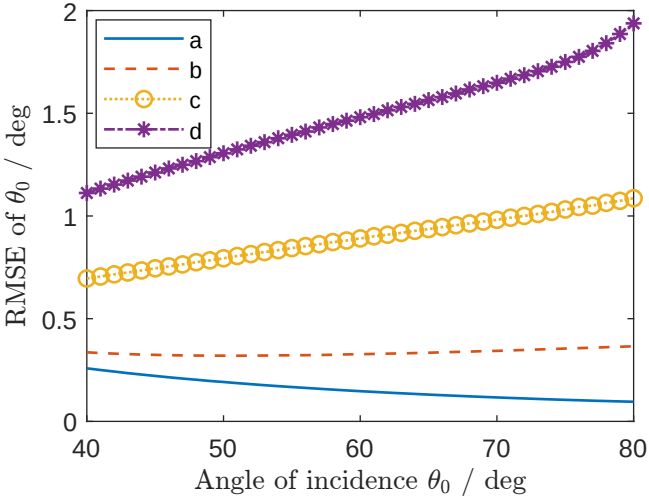

Figure 5.6: The RMSE for an angles of incidence between 40° and 80° for an aluminum mirror ($N_1 = 1.4482 - 7.5367$i). The uncertainty in the ellipsometric parameters ($u(\Psi)$,$u(\Delta)$) is (0.01°, 0.02°) and the uncertainty in the reflectance R is (a) $u(R) = 0$, (b) $u(R) = 0.001$, (c) $u(R) = 0.003$ and (d) $u(R) = 0.005$.

The uncertainty arises as the AOI θ_0 increases for curves (b), (c) and (d). In contrast to transparent substrates, a small AOI θ_0 decreases the uncertainty if the uncertainty in the reflectance is considered. For the same conditions, the RMSE for θ_0 for non-transparent substrates is greater than the RMSE for θ_0 for transparent substrates. Hence, it can be expected that the uncertainty in the refractive index for non-transparent substrates is also greater than that for transparent substrates.

Figures 5.7 and 5.8 show the RMSE for a complex refractive index ($N_1 = n - ik$). Curves (a) and (b) show small differences (NRMSE(n) < 3.9% and NRMSE(k) < 4.0%) between angles of incidence of 40° and 80°. For curve (c), the RMSE for n is less than 0.10 (7.0%) and the RMSE for k is less than 0.54 (7.1%) for an angle of incidence of less than 73°. For curve (d), n is less than 0.15 (10.0%) and k is less than 0.78 (10.0%) is the angle of incidence is less than

69°. If the AOI is appropriate ($\theta_0 < 69°$), the uncertainty in the refractive index is acceptable (NRMSE(n,k) < 10%), even for the worst case (curve (d)). The accuracy of the measured complex refractive index is sufficient for material identification in terms of a distinction between Al ($N = 1.4482 - 7.5367\mathrm{i}$) and Ag ($N = 0.0562 - 4.2760\mathrm{i}$) at a wavelength of 632.8 nm.

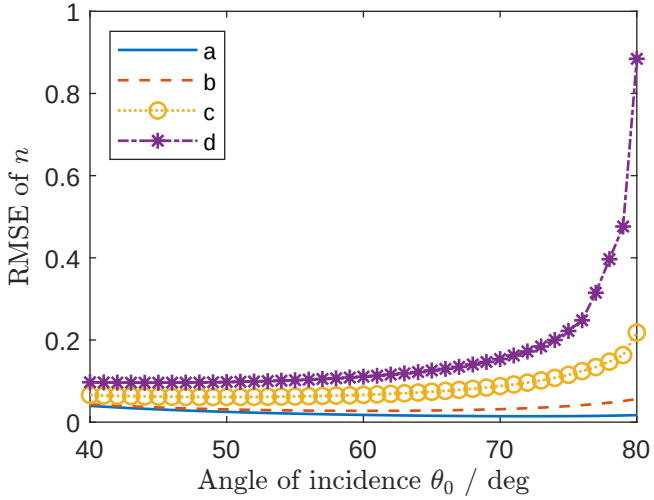

Figure 5.7: The RMSE for n between angles of incidence of 40° and 80° for an aluminum mirror ($N = 1.4482 - 7.5367\mathrm{i}$). The uncertainty in the ellipsometric parameters ($u(\Psi)$,$u(\Delta)$) is (0.01°, 0.02°) and the uncertainty in the reflectance R are (a) $u(R) = 0$, (b) $u(R) = 0.001$, (c) $u(R) = 0.003$ and (d) $u(R) = 0.005$.

To determine how the proposed method can be used for different materials, simulated complex refractive indices ($0 < n < 10$, $0 < k < 10$) are used to calculate the RMSE for n and k at an angle of incidence of 60°. The uncertainty in the ellipsometric parameters ($u(\Psi)$,$u(\Delta)$) is (0.01°, 0.02°) and the uncertainty in the reflectance is $u(R) = 0.003$.

Figure 5.9 shows the calculation result for the RMSE. The nominal values for N_1 are shown as dots and the width and the height of the rectangles represent the RMSEs for n and k, respectively. If n is fixed, the RMSE for n and k

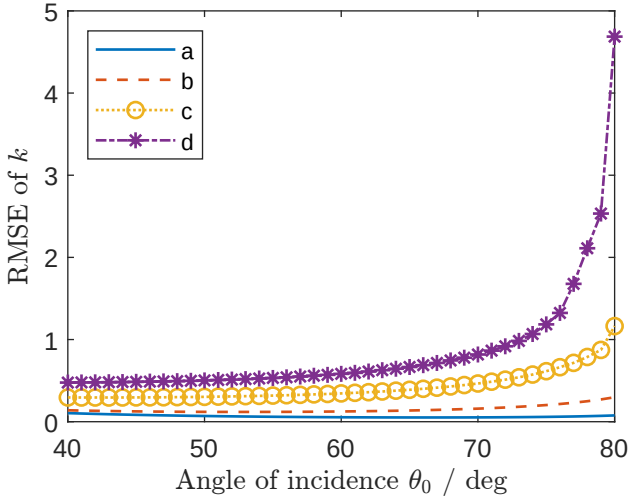

Figure 5.8: The RMSE for k between the angles of incidence of 40° and 80° for an aluminum mirror ($N = 1.4482 - 7.5367\mathrm{i}$). The uncertainty in the ellipsometric parameters ($u(\Psi)$,$u(\Delta)$) is (0.01°, 0.02°) and the uncertainty in the reflectance R is (a) $u(R) = 0$, (b) $u(R) = 0.001$, (c) $u(R) = 0.003$ and (d) $u(R) = 0.005$.

increases as k increases. Large errors (> 10%) in n and k occur in the region of high k ($k > 6.5$) and low n ($n < 1$).

The simulated results show that the proposed method can be used for different materials. For high-k and low-n materials, careful reflectance calibration and measurements are necessary to achieve accurate results, e.g., noise reduction can be used by averaging multiple measurements.

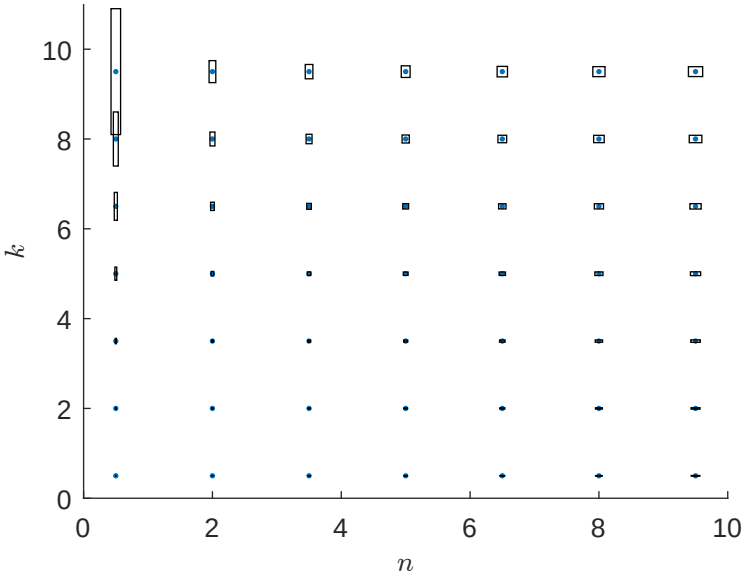

Figure 5.9: The RMSE for the complex refractive indices (n,k) at an angle of incidence of 60°. The uncertainty in the ellipsometric parameters $(u(\Psi),u(\Delta))$ is (0.01°, 0.02°) and the uncertainty in the reflectance R is $u(R) = 0.003$.

5.2 Numerical determination of the angle of incidence and film thickness for a three-phase system

An important case in ellipsometry involves reflection for a three-phase system (ambient/ film/ substrate), as shown in Figure 3.5, where N_0, N_1 and N_2 are the complex refractive indices for the ambient, film and substrate. θ_0 is the angle of incidence and d is the film thickness. Usually, the ambient space is air ($N_0 = 1$).

By substituting Equation 3.20 into Equation 3.46, ρ is written as:

$$\begin{aligned}\rho &= \tan\Psi e^{\mathrm{i}\Delta} = \frac{r_p}{r_s} = \frac{r_{012p}}{r_{012s}} \\ &= \frac{r_{01,\mathrm{p}} + r_{12,\mathrm{p}}\exp(-\mathrm{i}2\beta)}{1 + r_{01,\mathrm{p}} + r_{12,\mathrm{p}}\exp(-\mathrm{i}2\beta)} \cdot \frac{1 + r_{01,\mathrm{s}} + r_{12,\mathrm{s}}\exp(-\mathrm{i}2\beta)}{r_{01,\mathrm{s}} + r_{12,\mathrm{s}}\exp(-\mathrm{i}2\beta)}.\end{aligned} \tag{5.23}$$

Then ρ can be written as a quadratic function of X as [Azz87]

$$\rho = \tan\Psi e^{i\Delta} = \frac{A + BX + CX^2}{D + EX + FX^2}, \tag{5.24}$$

where

$$\begin{aligned}A &:= r_{01,\mathrm{p}},\ B := r_{12,\mathrm{p}} + r_{01,\mathrm{p}}r_{01,\mathrm{s}}r_{12,\,\mathrm{s}}, C := r_{12,\mathrm{p}}r_{01,\mathrm{s}}r_{12,\mathrm{s}}, \\ D &:= r_{01,\mathrm{s}},\ E := r_{12,\mathrm{s}} + r_{01,\mathrm{p}}r_{12,\mathrm{p}}r_{01,\,\mathrm{s}}, F := r_{01,\mathrm{p}}r_{12,\mathrm{p}}r_{01,\mathrm{s}},\end{aligned} \tag{5.25}$$

and

$$X := e^{-\mathrm{i}2\beta} = \exp\left[-\mathrm{i}\frac{4\pi d}{\lambda}\sqrt{(N_1^2 - N_0^2\sin^2\theta_0)}\right]. \tag{5.26}$$

It can be seen that X is a periodic function of the film thickness d for a fixed angle of incidence. The thickness cycle D_θ is defined as

$$D_\theta = \frac{\lambda}{2\sqrt{(N_1^2 - N_0^2 \sin^2 \theta_0)}}. \tag{5.27}$$

D_θ is a monotonically increasing function of θ_0 and only depends on N_0, N_1, θ_0 and λ.

In Equation 5.24, ρ, Ψ and Δ are a function of N_0, N_1, N_2, d, θ_0 and λ. If the refractive index (N_0, N_1 and N_2) and incident angle θ_0 are known, then the thickness d can be calculated using Ψ, Δ, θ_0 and λ by Equations 5.24 and 5.26.

For tilted samples, the ellipsometric parameters (Ψ and Δ) and the azimuthal rotational angle α are calculated by numerical fitting or by solving analytical solution of the polarization model, which is described in Sections 4.3 and 4.4. If the angle of incidence θ_0 is known, the nominal angle of incidence θ' and the angle of tilt ϕ are calculated using Equations 4.21 and 4.31. The thickness d is calculated using Ψ, Δ and θ_0. The AOI is usually measured or calculated using indirect methods, such as using a calibrated rotary stage or a goniometer [Liu16], and the spectroscopic data is fitted using a dispersion model [Li16, Duw19]. This study uses the simple inversion method of Easwarakhanthan and Ravelet [Eas96] to calculate the AOI because the calculation only requires ellipsometric parameters (Ψ and Δ) if the refractive index of the three-phase system is known.

In Equation 5.26, X is a function of N_0, N_1, N_2, d and λ. If the film is transparent, N_1 is a real number and X becomes a unit complex number in Equation 5.26. Then the absolute value of X can be written as:

$$|X| = 1. \tag{5.28}$$

The roots of Equation 5.24 are written as:

$$X = \frac{(\rho E - B) \pm \sqrt{(B - \rho E)^2 - 4(C - \rho F)(A - \rho)}}{2(C - \rho F)}. \tag{5.29}$$

The only unknown variable in the roots is the AOI θ_0 and θ_0 is solved using Equation 5.28 and the film thickness d is calculated using Equation 5.26. There are two solutions for θ_0 and d. Usually, only one solution fulfills the physical condition ($d \in \mathbb{R}$) and experimental setup (approximate range of θ_0).

To verify the proposed methods, a thickness sample (SiO_2/Si) was measured using a commercial spectroscopic ellipsometer (Smart SE, HORIBA). The nominal thickness is 82.9 nm and the standard deviation for the thickness is 1.5 nm. The respective refractive indices for the thin film and substrate at 635 nm are 1.457 and $3.868 - 0.016i$. The AOI for the ellipsometer is 70°. The measured ellipsometric parameters (Ψ, Δ) are 33.99° and 80.80°. Using the calculation for transparent films, θ_0 and d are solved sequentially. As previously noted, there are two solutions for this numerical method and one solution fulfills the physical condition ($d \in \mathbb{R}$ and $90° \geq \theta_0 \geq 0$). The calculation results are listed in Table 5.6. Solution 1 is wrong because the calculated angle of incidence is greater than 90°. Only solution 2 fulfills the physical condition and gives a value that is very close to the nominal values for the AOI and thickness.

Table 5.6: Calculation results for the measurement data for a sample (SiO_2/ Si) at an angle of incidence of 70°. The measured parameters for Ψ and Δ are 33.99° and 80.80°. Solutions 1 and 2 show the calculated parameters using Equations 5.24, 5.28 and 5.26.

	Sol. 1	Sol. 2
AOI θ_0	109.26°	69.98°
Thickness d	-	84.5 nm

Table 5.7 lists the results for the nominal values, the spectroscopic data analysis and the proposed method. Spectral fitting gives the most accurate results because 1276 different sets of ellipsometric parameters (between 440 nm and 1000 nm) from spectroscopic measurements are used to fit the AOI and the thickness. Compared to the nominal values, the fitting values are in good agreement, which proves that the ellipsometer is accurate. By the proposed method, the calculated AOI is very close to the fitted AOI ($\Delta\theta_0 = 0.06°$). The deviation in the thickness is 0.6 nm. The proposed method gives accurate results for the AOI and the thickness. Sources of error are the uncertainty in the measured ellipsometric parameters and the refractive index for the thin film and the substrate.

Table 5.7: Results for the nominal values, the spectroscopic data analysis and the proposed method.

	Nominal values	Spectral fitting	Proposed method
AOI θ_0	70.00°	69.92°	69.98°
Thickness d	82.9±1.5 nm	83.9 nm	84.5 nm

This method can be used for non-transparent films, i.e., absorbing films. For absorbing films, N_1 is a complex number. The condition for the unit complex number does not hold. The division of the root in Equation 5.29 and Equation 5.26 is unity and can be decomposed into polar form Y as:

$$Y = f(\theta_0,d) = re^{i\beta} = 1, (r,\beta) \in \mathbb{R} \rightarrow \begin{cases} r(\theta_0,d) = 1 \\ \beta(\theta_0,d) = 2m\pi, m \in \mathbb{Z} \end{cases}. \quad (5.30)$$

The absolute value and the argument for Y are 1 and $2m\pi$ ($m \in \mathbb{Z}$). There are two unknown parameters (θ_0,d) and two equations for Ψ, Δ, N_0, N_1 and N_2, which are known or measured variables. Hence, it is possible to solve the equations for θ_0 and d numerically. Equation 5.30 can be rewritten in a more convenient form to solve the non-linear equations as:

$$\begin{cases} |Y| = 1 \\ \tan\arg(Y) = 0 \end{cases}. \quad (5.31)$$

5.2.1 Uncertainty analysis

By using the proposed method for transparent films, the film thickness is determined using the angle of incidence and the ellipsometric parameters so the accuracy of the angle of incidence and the ellipsometric parameters has a significant effect on the film thickness. A Monte Carlo uncertainty analysis, which is described in Section 5.1.3 is used to determine the uncertainty in the angle of incidence and the film thickness. Only 10^3 Monte Carlo trials are used because an optimization function is used to solve X. The time for each trial is about 1 second. The probability density functions that are used for the Monte Carlo analysis are Gaussian distributions. The uncertainty in the amplitude ratio Ψ is between 0.01° and 0.1° and the uncertainty in the phase difference Δ is between 0.02° and 0.2° [Eas96]. Three different sets of Ψ and

Δ are used, depending on the measurement uncertainty for conventional ellipsometry. The root-mean-squared error is used to show the uncertainty in the angle of incidence and the thickness.

A three-phase system (air/SiO_2/Si) that is used as a calibration sample for ellipsometry is simulated at a wavelength of 632.8 nm. The respective refractive indices of air, SiO_2 and Si are 1, 1.457 and 3.871 – 0.016i, respectively. Figure 5.10 shows the variation in the RMSE for the AOI with the film thickness of 82.9 nm. The uncertainty in the AOI decreases as the angle of incidence increases. The maximum uncertainty in the AOI for the three different sets of ellipsometric parameters is better than 0.003° and the NRMSE is less than 0.01%. The simulated RMSE is much more accurate than if conventional rotary stages were used (±0.01°) so this method can be used to calculate or calibrate the angle of incidence.

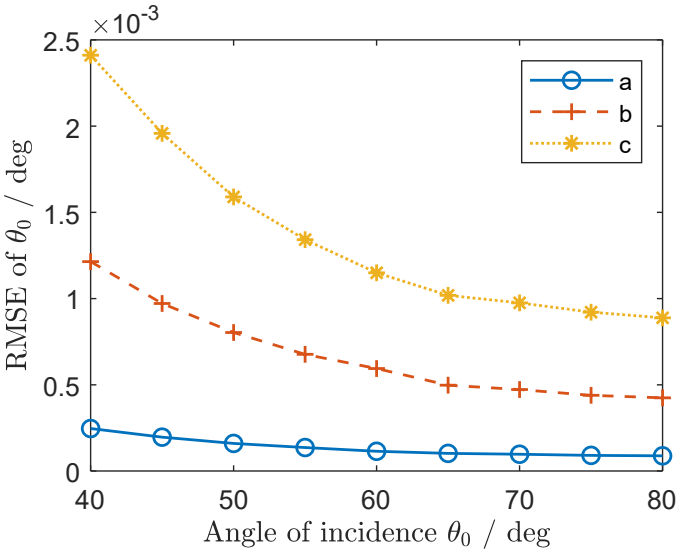

Figure 5.10: The RMSE for θ_0 between angles of incidence of 40° and 80° for a sample (SiO_2/Si) with a thickness of 82.9 nm. The uncertainty in the ellipsometric parameters ($u(\Psi)$,$u(\Delta)$) is (a) (0.01°, 0.02°), (b) (0.05°, 0.10°) and (c) (0.10°, 0.20°).

Figure 5.11 shows the variation in the RMSE for the thickness for Figure 5.10. There are large deviations at both ends. The maximum RMSE is 0.51 for curve (c) and the NRMSE is only 0.6%. These two plots show that the uncertainty in the ellipsometric parameters has a more significant effect on thickness than on the AOI.

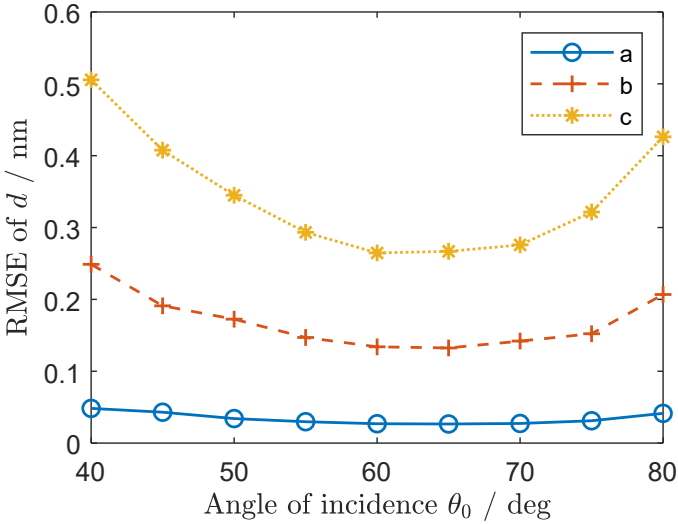

Figure 5.11: The RMSE for d between angles of incidence of 40° and 80° for a sample (SiO_2/Si). The uncertainty in the ellipsometric parameters ($u(\Psi)$,$u(\Delta)$) is (a) (0.01°, 0.02°), (b) (0.05°, 0.10°) and (c) (0.10°, 0.20°).

The film thickness for the sample also affects the uncertainty in the AOI and the thickness. For a fixed angle of incidence, X in Equation 5.26 is a periodic function of the thickness d. Substituting the same simulated parameters at an angle of incidence of 70° gives the thickness cycle D_θ as 284.1 nm. Figure 5.12 shows the trajectory up to a thickness of 280 nm. If the film thickness is greater than the thickness cycle, the trajectory follows the same path so the uncertainty analysis only considers thicknesses that are less than the thickness cycle.

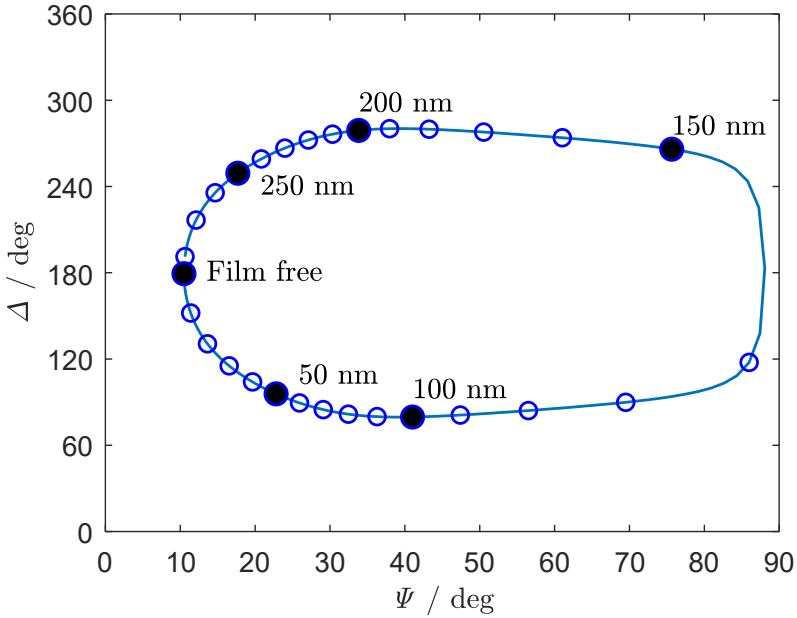

Figure 5.12: The trajectory (Ψ and Δ) for a sample (SiO_2/Si) at an incident angle of 70° and a wavelength of 632.8 nm. The range of thicknesses is from 0 to 280 nm with a interval of 10 nm. The thickness of the solid dots is shown in the text labels.

A range of thicknesses from 25 nm to 275 nm and an interval of 25 nm is used for the uncertainty analysis. The uncertainty in ellipsometric parameters (Ψ, Δ) is 0.1° and 0.2°. Figure 5.13 shows the variation in the RMSE uncertainty in the AOI and the thickness at an angle of incidence of 70°. The lowest value for the RMSE for the AOI and the thickness is achieved for a film thickness of 150 nm.

Figure 5.14 plots associated values of $|\rho|$ in Figure 5.13 versus thickness d. The peak value in Figure 5.14 is close to 150 nm. The curves in Figures 5.13 and 5.14 are highly Correlated. It is assumed that the uncertainty decreases if the value of $|\rho|$ is large.

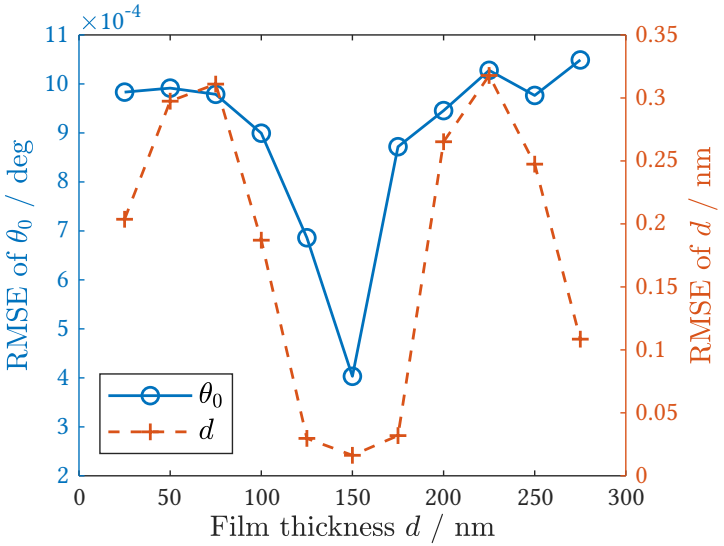

Figure 5.13: Variation in the RMSE uncertainty for the AOI and the thickness at an angle of incidence at 70° for a film thickness ranging between 25 nm to 275 nm.

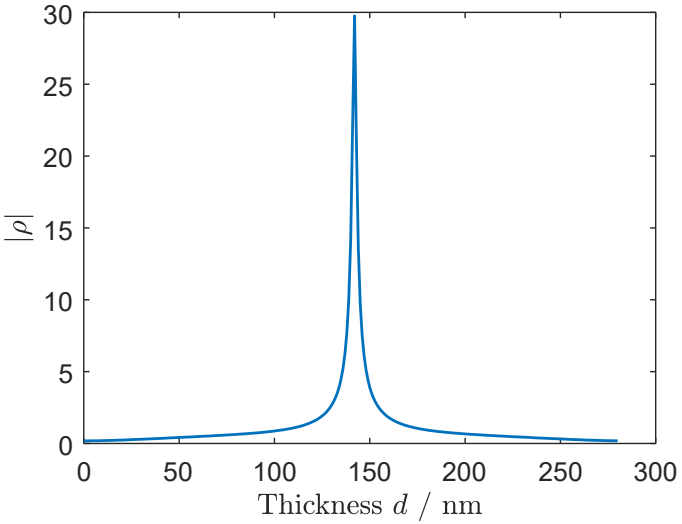

Figure 5.14: Associated values for $|\rho|$ in Figure 5.13 versus thickness d.

5.3 Analysis of ellipsometric measurements for nonplanar surfaces

From a micro perspective, a curved surface can be seen as a rotated flat surface if the illumination spot is a point, so the spot is infinitely small. However, the curvature of the surface has a significant effect on the measurement results, as shown in previous studies [Zha10, Kre11]. Křepelka analyzed ellipsometric data for a convex spherical surface using numerical simulation and geometrical and wave optics. Zhang et al. compared the experimental deviation with and without the aperture-filtering method. The simulation and experimental results showed that any deviation in the measurement is significantly correlated with the spot size of the light source and the shape of the surface. Therefore, the spot size should be taken into account in the calculation. This section analyzes a convex spherical surface using polarization ray tracing to determine the effect of the curved surface on retroreflex ellipsometry.

Figure 5.15 shows a spherical surface with a radius r and the center of the sphere is at $(0, 0, r)^{\mathrm{T}}$. An incident collimated beam $\mathbf{k}_0$ is reflected by the sample, where $\mathbf{k}_0$ is $(0, \sin\theta_0, -\cos\theta_0)^{\mathrm{T}}$. The spot size for the incident beams is defined as $2r_{\mathrm{i}}$. The central ray of the incident beams hits the origin point O and the angle of incidence for the ray is θ_0. To determine the effect of the curvature, the intersection points on the surface must be calculated. This problem can be redefined as the intersection of a sphere and a cylinder.

The function for a spherical surface and the surface normal $\boldsymbol{\eta}$ is written as:

$$x^2 + y^2 + (z - r)^2 = r^2, \tag{5.32}$$

$$\boldsymbol{\eta} = (x, y, z - r)^{\mathrm{T}}. \tag{5.33}$$

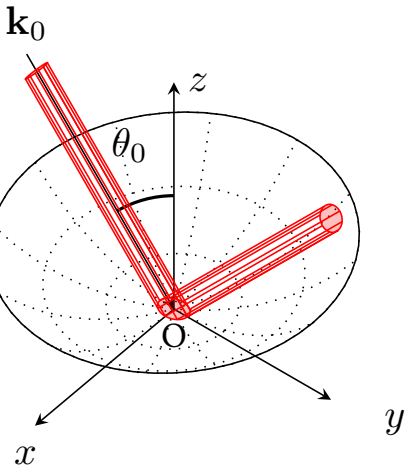

Figure 5.15: Schematic diagram of a concave spherical sample. The incident beam follows the direction $\mathbf{k}_0$ when it is reflected by the sample.

The incident beams $\mathbf{k}_0$ can be seen as a cylinder rotates θ_0 around x axis, which is described using a parametric equation as:

$$\begin{aligned}\begin{bmatrix} x \\ y \\ z \end{bmatrix} &= \begin{bmatrix} \cos\theta_0 & 0 & \sin\theta_0 \\ 0 & 1 & 0 \\ -\sin\theta_0 & 0 & \cos\theta_0 \end{bmatrix} \cdot \begin{bmatrix} r_c\cos\varphi \\ r_c\sin\varphi \\ L \end{bmatrix} \\ &= \begin{bmatrix} r_c\cos\varphi\cos\alpha + L\sin\alpha \\ r_c\sin\varphi \\ L\cos\alpha - r_c\cos\varphi\sin\alpha \end{bmatrix},\end{aligned} \tag{5.34}$$

where $r_\mathrm{i} \geq r_c \geq 0$, $360^\circ > \varphi \geq 0$ and $L \geq r$. By substituting Equation 5.34 into Equation 5.32, the parametric parameter L in Equation 5.34 can be solved as:

$$L = 2r_\mathrm{i}\cos\theta_0 \pm \frac{\sqrt{r_\mathrm{i}^2 - 2r_c^2 + r_\mathrm{i}^2\cos 2\theta_0 - 4r_\mathrm{i}r_c\cos\varphi\sin\theta_0}}{\sqrt{2}}. \tag{5.35}$$

In Equation 5.35, there are two solutions (L_1 and L_2), where L_1 is greater than or equal to L_2. L_1 represents the intersection with the concave surface and

L_2 represents the intersection with the convex surface. The surface is convex so the intersection points are calculated by substituting L_1 into Equation 5.34. Figure 5.16 shows an incident beam with a radius of 1 mm at an angle of incidence of 70° and its projection on a spherical concave surface with a radius of 175 mm. The center of the beam coincides with the origin point O. The area of the input beam is 3.14 mm^2 and the projection area on the xy- plane is 9.19 mm^2.

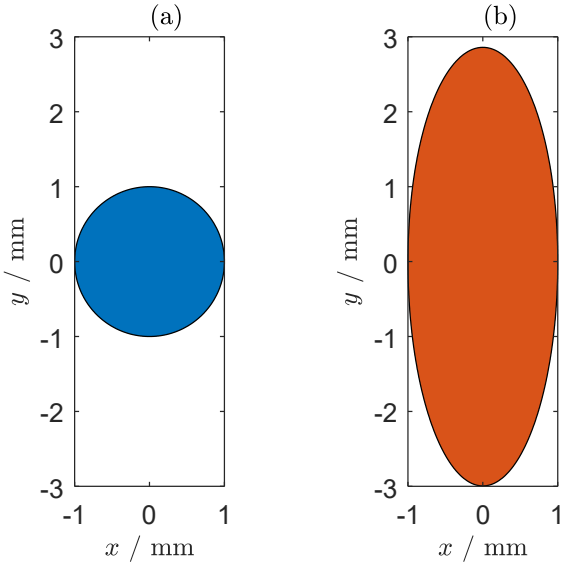

Figure 5.16: (a) An incident beam with a radius of 1 mm. (b) The projection of the incident beam at an incident angle of 70° on the spherical concave surface with a radius of 175 mm.

The local angle of incidence θ_0 and the tilt angle ϕ, which are defined in Section 4.3, are calculated using the surface normal $\boldsymbol{\eta}$ in Equation 5.33 and $\mathbf{k}_0$. Figure 5.17 shows the local distribution of θ_0 and ϕ. The AOI is between 69.06° and 70.98° and the maximum tilt angle is 0.33°. If the refractive index of the surface is $1.4482 - 7.5367i$, the local ellipsometric parameters (Ψ and Δ) and the reflectance R can be calculated using Fresnel's equations in Equation 3.11.

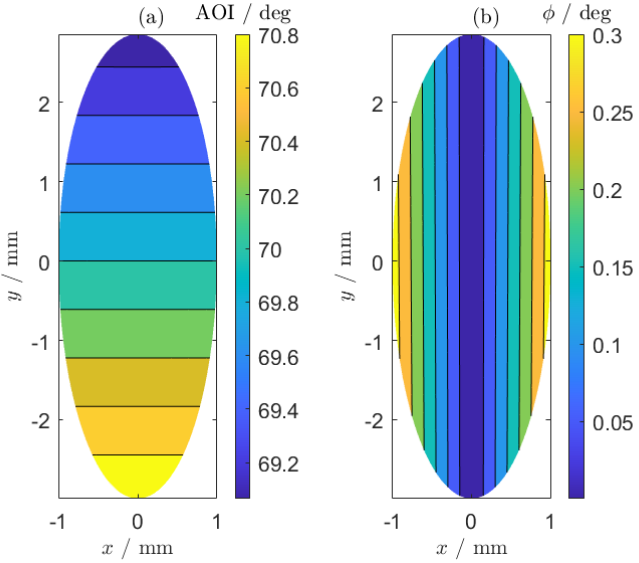

Figure 5.17: Local angle of incidence (a) and tilt angle (b) for a collimated beam with a radius of 1 mm that impinges on a sphere with a radius 175 mm.

Figure 5.18 plots the local distribution of Ψ, Δ and R. The local change in the ellipsometric parameters and reflectance is symmetrical with respect to the y axis. The value of Ψ ranges between 41.63° and 41.93° and the value of Δ ranges between 141.42° and 145.41°. The deviation in Δ is 3.99° and the deviation in Ψ is only 0.3°. The reflectance is the average of the magnitude squared of the amplitude reflection coefficients so any change in the reflectance R is very slight. The simulation shows that the range for R is between 0.8675 and 0.8729 and the deviation is 0.0054.

This analysis shows that the spot size and the angle of incidence are strongly correlated with the distribution of the local quantities (Ψ, Δ and R). Figure 5.19 shows the deviation and the standard deviation for local quantities for different spot sizes. Figure 5.20 presents the deviation and the standard deviation for the local quantities for different angle of incidence. The subscripts for average and center denote the average value and the center value. The length of the error bars is the standard deviation for the local quantities.

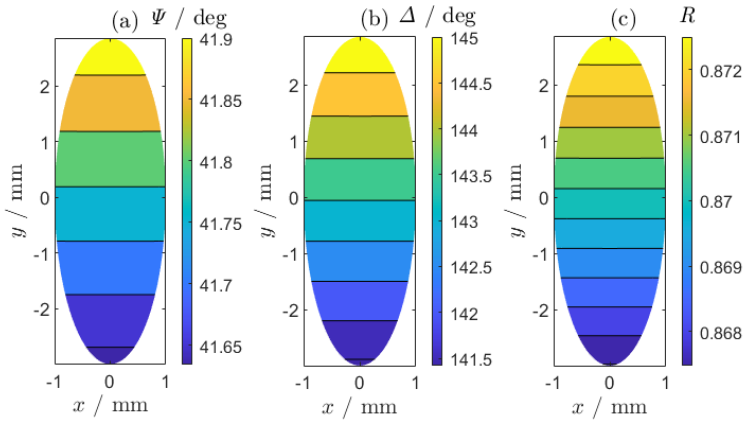

Figure 5.18: Local Ψ (a), Δ (b) and R (c) values for a collimated beam with a radius of 1 mm that impinges on a sphere with a radius 175 mm. The refractive index of the surface is $1.4482 - 7.5367\mathrm{i}$.

If there is an increase in the spot size or the angle of incidence arise, the deviation from the center value and the standard deviation for of Ψ, Δ and R increase. The plots show that the average value is less than the center value, so the real measurement value must be less than the nominal value at the center point of the incident beam because the surface is concave. An incident beam with a small spot size that impinges at a small angle of incidence gives more accurate measurement results. This calculation uses the local coordinate so the average value only has a statistical meaning because a polarimeter measures the average intensity and then transforms the measured values to Stokes vectors. Therefore, a direct average value for Ψ and Δ has no physical meaning but the local distribution of Ψ and Δ shows the effect of the shape of the surface.

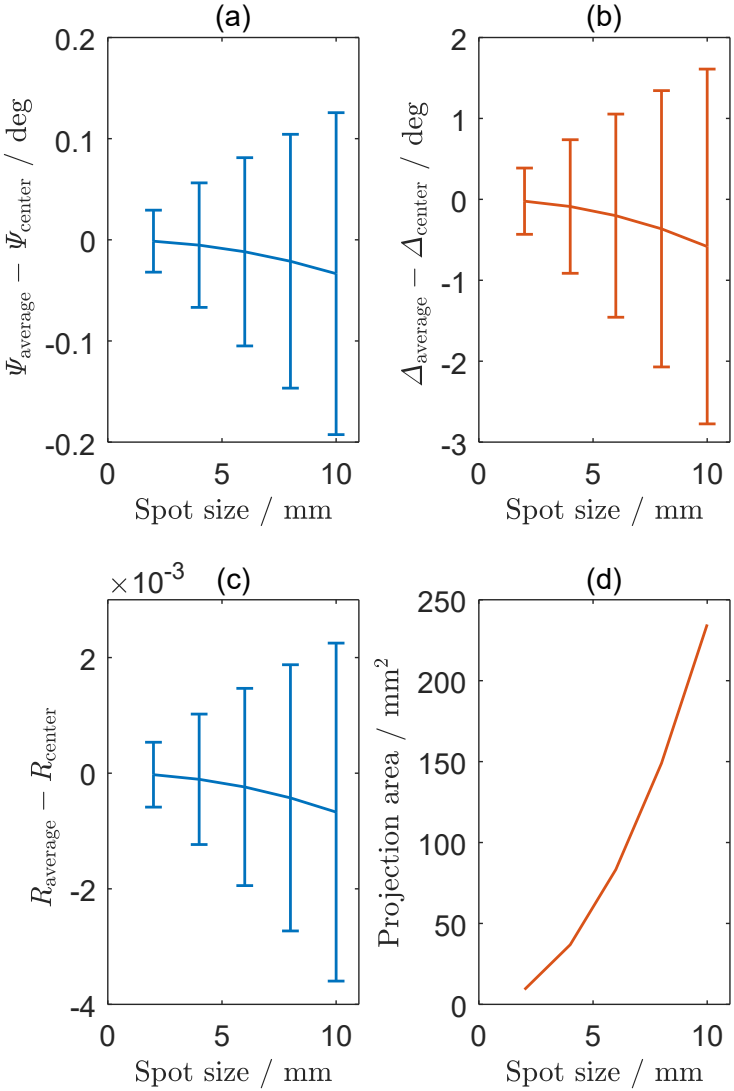

Figure 5.19: Deviation in the local Ψ (a), Δ (b), R (c) and projection area (d) values for different spot sizes.

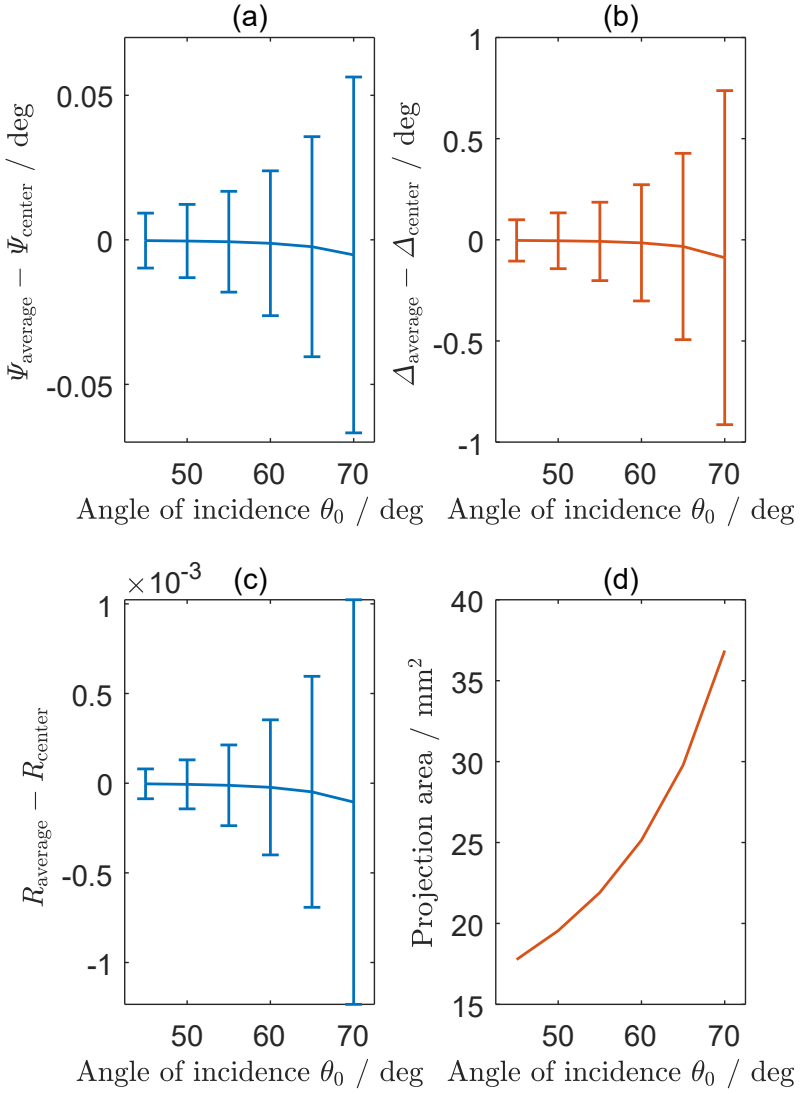

Figure 5.20: Deviation in the local Ψ (a), Δ (b), R (c) and projection area (d) values for different angles of incidence.

In terms of ellipsometry, the detector in the PSA measures only the light intensity. The average electric field $\mathbf{E}$ for the reflected beam is calculated as:

$$\mathbf{E}_{\text{Measured}} = \frac{\sum_{i=1}^{M} \mathbf{P}_{\text{Total},i} \mathbf{E}_{\text{Input}}}{M}, \tag{5.36}$$

where $\mathbf{P}_{\text{Total},i}$ is the net polarization transfer matrix for the measurement of the curved surface at the ith position and $\mathbf{E}_{\text{Input}}$ is the field for the input polarized light. The intensity is then calculated using Equation 3.5. From the definition of the 3D Jones matrix of the sample in Equation 4.24, $j_{11}^{(3)}$ and $j_{22}^{(3)}$ are measured using linear polarized light at 90° and 0°. The Ψ and Δ are calculated as:

$$\begin{aligned} \Psi &= \tan^{-1} |\frac{j_{22}^{(3)}}{j_{11}^{(3)}}|, \\ \Delta &= \arg(\frac{j_{22}^{(3)}}{j_{11}^{(3)}}). \end{aligned} \tag{5.37}$$

Using the simulation parameters for the previous analysis ($r = 175$ mm, $r_{\text{i}} = 1$ mm and $N_1 = 1.4482 - 7.5367\text{i}$), the measured values for Ψ and Δ are calculated using Equation 5.37. Figures 5.21 and 5.22 show the deviation in the measured values for Ψ and Δ from the center values. The measured values exhibit a greater deviation than the average values for the local distribution. The deviation in the value of Ψ and Δ increases dramatically with the angle of incidence so a small angle of incidence gives more accurate measured values.

Figure 5.23 shows the simulated raster scan for a concave mirror using uniform steps. The center incident collimated beam is on the yz plane, as shown in Figure 5.15. The angle of incidence for the center beam is 45° and the ratio of the spot size to the mirror's diameter is 1:20 to allow better visualization. Figure 5.24 plots the top view of the simulated spot distribution and the black point represents the centroid of the spot. The shape of the projection is irregular, especially if the spot is far from the origin. The spots are symmetrical along the y axis. The spot size decreases from the $-y$ to y direction because the angle of incidence decreases. The spot size increases from the origin along

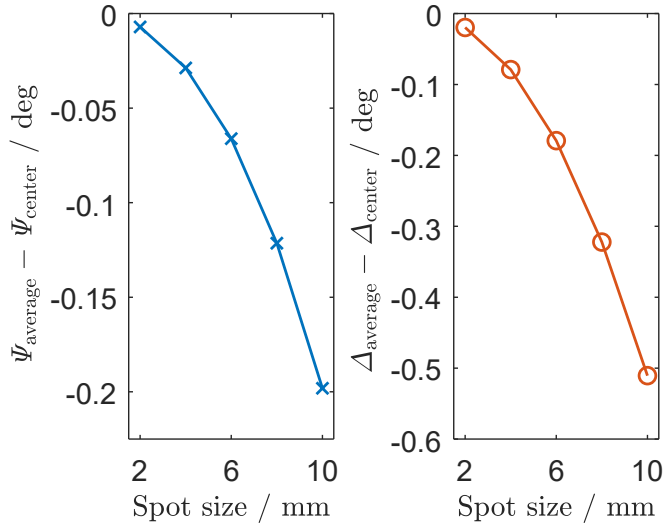

Figure 5.21: The deviation in the measured Ψ and Δ values for different spot sizes.

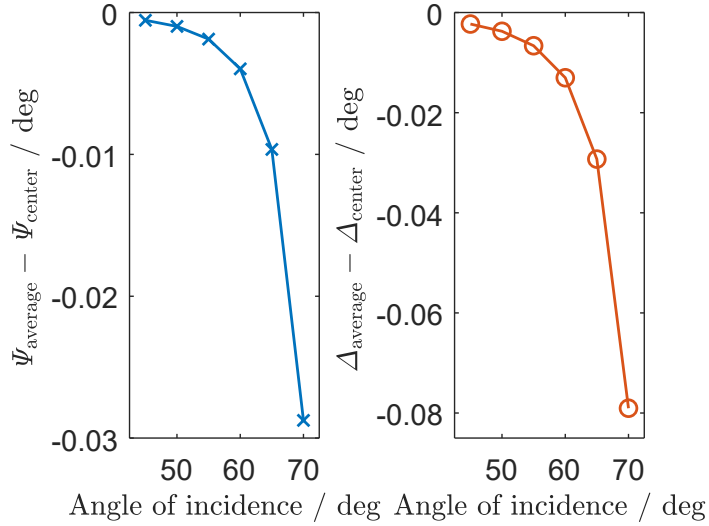

Figure 5.22: Deviation in the measured Ψ and Δ values for different angles of incidence.

the x direction and the $-x$ direction because increasing the angle of tilt increases the angle of incidence.

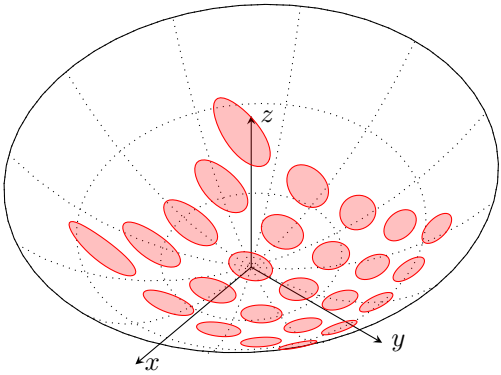

Figure 5.23: Simulated raster scan for a concave mirror using a uniform step. The center angle of incidence is **45°** and the ratio of the spot size to the mirror's diameter is 1:20.

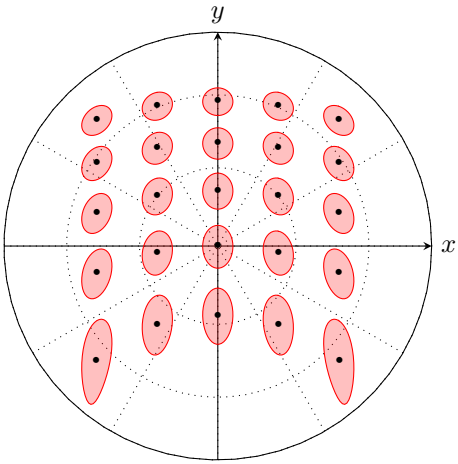

Figure 5.24: Top view of the simulated spot distribution on a concave mirror using xy scanning with a uniform step. The center angle of incidence is **45°** and the ratio of the spot size to the mirror's diameter is 1:20. The black dot is the centroid of the spot.

Figure 5.25 shows a simulated xy scan for a sample that moves along the x and y axes in uniform steps $0.2r$. If the surface is flat, the centroid of the spot lies at the intersections of the scanning lines. For a curved surface, the measured points are distorted geometrically. The x and y offsets for the centroid can be observed because the surface is concave spherical. If the sample moves along the y axis, the distance between each spot decreases. The surface inclination is calculated using the measurement results (θ_0, ϕ) so the surface can be reconstructed. Any distortion induces a reconstruction error so using a small region (e.g., $-0.2r < x,y < 0.2r$) or using a compensation method [Pil21] increases the accuracy of the surface reconstruction.

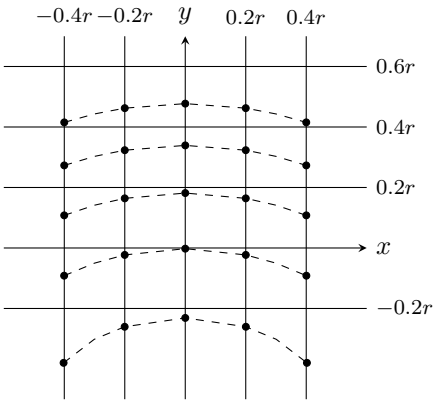

Figure 5.25: Centroid of spots on a spherical mirror using xy scanning.

5.4 Summary

This chapter proposes two simple methods used to obtain geometric information about two-phase and three-phase systems without the need for extra hardware. For a two-phase system, the direct relationship between the p- and s- polarizations and the angle of incidence is used to recover the phases of the p- and s- polarizations using the reflectance. If the detector is calibrated for reflectance measurements, the angle of incidence and the refractive index

for the substrate are calculated using reflectance and ellipsometric data. The uncertainty analysis for two-phase systems uses a Monte Carlo analysis. For transparent substrates, the uncertainty analysis shows a satisfactory result. The normalized RMSE for n is 0.9% for different materials ($1.5 \leq n \leq 2.0$) if the uncertainty in the ellipsometric parameters ($u(\Psi)$, $u(\Delta)$) is (0.01°, 0.02°) and the uncertainty in the reflectance is 0.003. For non-transparent substrates, the simulation results show that the RMSEs for n and k are greater than 10% if the AOI is appropriate. For high-k and low-n materials, careful measurements are necessary to ensure accurate results. The advantages of this method are:

1 The angle of incidence and the refractive index are determined using a single measurement of a set of reflectance and the ellipsometric data with closed form solutions.

2 The proposed method is suitable for high-speed measurements because the reflectance and the ellipsometric parameters can be measured by the same sensor. The AOI and the refractive index can be calculated without numerical fitting. It is fast to calculate the result and easy to analyze the uncertainty of the method.

3 An absolute intensity calibration is sufficient for the proposed method using an ellipsometer, without the need for extra hardware or modification.

For a three-phase system, the proposed method uses the properties of a complex exponential function X. If the thin film is transparent ($k = 0$), the angle of incidence is calculated using the refractive indices of the thin film and substrate and ellipsometric parameters so the film thickness can be calculated. If the thin film is not transparent ($k \neq 0$), the angle of incidence and the thickness are calculated by numerical optimization. The uncertainty analysis shows that the proposed method gives a highly accurate value for the AOI and the thickness for different AOIs and film thicknesses. For this method, the calculation for the AOI and thickness only requires ellipsometric parameters (Ψ, Δ), without the need for extra hardware, if the optical properties of the three-phase system are known. The proposed method gives a highly accurate result (better than 0.003°) for the angle of incidence. The method can also be

used for alignment or calibration, which is particularly important for in-situ and inline measurements. The proposed method can also be used as an initial solution for the AOI and film thickness to increase the speed of convergence and the accuracy of results.

Another important factor that affects the measurement result is the shape of the surface and the spot size. The local distribution for the measurement parameters is calculated and visualized. A small spot size and AOI reduces the measurement deviation in the Ψ, Δ and R values. When scanning a large surface, there is geometrical distortion. This distortion affects the result for the surface reconstruction so positional compensation or a small measurement region is necessary.

6 Results and discussion

The prototype retroreflex ellipsometry and calculation methods for two and three-phase systems are explained in Chapters 4 and 5. This chapter presents the system calibration and measurement results for planar and nonplanar samples. Section 6.1 provides the calibration result and the results of straight-through measurements. An uncoated gold mirror and an uncoated gold parabolic mirror are then measured and analyzed in Section 6.2. Section 6.3 gives the measurement results for a thickness sample and a coated spherical gold mirror.

6.1 System calibration

As described in Section 4.4, the NPBS must be calibrated first because it has non-ideal polarization properties. Figure 6.1 shows the normalized Stokes parameters that are generated by the PSG. The QWP rotates from 0° to 350° in steps of 10°. Each point represents the average for 100 measurements using a polarimeter. Figure 6.2 plots the corresponding standard deviation (SD) for the Stokes parameters in Figure 6.1. The average SD for the normalized Stokes parameters is 0.004 and the maximum SD is 0.005 for s_2 at a fast axis angle of 140°.

Using the procedure that is described in Figure 4.13, the normalized Mueller matrix for the NPBS for reflection is calculated as:

$$\hat{\mathbf{M}}_{\mathrm{NPBS,R}} = \begin{bmatrix} 1. & -0.177 & -0.003 & 0.002 \\ -0.128 & 0.953 & -0.015 & 0.005 \\ -0.001 & -0.014 & -0.949 & -0.247 \\ -0.0.01 & 0.008 & 0.249 & -0.940 \end{bmatrix}. \tag{6.1}$$

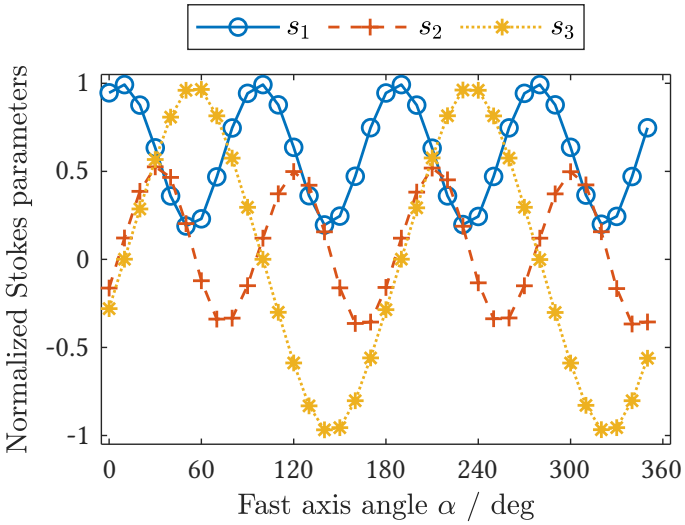

Figure 6.1: Normalized Stokes parameters that are generated by the PSG.

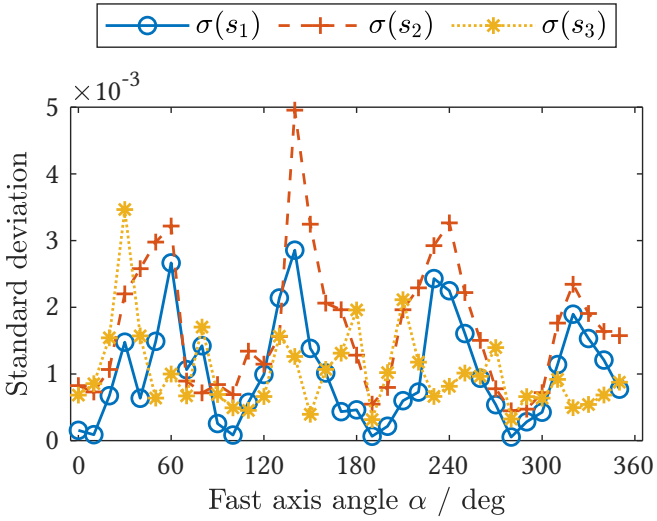

Figure 6.2: Standard deviation for the normalized Stokes parameters that are generated by the PSG.

The values for m_{12}, m_{21}, m_{34} and m_{43} exhibit large deviations (> 0.1), which shows that the NPBS is not an ideal optical element. The values for m_{12} and m_{21} represent diattenuation and polarizance and m_{34} and m_{43} correspond to retardation [Chi18]. These deviations distort polarization states when light travels through the NPBS.

After system calibration, a straight-through measurement (i.e., no sample) with the retroreflector was performed to verify the calibration. In this configuration, the Mueller matrix for the ideal straight-through measurement is the same as the Mueller matrix for an ideal mirror, which is a diagonal matrix that is given by diag(1, 1, -1, -1). The measurement results are:

$$\hat{\mathbf{M}}_{\text{Air,mean}} = \begin{bmatrix} 1. & -0.013 & -0.001 & -0.001 \\ -0.012 & 1. & 0. & -0.003 \\ -0.004 & 0.002 & -0.987 & 0.003 \\ 0. & -0.001 & 0.007 & -1. \end{bmatrix}, \tag{6.2}$$

$$\hat{\mathbf{M}}_{\text{Air},\sigma} = \begin{bmatrix} 0. & 0.001 & 0.001 & 0.002 \\ 0.004 & 0.005 & 0.003 & 0.001 \\ 0.002 & 0.003 & 0.005 & 0.003 \\ 0.001 & 0.001 & 0.005 & 0.002 \end{bmatrix}, \tag{6.3}$$

where $\hat{\mathbf{M}}_{\text{Air,mean}}$ indicates the mean normalized Mueller matrix for ten different measurements and $\hat{\mathbf{M}}_{\text{Air},\sigma}$ denotes the standard deviations for each element. In Equations 6.2 and 6.3, the systematic deviations (errors) for the elements of the Mueller matrix from the arithmetic mean are less than 0.013 and the standard deviation is less than 0.005.

The result for straight-through measurements also demonstrates the polarization properties of the retroreflector. The ellipsometric parameters Ψ and Δ are transformed from the Mueller matrix. The average Ψ and Δ values for the retroreflector are 44.82° and 180.04°, which is in good agreement with the simulation result for the retroreflector in Section 4.2.

The main source of error is the deviation in the intensity due to the laser, the polarimeter and the system alignment. The accuracy of the polarimeter in

the prototype is better than 0.009 for Stokes parameters. Figure 6.3 shows the average intensity (S_0) and the standard deviation when the QWP is rotated.

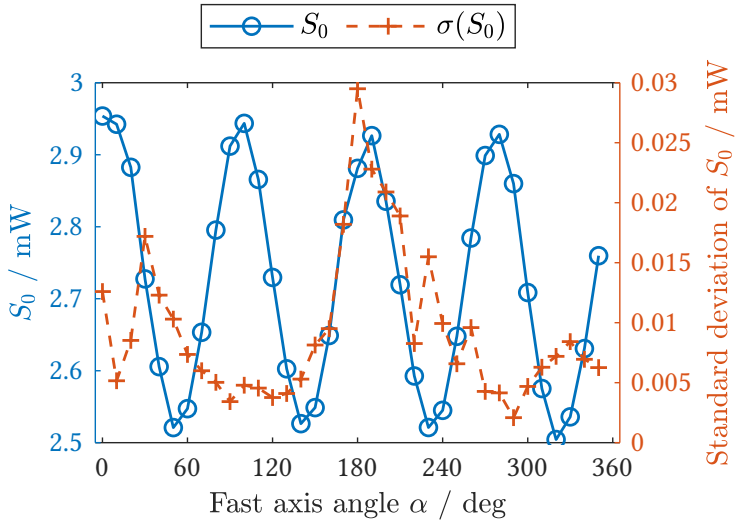

Figure 6.3: Average and standard deviation of the Stokes parameter S_0 that are generated by the PSG. The fast axis of the QWP is rotated from 0° to 350° in steps of 10°.

The maximum normalized SD is 1.0% and there is a ripple effect because there may be misalignment or multiple internal reflections in the QWP [Ait01]. Misalignment results in non-linear polarization properties for the QWP and multiple reflections lead to intensity modulation. If the uncertainty in the intensity (1.0%) is used for the calculation, the simulated standard deviation for the straight-through measurement is:

$$\hat{\mathbf{M}}^{\mathrm{Sim}}_{\mathrm{Air},\sigma} = \begin{bmatrix} 0. & 0.001 & 0.001 & 0.003 \\ 0.005 & 0.005 & 0.001 & 0.003 \\ 0.005 & 0.003 & 0.003 & 0.003 \\ 0.002 & 0.001 & 0.001 & 0.001 \end{bmatrix}. \tag{6.4}$$

The simulated standard deviation is in good agreement with the experimental result. The uncertainty is reduced by better aligning the QWP and by increasing the stability of the laser and the polarimeter.

6.2 Two-phase systems

To validate the retroreflex ellipsometry, measurements for an unprotected gold mirror (PF10-03-M03, Thorlabs Inc.) were made and these are compared with the results for a commercial spectroscopic ellipsometer (HORIBA Smart SE) with a straight-through air accuracy for $\Psi = 45° \pm 0.05°$ and $\Delta = 0° \pm 0.2°$. The gold mirror was rotated using a motorized stage. The angle of incidence for the gold mirror was varied from 51° to 61° in steps of 1°. The Mueller matrix was measured and the ellipsometric data (Ψ, Δ) and azimuthal rotation angle α were calculated by fitting. The compensated values for Ψ and Δ are applied to the experimental ellipsometric parameters.

Figure 6.4 shows the experimental results and the calculated results using the refractive index that is measured using the HORIBA Smart SE. The results show good agreement between the measured and calculated values, with respective mean absolute errors for Ψ and Δ of 0.14° and 0.02°. The experiments show that the retroreflex ellipsometer measures changes in the tilt angle and the angle of incidence and the results show that this prototype is highly accurate and stable. There is a systematic error in the amplitude ratio Ψ, possibly because of the effect of the spot size. This error increase as the AOI increases. The system was calibrated using the transmission configuration with the beam perpendicular to the mirror. In the reflection configuration, the projection area for the input beam increases as the angle of incidence increases.

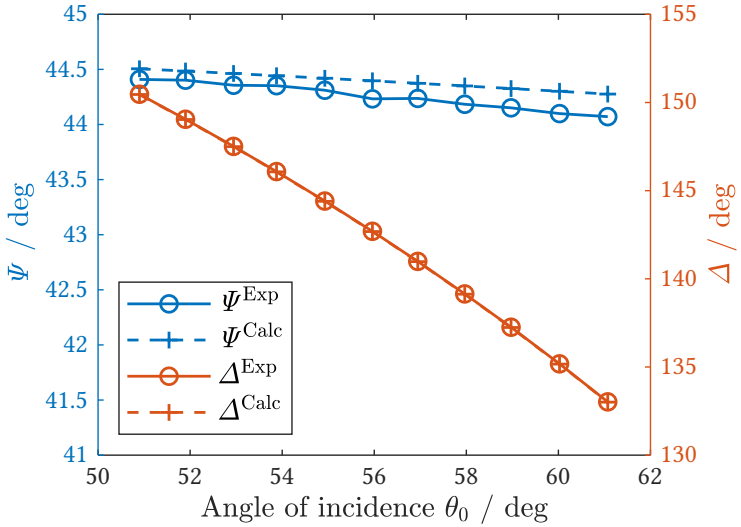

Figure 6.4: Experimental results for an uncoated gold mirror as the angle of incidence varies from 51° to 61°. The refractive index for the gold mirror is 0.1295 − 3.5323i, as measured by HORIBA Smart SE.

Another experiment used an off-axis parabolic mirror (MPD249-M03, Thorlabs Inc.). The refractive index for the parabolic mirror was measured as 0.241−3.239i by HORIBA Smart SE. Figure 6.5 shows the measurement setup. The incident beam on the retroreflex ellipsometer is parallel to the mechanical axis of the mirror and the parabolic mirror moves perpendicular to its mechanical axis from -3 to 3 mm. The angle of incidence angle changes from 44.14° to 45.83°. When the parabolic mirror and the retroreflector were fixed, there was no need to adjust the relative distance or the angle during the measurement because the retroreflector has an acceptable angular range of ±30°. This feature allows the measurement of curved surfaces and increases the ease of alignment so the installation of the retroreflector and the sample is flexible. The angle of incidence θ_0 and the complex refractive index N are calculated by Equations 5.18 and 5.5, and the measurement results are shown in Figure 6.6 and Table 6.1. The average complex refractive index ($N = n - ik$) is 0.207−3.192i and the standard deviation is 0.006 and 0.008, respectively. The average errors are 0.034 and 0.047 for n and k. This experiment demonstrates

that the method can be used to measure complex refractive indices at curved surfaces. The value of n has a higher relative error (14%) than that of k (1%) because the angle of incidence is close to 45°. The amplitude ratio Ψ and the reflectance R are relatively insensitive to the angle of incidence so a slight measurement error in the system induces a large error in the real part of the refractive index during the calculation process.

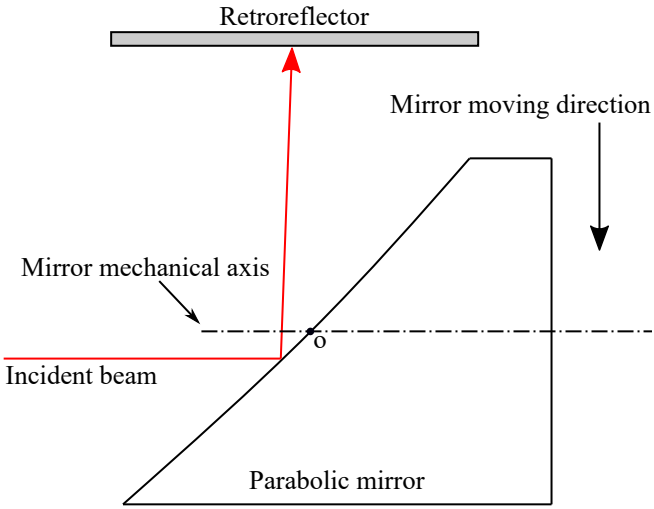

Figure 6.5: Schematic illustration showing the parabolic mirror and the scanning direction: O is the center of the parabolic mirror.

Although experimental errors remain in the experiment, the result obtained is sufficient for many industrial applications such as distinguishing between the materials silver and aluminum and between gold and pyrite. Several sources of error exist in the experiments, such as the surface roughness of the sample and the stability of the laser. The sample surface roughness may cause a diffuse reflection on the surface, thus nullifying the assumption of pure specular reflection.

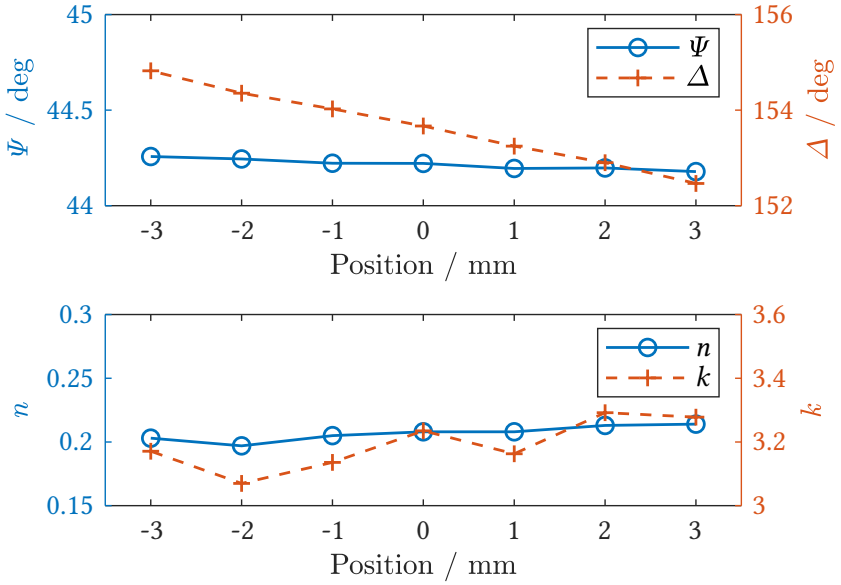

Figure 6.6: Experimental result of the parabolic mirror moving along its mechanical axis. Amplitude ratio Ψ, phase difference Δ and tilt angle ϕ are obtained from the measured Mueller matrices. Angles of incidence θ and complex refractive index ($N = n - ik$) are calculated using Ψ, Δ and reflectance R.

Table 6.1: Experimental refractive indices of the parabolic mirror calculated by the proposed method, showing the standard deviation (SD), and the differences (Δn and Δk) from the reference value $0.241 - 3.239$i (as measured by the HORIBA Smart SE).

Position (mm)	n	Δn	k	Δk
-3	0.203	0.038	3.171	0.068
-2	0.197	0.044	3.070	0.169
-1	0.205	0.036	3.136	0.103
0	0.208	0.033	3.235	0.004
1	0.208	0.033	3.163	0.076
2	0.213	0.028	3.292	-0.053
3	0.214	0.027	3.278	-0.039
Average	0.207	0.034	3.192	0.047
SD	0.006	-	0.008	-

6.3 Three-phase systems

To validate the polarization model for curved surfaces and inverse calculation, a flat sample and a spherical mirror are measured and analyzed by the retroreflex ellipsometer. The wavelength of the light source was 635 nm and a flat sample was rotated using a rotary stage (LMG40T4, Zaber Technologies Inc.), which has a repeatability of 0.005°. The unidirectional accuracy is not listed in the specification and the stage is discontinued but for the replacement product (GSM40-T4, Zaber Technologies Inc.), the unidirectional accuracy is 0.06°, which is used for the rotary stage in the experiments. The Mueller matrix was measured and the ellipsometric data (Ψ, Δ) and azimuthal rotation

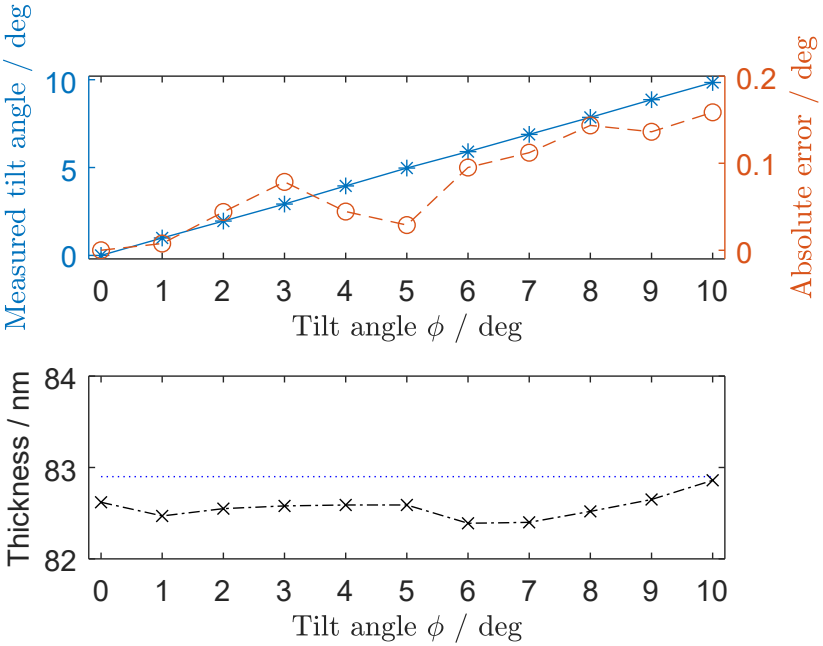

Figure 6.7: Measurement results for a flat sample (SiO_2/ C-Si). The tilt angle ϕ varies from 0° to 10° in steps of 1°.

angle α are calculated using the numerical fitting, which is described in Section 4.3. The angle of incidence θ_0 and the tilt angle ϕ and film thickness d are calculated using the proposed method.

The flat sample was SiO_2/c-Si with a nominal film thickness d of 82.9 $\pm$ 1.5 nm, where c-Si is crystalline silicon. Figure 6.7 shows the results for a tilt angle ϕ from 0° to 10° using steps of 1° at an angle of incidence of 70°. The mean absolute error in the tilt angle is 0.09°. The measured values are in good agreement with the reading for the rotation stage.

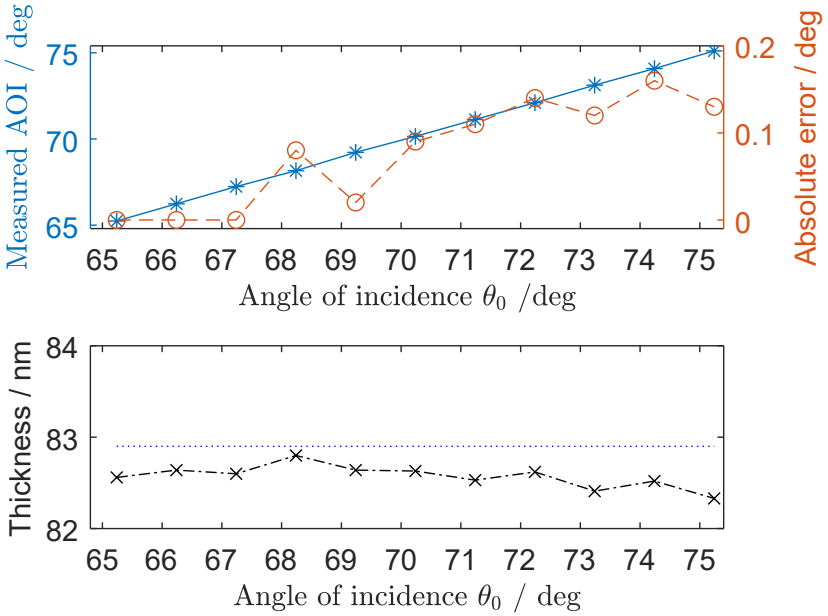

Figure 6.8: Measurement results for a flat sample (SiO_2/ C-Si). The angle of incidence θ_0 varies from 65° to 75° in steps of 1°.

The second experiment varied the angle of incidence of the flat sample from 65° to 75° in steps of 1°. The results are shown in Figure 6.8. The mean absolute error in the measured and calculated values for the AOI is 0.13°, whose values are very similar. The results for the thickness measurements for both

experiments are within the range of the nominal thickness (82.9 ± 1.5 nm), which verifies the proposed method.

The first and the second experiments show that the retroreflex ellipsometer measures the film thickness and changes in the angle of incidence and the tilt angle. The measurement results show that the retroreflex ellipsometer and the proposed method are very accurate and stable. There are several sources of error in the experiments, such as the alignment and the accuracy of the rotary stage. The sample was not placed at the center of rotation so there is a slight change in the beam occurred during the measurements due to variation in the film thickness. The stage also has no encoder and the unidirectional accuracy of the stage is about 0.06°. The accumulated error of the stage can increase the error in the tilt and angle of incidence.

Another experiment measured a protected gold-coated concave mirror (CM508-150M01, Thorlabs Inc.). The diameter of the concave mirror is 50.4 mm but the refractive indices for the thin film and substrate are not provided by the vendor so the refractive index for an unprotected gold mirror (PF10-03-M03, Thorlabs Inc.) was measured as $0.130 - 3.532i$ using a commercial ellipsometer (HORIBA Smart SE) and this value is used as the refractive index for the substrate for the spherical mirror. The center of the concave mirror was measured using the ellipsometer. Data analysis was used to determine the refractive index for the film ($1.405 - 0.004i$) at a wavelength of 635 nm and the film thickness (138.5 nm). The concave mirror was then measured using the retroreflex ellipsometer with a xy linear stage. The steps for the x- and y- axes were 5 mm. Figure 6.9 shows the measurement results for Ψ and Δ. The AOI and the angle of tilt are calculated as shown in Figure 6.10.

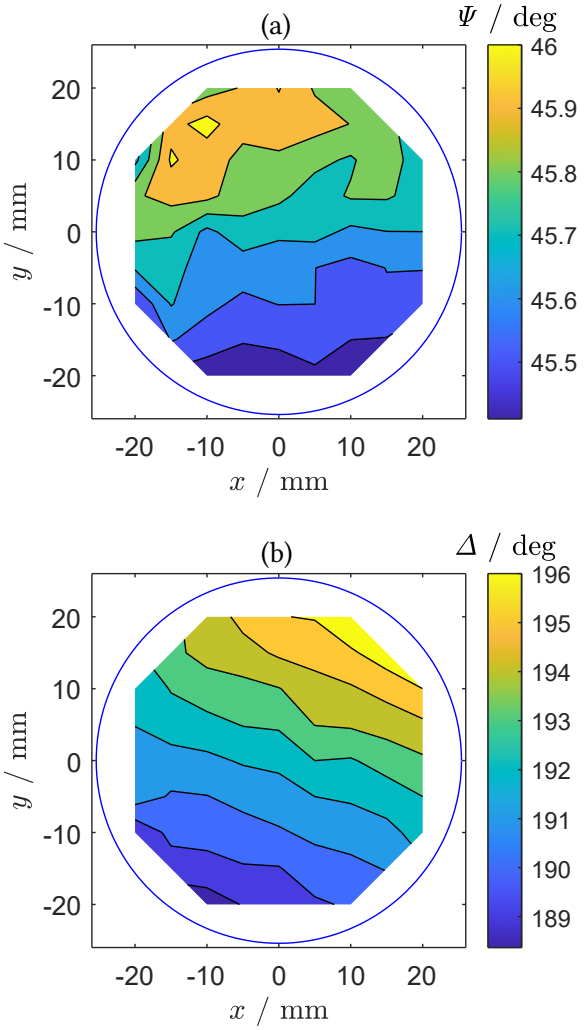

Figure 6.9: Contour plots for the measurement results for (a) Ψ and (b) Δ. The circle represents the diameter of the concave mirror.

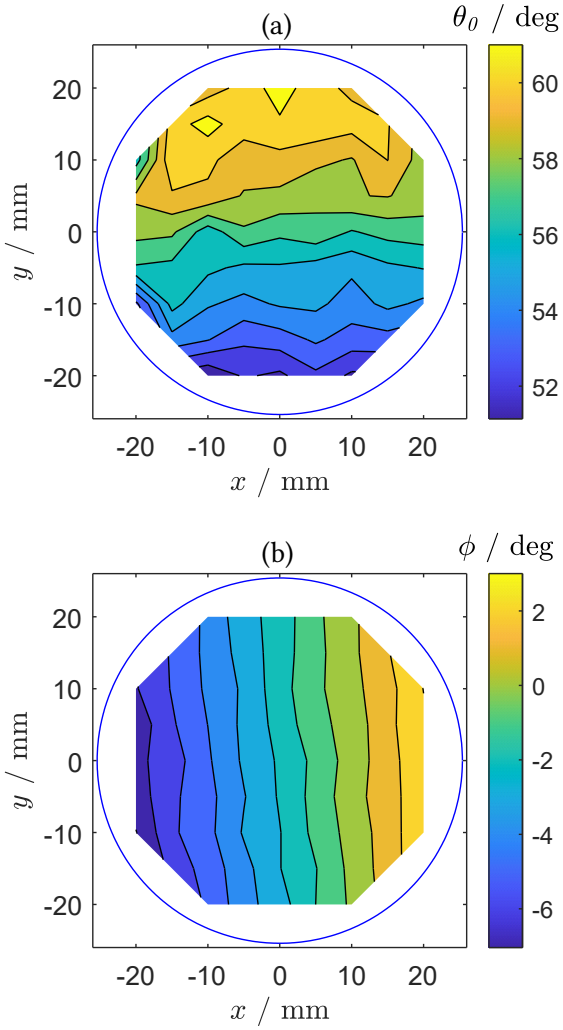

Figure 6.10: Contour plots for the measurement results for (a) θ_0 and (b) ϕ. The circle represents the diameter of the concave mirror.

The measurement setup and the thickness distribution are shown in Figures 6.11 and 6.12. The center thickness is 138.0 nm and the average thickness is

138.2 nm. These values are in agreement with the value obtained using the commercial ellipsometer. This experiment demonstrates that film thickness can be measured for curved surfaces. The measurement results show that the distribution of the film thickness is not uniform: the thickness increases along the direction of 45° in Figure 6.12. The reason for the non-uniformity may be the coating process. Samples that are placed on a holder rotate about the optical axis of a rotary stage during deposition [Ris02]. The tangential speed affects the deposition thickness.

It is worth mentioning that If the concave mirror and the retroreflector are fixed, there is no need to readjust the relative distance or the angle during a measurement and the measurement range depends on the size of the retroreflective sheet. Therefore, nonplanar surfaces on large samples can be measured and alignment is easy the installation of the retroreflector and the sample is flexible.

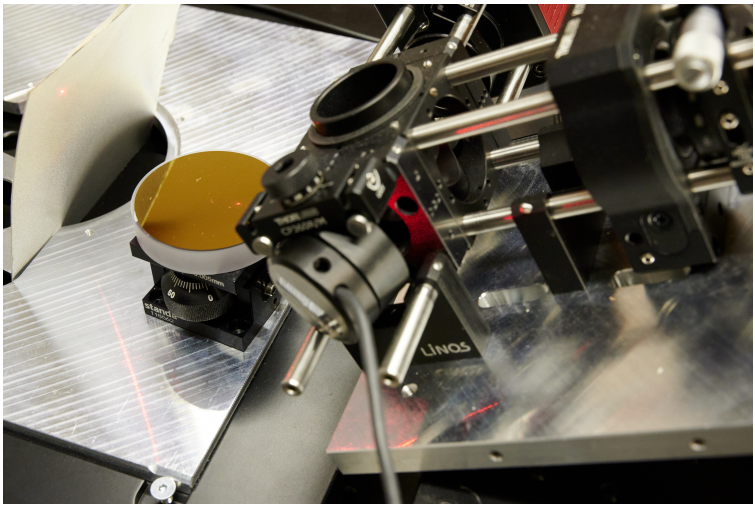

Figure 6.11: (a) Measurement setup for a protected gold-coated concave mirror.

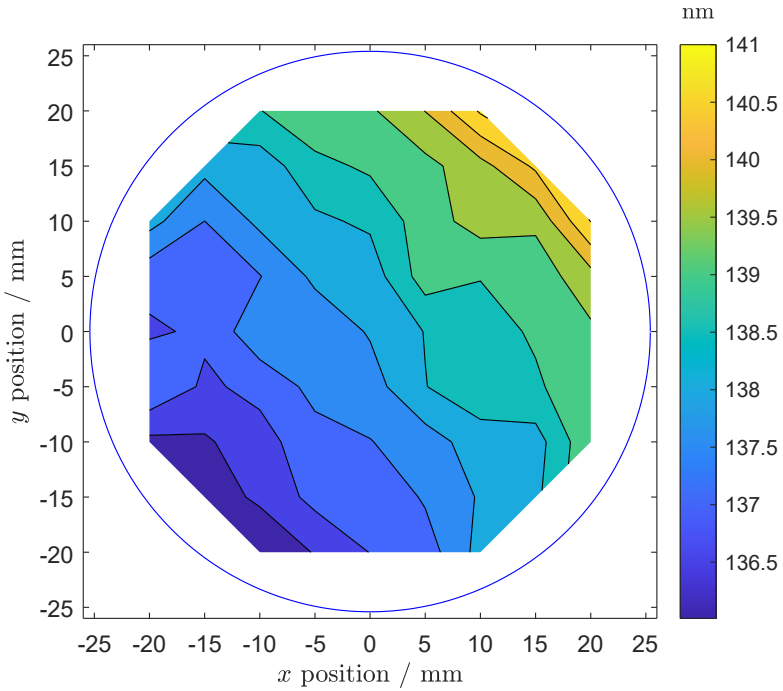

Figure 6.12: Contour plot for the measurement results for the concave mirror. The circle represents the diameter of the mirror.

The surface orientation (θ_0 and ϕ) is known so the surface can be reconstructed by numerical gradient integration. The calculation procedures are described in [Har13]. Figure 6.13 shows the reconstruction result. When the reconstruction data is fitted with the nominal radius of 150 mm, the center point can be determined. The RMSE for the surface height is 33.3 µm and the coefficient of determination for the fitting R^2 is 0.98. The main source of error is the distortion due to the curvature of the surface, which is detailed in Section 5.3. Distortion can be reduced by using a small angle of incidence or by compensating the x and y coordinates.

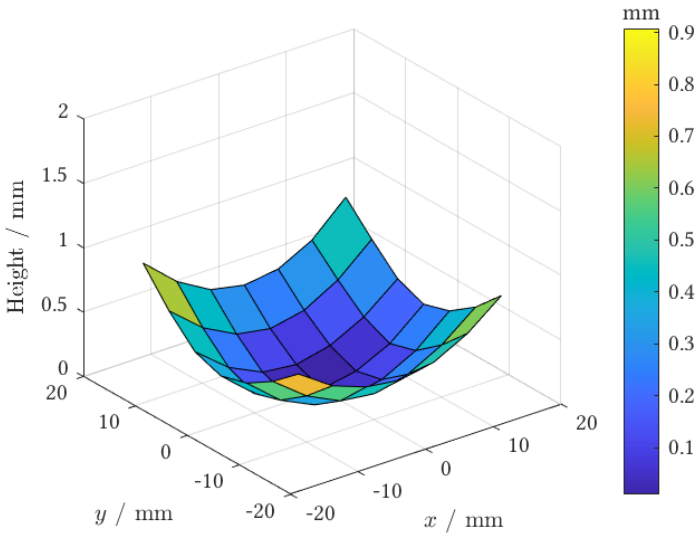

Figure 6.13: Surface reconstruction of the spherical mirror using measured data.

7 Conclusion and outlook

This dissertation develops a holistic solution for ellipsometric measurement of nonplanar surfaces. In this final chapter, the results and contribution of this thesis are summarized and improvements in the prototype and analysis methods are postulated. Opportunities for future study and application are also presented.

7.1 Conclusion

Conventional ellipsometry is only suitable for planar or near-planar surfaces. Measurement of nonplanar surfaces involves time-consuming alignment of the sample and only several sampling points are measured. In the worst case, the sample cannot be measured using conventional ellipsometry due to high curvature. This constraint limits the use of ellipsometry in industrial applications. However, quality monitoring or characterization of nonplanar surfaces is required for different applications, such as the uniformity of metallic coatings and functional coatings on lenses for anti-reflection coatings and self-cleaning properties.

A holistic approach is proposed to resolve this problem: retroreflex ellipsometry. Retroreflex ellipsometry uses a retroreflective sheet that returns a light beam from the sample back along the same beam path. The polarization properties of the retroreflector are also nearly the same as those for an ideal mirror at an angle deviation of $\pm 30°$. The alignment condition for the sample and the detector is automatically fulfilled, so retroreflex ellipsometry can be used to measure nonplanar surfaces without the need for manual adjustment.

This study determines the polarization characteristics of the retroreflector using simulation and experimental results, which are in good agreement. A polarization model for the measurements of nonplanar surfaces is developed using polarization ray tracing. The relationship between the angle of incidence θ_0, the tilt angle ϕ and the azimuthal rotation angle α is determined mathematically with no need for local coordinate transformation. A prototype that uses a dual rotating-compensator configuration with a single wavelength laser (635 nm) is constructed to verify the concept. After alignment and calibration, the accuracy of the elements of the Mueller matrix for the straight-through measurement (air) is better than 1.3% and the uncertainties in Mueller matrix elements are less than 0.5%. The deviation in the amplitude ratio Ψ and the phase difference Δ are 0.18° and 0.04° for the straight-through measurements. This result also shows that the polarization properties of the retroreflector are similar to an ideal mirror.

Based on retroreflex ellipsometry, two methods for two- and three-phase systems are proposed to determine the angle of incidence. For transparent ($k = 0$) and non-transparent ($k \neq 0$) two-phase systems (ambient/ substrate), two solutions are derived using the direct relationship between the p- and s- polarizations and the angle of incidence to determine the phases of the p- and s-polarizations using reflectance and ellipsometric parameters. These methods are used to determine the optical properties of isotropic substrates with nonplanar surfaces with no prior information about materials or the angle of incidence. For a three-phase system (ambient/ film/ substrate) with a transparent film, the angle of incidence is calculated using only ellipsometric parameters and the refractive index for the film and the substrate to determine the film thickness. The method can also be used for non-transparent films via numerical inversion of the AOI and the film thickness. The uncertainty for these methods is determined using a Monte Carlo simulation and the measurement deviations due to the curvature of the surface is evaluated.

The prototype ellipsometer achieved accordance of 0.14° for the amplitude ratio Ψ and 0.02° for the phase difference Δ to the measurements of a commercial ellipsometer at a gold plane mirror (two-phase system). The device can

determine the optical properties of isotropic substrates with nonplanar surfaces by measurements of reflectance R and ellipsometric data (Ψ, Δ) without a priori information about materials and angle of incidences. For the experiment with a parabolic mirror, the average respective measurement errors in the complex refractive index (n, k) are 0.034 and 0.047. For the experiments using a three-phase system (SiO_2/ C-Si), the mean absolute error in the angle of incidence is 0.09° and in the angle of tilt is 0.13°. For the experiment using a protected gold concave mirror, the deviation in the center thickness between the commercial and the retroreflex ellipsometer is 0.5 nm. The surface of the mirror is reconstructed using the surface orientation. The RMSE for the surface height is 33.3 µm.

Retroreflex ellipsometry addresses the geometric restrictions of conventional ellipsometry because samples need not have flat surfaces so ellipsometric measurements can be used for many industrial production processes for the characterization of optical properties of freeform optics or to inspect for defects in a sample with an arbitrary shape. The retroreflex ellipsometer can be used for differently shaped surfaces and the complexity of the system is simple. It can also be used for inline and in situ quality control systems because the maximum acceptable angular range for the reflection or refraction of beams at the sample is ±30°. so it can be used for free-form optics, flexible LED display modules and to monitor the coatings on lenses and mirrors.

7.2 Outlook

The retroreflex ellipsometer can measure nonplanar surfaces with satisfactory results. Nevertheless, there is still room for improvements in the prototype, e.g., optimizing optical elements and reducing the measurement time. In addition, potential research directions and applications are also presented and discussed in this section.

Improvements in hardware

Currently, only a single wavelength light source is used in the retroreflex ellipsometer so only two unknown variables can be solved. It is also possible to use multi-wavelength light sources for the retroreflex ellipsometer, such as a supercontinuum white light laser [Zim19] or a laser diode combiner [Sta08]. Multiple wavelengths give more information to determine the material properties of samples and allow a more robust calculation. The refractive index for the film is determined using a dispersion model. The methods that are proposed by this study can be used to determine an initial solution for the AOI and film thickness to improve the speed of convergence and accuracy of results.

The prototype for this study uses a dual rotating-compensator configuration, which features two mechanical rotary stages that rotate two quarter-waveplates. However, the optimum retardance for the PSG and PSA is 127°, which achieves the minimum condition number for the Mueller matrix calculation [Smi02]. Dual rotating-compensator ellipsometry is a simple and cost-effective configuration but the mechanical rotation stages can cause the beam wandering, vibration, a non-uniform rotation speed and positional errors, which induce measurement errors in the calibration and the determination of the Mueller matrix. The rotational speed also limits the measurement time because there are mechanical constraints. For large samples, measurements must be fast. Liquid crystal variable retarders (LCVRs) and photoelastic modulators (PEMs) allow fast phase-modulation for the polarization state generator and polarization state analyzer without the need for mechanical components. The temporal resolution of the Mueller matrix measurement is 2 s using LCVRs [Lóp14] and 11 µs using PEMs [Zha20]. However, LCVRs and PEMs require more complicated calibration and a stable environment.

The retroreflector is a key component for retroreflex ellipsometry. The simulation and experimental results show that the retroreflector is nearly ideal but the intensity is low (< 5%). It is also possible to optimize the retroreflector to

increase the intensity and the field of view [She22, Rib22]. Instead of traditional glass beads, metasurfaces can be used for a high-performance retroreflector [Arb17]. Metasurfaces can also be designed for many multi-functions, such as beam deflection and phase control [Zha21].

Calibration, measurement and analysis methods

Current calibration procedures use a commercial polarimeter. The accuracy of the polarimeter in the prototype is better than 0.009 for Stokes parameters. To allow more accurate Stokes vectors measurements, every element in the polarimeter must be calibrated to reduce the first- and second-order system errors [Bro10]. Shot noise, thermal noise and dark noise can also be calibrated to decrease the incidence of random errors [Jia22].

The proposed measurement methods use a single measurement but it is also possible to measure samples at multiple angles. Measurement at multiple angles gives more information about unknown parameters [Woo99]. For a three-phase system, the reflectance is also used to calculate the film thicknesses [Kih92]. By using ellipsometric parameters and reflectance, three unknown parameters can be determined.

The data analysis for Mueller matrices assumes no depolarization. However, surface scattering, variation in the angle of incidence and backside reflection induce depolarization, which increases the measurement error [Fuj07]. For depolarization, decomposition methods for Mueller Matrices are then used to derive the physical Mueller matrices or to evaluate the diattenuation, retardation, depolarization and polarizance properties of the measured Mueller Matrices [Gar13].

Opportunities for future research and applications

Section 5.3 determines the effect of the spot size. The prototype uses a collimated beam with a post size of 2 mm for measurements. Focusing optics can be used to reduce the spot size to the submicron level. A smaller spot size induces less uncertainty in the measurements but the angle of incidence

of the focusing beam varies with the position of the objective lens. Variation in the angle of incidence causes depolarization so the focusing lens must also be compensated, especially for a high NA objective lens [Liu23]. The retroreflector can also be used for imaging ellipsometry [Neg20, Neg23]. The imaging sensor acts as an array of photodiodes and multiple points can be measured simultaneously so measurements are faster and the resolution is significantly increased.

Only optically isotropic materials have been used for retroreflex ellipsometry. Optically anisotropic materials are also important in many fields for the detection of stress-induced birefringence in plastics and for the determination of PET (Polyethylene Terephthalate) films. With the exception of refractive index or film thickness measurements, retroreflex ellipsometry can be used for remote sensing [Che21c], biosensing [Che23b] and object tracking [Jeo21]. Polarization ray tracing can be used for inverse rendering [Sha22] or object detection [Kal20] for transparent objects.

Bibliography

[Ait01] Aitken, D. K. and Hough, J. H.: "Spectral Modulation, or Ripple, in Retardation Plates for Linear and Circular Polarization". In: *Publications of the Astronomical Society of the Pacific* 113.788 (2001), pp. 1300–1305. doi: 10.1086/323356 (cit. on p. 122).

[Ale89] Alexander, S.; Hellemans, L.; Marti, O.; Schneir, J.; Elings, V.; Hansma, P. K.; Longmire, Matt and Gurley, John: "An atomic-resolution atomic-force microscope implemented using an optical lever". In: *Journal of Applied Physics* 65.1 (1989), pp. 164–167. doi: 10.1063/1.342563 (cit. on p. 16).

[An03] An, Ilsin; Lee, Jaeho; Bang, Kyoung-Yoon; Kim, Ok-Kyung and Oh, Hye-Keun: "A Single Zone Azimuth Calibration for Rotating Compensator Multichannel Ellipsometry". In: *Japanese Journal of Applied Physics* 42.5R (2003), p. 2872. doi: 10.1143/JJAP.42.2872 (cit. on p. 18).

[An93] An, Ilsin; Nguyen, Hien V.; Heyd, A. R. and Collins, R. W.: "Simultaneous Real Time Spectroscopic Ellipsometry and Reflectance for Monitoring Semiconductor and Thin Film Preparation". In: *MRS Proceedings* 324 (1993), p. 799. doi: 10.1557/PROC-324-33 (cit. on p. 80).

[Arb17] Arbabi, Amir; Arbabi, Ehsan; Horie, Yu; Kamali, Seyedeh Mahsa and Faraon, Andrei: "Planar metasurface retroreflector". In: *Nature Photonics* 11.7 (2017), pp. 415–420. doi: 10.1038/nphoton.2017.96 (cit. on p. 139).

[Art14] Arteaga, Oriol and Kuntman, Ertan: "Beyond polarization microscopy: Mueller matrix microscopy with frequency demodulation". In: ed. by Chenault, David B. and Goldstein, Dennis H. SPIE Proceedings. SPIE, 2014, 90990R. doi: 10.1117/12.2053336 (cit. on pp. 15, 17).

[Arw98] Arwin, H.: "Spectroscopic ellipsometry and biology: recent developments and challenges". In: *Thin Solid Films* 313-314 (1998), pp. 764–774. doi: 10.1016/S0040-6090(97)00993-0 (cit. on p. 2).

[Asp71] Aspnes, D. E. and Studna, A. A.: "Geometrically exact ellipsometer alignment". In: *Applied optics* 10.5 (1971), pp. 1024–1030. doi: 10.1364/AO.10.001024 (cit. on p. 18).

[Azz77] Azzam, R.M.A.: "Return-path Ellipsometry and a Novel Normal-incidence Null Ellipsometer (NINE)". In: *Optica Acta: International Journal of Optics* 24.10 (1977), pp. 1039–1049. doi: 10.1080/713819411 (cit. on p. 16).

[Azz86] Azzam, R. M. A.: "Relationship between the p and s Fresnel reflection coefficients of an interface independent of angle of incidence". In: *JOSA A* 3.7 (1986), pp. 928–929. doi: 10.1364/JOSAA.3.000928 (cit. on p. 81).

[Azz87] Azzam, Rasheed Mohammed Abdel-Gawad and Bashara, Nicholas Mitchell: Ellipsometry and polarized light. 4. impression, paperback ed. North-Holland personal library. Amsterdam: Elsevier, 1987 (cit. on pp. 25, 33, 82, 97).

[Bee66] Beer, R. and Marjaniemi, D.: "Wavefronts and construction tolerances for a cat's-eye retroreflector". In: *Applied optics* 5.7 (1966), pp. 1191–1198. doi: 10.1364/AO.5.001191 (cit. on p. 56).

[Bor16] Born, Max; Wolf, Emil and Bhatia, Avadh Behari: Principles of optics: Electromagnetic theory of propagation, interference and diffraction of light. 7th ed., 11th reprinting. Cambridge: Cambridge Univ. Press, 2016 (cit. on pp. 25, 34).

[Bro10] Broch, Laurent; En Naciri, Aotmane and Johann, Luc: "Second-order systematic errors in Mueller matrix dual rotating compensator ellipsometry". In: *Applied optics* 49.17 (2010), pp. 3250–3258. doi: 10.1364/AO.49.003250 (cit. on p. 139).

[Che20] Chen, Chia-Wei; Hartrumpf, Matthias; Längle, Thomas and Beyerer, Jürgen: "Retroreflex ellipsometry for isotropic substrates with nonplanar surfaces". In: *Journal of Vacuum Science & Technology B, Nanotechnology and Microelectronics: Materials, Processing, Measurement, and Phenomena* 38.1 (2020), p. 014005. doi: 10.1116/1.5121854 (cit. on pp. 7, 8, 22).

[Che21a] Chen, Chao; Chen, Xiuguo; Wang, Cai; Sheng, Sheng; Song, Lixuan; Gu, Honggang and Liu, Shiyuan: "Imaging Mueller matrix ellipsometry with sub-micron resolution based on back focal plane scanning". In: *Optics Express* 29.20 (2021), pp. 32712–32727. doi: 10.1364/OE.439941 (cit. on p. 15).

[Che21b] Chen, Chia-Wei; Hartrumpf, Matthias; Längle, Thomas and Beyerer, Jürgen: "Analytical determination of the complex refractive index and the incident angle of an optically isotropic substrate by ellipsometric parameters and reflectance". In: *Applied optics* 60.22 (2021), F33–F38. doi: 10.1364/AO.423793 (cit. on p. 7).

[Che21c] Chen, Chia-Wei; Hartrumpf, Matthias; Längle, Thomas and Beyerer, Jürgen: "Sensitivity enhanced roll-angle sensor by means of a quarter-waveplate". In: *tm - Technisches Messen* 88.s1 (2021), s48–s52. doi: 10.1515/teme-2021-0069 (cit. on p. 140).

[Che23a] Chen, Chia-Wei; Hartrumpf, Matthias; Längle, Thomas and Beyerer, Jürgen: "Retroreflex ellipsometry for

isotropic three-phase systems with nonplanar surfaces". In: *Thin Solid Films* 769 (2023), p. 139732. DOI: 10.1016/j.tsf.2023.139732 (cit. on pp. 7, 8, 23).

[Che23b] Chen, Chia-Wei; Hartrumpf, Matthias; Längle, Thomas and Beyerer, Jürgen: "Sensitivity enhanced glucose sensing by return-path Mueller matrix ellipsometry". In: *OCM 2023 - Optical Characterization of Materials : Conference Proceedings*. Ed. by Beyerer, Jürgen; Längle, Thomas and Heizmann, Michael. Karlsruher Institut für Technologie (KIT), 2023, pp. 119–128 (cit. on p. 140).

[Chi18] Chipman, Russell A.; Young, Garam and Lam, Wai Sze Tiffany: Polarized Light and Optical Systems. Optical Sciences and Applications of Light Ser. Milton: Chapman and Hall/CRC, 2018 (cit. on pp. 25, 40, 43, 50, 121).

[Coh88] Cohn, R. F.; Wagner, J. W. and Kruger, J.: "Dynamic imaging microellipsometry: theory, system design, and feasibility demonstration". In: *Applied optics* 27.22 (1988), pp. 4664–4671. DOI: 10.1364/AO.27.004664 (cit. on p. 15).

[Del02] Delgado, M. and Delgado, E.: "Optical constants found by reflectance equations". In: *Optik* 113.1 (2002), pp. 35–38. DOI: 10.1078/0030-4026-00114 (cit. on p. 80).

[DIN 5098918] Ellipsometrie - Teil 1: Grundlagen; Text Deutsch und Englisch. Berlin: DIN Deutsches Institut für Normung e. V., 2018. DOI: 10.31030/2799141 (cit. on p. 25).

[DIN 5098921] Ellipsometrie - Teil 2: Modell Volumenmaterial; Text Deutsch und Englisch. Berlin: DIN Deutsches Institut für Normung e. V., 2021. DOI: 10.31030/3231854 (cit. on p. 25).

[DIN 5098922] Ellipsometrie - Teil 3: Modell transparente Einfachschicht; Text Deutsch und Englisch. DIN Deutsches Institut für Normung e. V., 2022. DOI: 10.31030/3319666 (cit. on p. 25).

[Duw19] Duwe, Matthias; Quast, Jan-Henrik; Schneider, Stefan; Fischer, Daniel and Beck, Uwe: "Thin-film metrology of tilted and curved surfaces by imaging Mueller-matrix ellipsometry". In: *Journal of Vacuum Science & Technology B, Nanotechnology and Microelectronics: Materials, Processing, Measurement, and Phenomena* 37.6 (2019), p. 062908. DOI: 10.1116/1.5122757 (cit. on pp. 16, 18, 19, 98).

[Duw22] Duwe, Matthias: "METHOD FOR DETERMINING PROPERTIES OF A SAMPLE BY ELLIPSOMETRY". US2022065774 (A1). 2022 (cit. on p. 19).

[Eas96] Easwarakhanthan, T. and Ravelet, S.: "Numerical calibration of the angle of incidence in ellipsometers". In: *Measurement Science and Technology* 7.5 (1996), p. 768. DOI: 10.1088/0957-0233/7/5/008 (cit. on pp. 98, 100).

[Fek98] Feke, G. D.; Snow, D. P.; Grober, R. D.; Groot, P. J. de and Deck, L.: "Interferometric back focal plane microellipsometry". In: *Applied optics* 37.10 (1998), pp. 1796–1802. DOI: 10.1364/AO.37.001796 (cit. on p. 13).

[Fu95] Fu, H.; Goodman, T.; Sugaya, S.; Erwin, J. K. and Mansuripur, M.: "Retroreflecting ellipsometer for measuring the birefringence of optical disk substrates". In: *Applied Optics* 34.1 (1995), pp. 31–39. DOI: 10.1364/AO.34.000031 (cit. on p. 17).

[Fuj07] Fujiwara, Hiroyuki: Spectroscopic ellipsometry: Principles and applications. Chichester, England and Hoboken, NJ: John Wiley & Sons, 2007. DOI: 10.1002/9780470060193 (cit. on pp. 1, 25, 40, 48, 55, 80, 139).

[Fuj17] Fujita, Kazuaki; Kuramoto, Naoki; Azuma, Yasushi; Mizushima, Shigeki and Fujii, Kenichi: "Surface Layer Analysis of a 28 Si-Enriched Sphere Both in Vacuum and in Air by Ellipsometry". In: *IEEE Transactions on Instrumentation and Measurement* 66.6 (2017), pp. 1283–1288. DOI: 10.1109/TIM.2016.2634640 (cit. on p. 3).

[Gar13] Garcia-Caurel, Enric; Ossikovski, Razvigor; Foldyna, Martin; Pierangelo, Angelo; Drévillon, Bernard and Martino, Antonello de: "Advanced Mueller Ellipsometry Instrumentation and Data Analysis". In: *Ellipsometry at the Nanoscale*. Ed. by Losurdo, Maria and Hingerl, Kurt. Berlin, Heidelberg: Springer Berlin Heidelberg, 2013, pp. 31–143. doi: 10.1007/978-3-642-33956-1_2 (cit. on p. 139).

[Gho10] Ghosh, Abhijeet; Chen, Tongbo; Peers, Pieter; Wilson, Cyrus A. and Debevec, Paul: "Circularly polarized spherical illumination reflectometry". In: *ACM Transactions on Graphics (TOG)* 29.6 (2010), p. 162. doi: 10.1145/1866158.1866163 (cit. on pp. 80, 91).

[Gra22] Graeupner, Paul; Kuerz, Peter; Stammler, Thomas; van Schoot, Jan and Stoeldraijer, Judon: "EUV optics: status, outlook and future". In: *Optical and EUV Nanolithography XXXV*. Ed. by Lio, Anna and Burkhardt, Martin. SPIE, 2022, p. 3. doi: 10.1117/12.2614778 (cit. on p. 3).

[Hab98] Haberland, K.; Hunderi, O.; Pristovsek, M.; Zettler, J.-T. and Richter, W.: "Ellipsometric and reflectance-anisotropy measurements on rotating samples". In: *Thin Solid Films* 313-314 (1998), pp. 620–624. doi: 10.1016/S0040-6090(97)00897-3 (cit. on p. 17).

[Hag80] Hague, P. S.: "Recent developments in instrumentation in ellipsometry". In: *Surface Science* 96.1-3 (1980), pp. 108–140. doi: 10.1016/0039-6028(80)90297-6 (cit. on p. 53).

[Han06] Han, Chien-Yuan and Chao, Yu-Faye: "Photoelastic modulated imaging ellipsometry by stroboscopic illumination technique". In: *Review of Scientific Instruments* 77.2 (2006), p. 023107. doi: 10.1063/1.2173027 (cit. on p. 15).

[Han09] Han, Chien-Yuan; Lee, Zhen-You and Chao, Yu-Faye: "Determining thickness of films on a curved substrate by use

of ellipsometric measurements". In: *Applied Optics* 48.17 (2009), p. 3139. DOI: 10.1364/AO.48.003139 (cit. on p. 18).

[Har13] HARKER, Matthew and O'LEARY, Paul: "Direct regularized surface reconstruction from gradients for Industrial Photometric Stereo". In: *Computers in Industry* 64.9 (2013), pp. 1221–1228. DOI: 10.1016/j.compind.2013.03.013 (cit. on p. 133).

[Har17] HARTRUMPF, Matthias and NEGARA, Christian: "Configurable retro-reflective sensor system for the improved characterization of the properties of a sample". WO/2017/207681. 2017 (cit. on pp. 17, 22).

[Har20] HARTRUMPF, Matthias; CHEN, Chia-Wei; LÄNGLE, Thomas and BEYERER, Jürgen: "Ellipsometric inline inspection of dielectric substrates with nonplanar surfaces". In: *tm - Technisches Messen* 87.6 (2020), pp. 383–391. DOI: 10.1515/teme-2019-0097 (cit. on pp. 7, 80).

[Haz83] HAZEBROEK, H. F. and VISSER, W. M.: "Automated laser interferometric ellipsometry and precision reflectometry". In: *Journal of Physics E: Scientific Instruments* 16.7 (1983), p. 654. DOI: 10.1088/0022-3735/16/7/022 (cit. on pp. 80, 83, 84, 87–89).

[Hei15] HEIMSATH, A.; SCHMID, T. and NITZ, P.: "Angle Resolved Specular Reflectance Measured with VLABS". In: *Energy Procedia* 69 (2015), pp. 1895–1903. DOI: 10.1016/j.egypro.2015.03.173 (cit. on p. 89).

[Hil11] HILFIKER, J. N.: "In situ spectroscopic ellipsometry (SE) for characterization of thin film growth". In: *In situ characterization of thin film growth*. Ed. by KOSTER, Gertjan and RIJNDERS, Guus. Woodhead Publishing Series in Electronic and Optical Materials. Philadelphia, PA: Woodhead Pub, 2011, pp. 99–151. DOI: 10.1533/9780857094957.2.99 (cit. on p. 2).

[Hol96] Holzapfel, Wolfgang; Neuschaefer-Rube, Ulrich and Doberitzsch, Jochen: "Ellipsometric topometry for technical surfaces". In: ed. by Yoshizawa, Toru and Yokota, Hideshi. SPIE Proceedings. SPIE, 1996, pp. 172–175. doi: 10.1117/12.246211 (cit. on p. 14).

[Jeo21] Jeong, Hyo Bin; Park, Jong-Kyu; Kim, Daewook and Joo, Ki-Nam: "Polarized imaging interpreter for simultaneous clocking metrology of multiple objects". In: *Optics Letters* 46.19 (2021), pp. 4992–4995. doi: 10.1364/OL.439614 (cit. on p. 140).

[Jia22] Jiang, Zhou; Zhang, Song; Liu, Jiaming; Li, Qi; Jiang, Hao and Liu, Shiyuan: "Error Analysis for Repeatability Enhancement of a Dual-Rotation Mueller Matrix Ellipsometer". In: *Frontiers in Physics* 9 (2022). doi: 10.3389/fphy.2021.820552 (cit. on p. 139).

[Jin21] Jin, Lianhua; Kondoh, Eiichi; Iizuka, Yuki; Otake, Motoyuki and Gelloz, Bernard: "Lateral ellipsometry resolution for imaging ellipsometry measurement". In: *Japanese Journal of Applied Physics* 60.5 (2021), p. 058003. doi: 10.35848/1347-4065/abf5ac (cit. on p. 15).

[Jin96] Jin, Gang; Jansson, Roger and Arwin, Hans: "Imaging ellipsometry revisited: Developments for visualization of thin transparent layers on silicon substrates". In: *Review of Scientific Instruments* 67.8 (1996), pp. 2930–2936. doi: 10.1063/1.1147074 (cit. on p. 15).

[Joh11] Johs, Blaine and He, Ping: "Substrate wobble compensation for in situ spectroscopic ellipsometry measurements". In: *Journal of Vacuum Science & Technology B, Nanotechnology and Microelectronics: Materials, Processing, Measurement, and Phenomena* 29.3 (2011), p. 03C111. doi: 10.1116/1.3555332 (cit. on pp. 17, 19, 73, 75).

[Joh93] Johs, Blaine: "Regression calibration method for rotating element ellipsometers". In: *Thin Solid Films* 234.1-2 (1993), pp. 395–398. doi: 10.1016/0040-6090(93)90293-X (cit. on p. 18).

[Jon41] Jones, R. Clark: "A New Calculus for the Treatment of Optical SystemsI Description and Discussion of the Calculus". In: *Journal of the Optical Society of America* 31.7 (1941), p. 488. doi: 10.1364/JOSA.31.000488 (cit. on p. 33).

[Kaj11] Kajihara, Yosuke; Fukuzawa, Kenji; Itoh, Shintaro and Zhang, Hedong: "Real-Time Visualization of a Shearing Nanometer-Thick Lubricant Film by Two-Stage Imaging Ellipsometric Microscopy". In: *IEEE Transactions on Magnetics* 47.10 (2011), pp. 3441–3444. doi: 10.1109/TMAG.2011.2158574 (cit. on p. 16).

[Kal07] Kalibjian, Ralph: "Output polarization states of a corner cube reflector irradiated at non-normal incidence". In: *Optics & Laser Technology* 39.8 (2007), pp. 1485–1495. doi: 10.1016/j.optlastec.2007.01.006 (cit. on p. 56).

[Kal20] Kalra, Agastya; Taamazyan, Vage; Rao, Supreeth Krishna; Venkataraman, Kartik; Raskar, Ramesh and Kadambi, Achuta: "Deep Polarization Cues for Transparent Object Segmentation". In: *2020 IEEE/CVF Conference on Computer Vision and Pattern Recognition (CVPR)*. IEEE, 2020, pp. 8599–8608. doi: 10.1109/CVPR42600.2020.00863 (cit. on p. 140).

[Kih92] Kihara, Tami and Yokomori, Kiyoshi: "Refractive-index and thickness measurements for an anisotropic film by S- and P-polarized reflectances". In: International Society for Optics and Photonics, 1992, pp. 259–268. doi: 10.1117/12.138796. url: https://www.spiedigitallibrary.org/conference-proceedings-of-spie/1746/0000/Refractive-index-and-thickness-measurements-for-an-anisotropic-film-by/10.1117/12.138796.full (cit. on p. 139).

[Kot09] Kotenev, V. A. and Tsivadze, A. Yu.: "Laser-ellipsometric monitoring of corrosive attack". In: *Protection of Metals and Physical Chemistry of Surfaces* 45.4 (2009), pp. 472–486. doi: 10.1134/S2070205109040170 (cit. on p. 2).

[Kre11] Krepelka, Jaromir: Analysis of ellipsometric data obtained from curved surfaces. 2011. doi: 10.48550/arXiv.1109.0892 (cit. on pp. 20, 105).

[Lam06] Lamminpää, Antti; Nevas, Saulius; Manoocheri, Farshid and Ikonen, Erkki: "Characterization of thin films based on reflectance and transmittance measurements at oblique angles of incidence". In: *Applied optics* 45.7 (2006), pp. 1392–1396. doi: 10.1364/AO.45.001392 (cit. on p. 89).

[Lee05] Lee, Kan Yan and Chao, Yu Faye: "The Ellipsometric Measurements of a Curved Surface". In: *Japanese Journal of Applied Physics* 44.7L (2005), p. L1015. doi: 10.1143/JJAP.44.L1015 (cit. on p. 18).

[Leo03] Leonhardt, K.; Droste, U. and Tiziani, H. J.: "Interferometry for Ellipso-Height-Topometry – Part 1: Coherence scanning on the base of spacial coherence". In: *Optik* 113.12 (2003), pp. 513–519. doi: 10.1078/0030-4026-00200 (cit. on p. 14).

[Leo91] Leonhardt, K.; Jordan, H.-J and Tiziani, H. J.: "Micro-Ellipso-Height-Profilometry". In: *Optics Communications* 80.3-4 (1991). doi: 10.1016/0030-4018(91)90251-8 (cit. on p. 14).

[Leo98] Leonhardt, K.; Droste, U. and Tiziani, H. J.: "Topometry for locally changing materials". In: *Optics Letters* 23.22 (1998), p. 1772. doi: 10.1364/OL.23.001772 (cit. on p. 14).

[Li16] Li, Weiqi; Jiang, Hao; Zhang, Chuanwei; Chen, Xiuguo; Gu, Honggang and Liu, Shiyuan: "Characterization of curved surface layer by Mueller matrix ellipsometry". In: *Journal of Vacuum Science & Technology B, Nanotechnology*

and Microelectronics: Materials, Processing, Measurement, and Phenomena 34.2 (2016), p. 020602. DOI: 10.1116/1.4943952 (cit. on pp. 18, 19, 98).

[Li19] Li, Yahong; Zhao, Yu; Yan, Li; He, Wenjun and Fu, Yuegang: "Polarization analysis of wide-viewing-angle retroreflector based on 3D coherency polarization calculus". In: *AOPC 2019: Optical Sensing and Imaging Technology*. Ed. by Gong, HaiMei; Greivenkamp, John E.; Tanida, Jun; Jiang, Yadong; Lu, Jin and Liu, Dong. SPIE, 2019, p. 85. DOI: 10.1117/12.2545499 (cit. on pp. 18, 56, 57, 59).

[Liu16] Liu, Yeng-Cheng; Lo, Yu-Lung and Liao, Chia-Chi: "Compensation of non-ideal beam splitter polarization distortion effect in Michelson interferometer". In: *Optics Communications* 361 (2016), pp. 153–161. DOI: 10.1016/j.optcom.2015.09.099 (cit. on pp. 75, 76, 98).

[Liu19] Liu, Jiamin; Lin, Jianbin; Jiang, Hao; Gu, Honggang; Chen, Xiuguo; Zhang, Chuanwei; Liao, Guanglan and Liu, Shiyuan: "Characterization of dielectric function for metallic thin films based on ellipsometric parameters and reflectivity". In: *Physica Scripta* 94.8 (2019), p. 085802. DOI: 10.1088/1402-4896/ab1606 (cit. on p. 80).

[Liu23] Liu, Jiamin; Jiang, Zhou; Zhang, Song; Huang, Tao; Jiang, Hao and Liu, Shiyuan: "Calibration of polarization effects for the focusing lens pair in a micro-spot Mueller matrix ellipsometer". In: *Thin Solid Films* 766 (2023), p. 139656. DOI: 10.1016/j.tsf.2022.139656 (cit. on p. 140).

[Liz13] Lizana, A.; Foldyna, M.; Stchakovsky, M.; Georges, B.; Nicolas, D. and Garcia-Caurel, E.: "Enhanced sensitivity to dielectric function and thickness of absorbing thin films by combining total internal reflection ellipsometry with standard ellipsometry and reflectometry". In: *Journal of Physics D: Applied Physics* 46.10 (2013), p. 105501. DOI: 10.1088/0022-3727/46/10/105501 (cit. on p. 80).

[Lóp14] López-Téllez, J. M. and Bruce, N. C.: "Mueller-matrix polarimeter using analysis of the nonlinear voltage-retardance relationship for liquid-crystal variable retarders". In: *Applied optics* 53.24 (2014), pp. 5359–5366. DOI: 10.1364/AO.53.005359 (cit. on p. 138).

[Löp15] Löper, Philipp; Stuckelberger, Michael; Niesen, Bjoern; Werner, Jérémie; Filipič, Miha; Moon, Soo-Jin; Yum, Jun-Ho; Topič, Marko; Wolf, Stefaan de and Ballif, Christophe: "Complex Refractive Index Spectra of CH3NH3PbI3 Perovskite Thin Films Determined by Spectroscopic Ellipsometry and Spectrophotometry". In: *The journal of physical chemistry letters* 6.1 (2015), pp. 66–71. DOI: 10.1021/jz502471h (cit. on p. 80).

[Lös79] Löschke, K.: "Microscopy with an ellipsometric arrangement". In: *Kristall und Technik* 14.6 (1979), pp. 717–720. DOI: 10.1002/crat.19790140616 (cit. on p. 15).

[May93] Mayer, J. Rene: "Polarization optics design for a laser tracking triangulation instrument based on dual-axis scanning and a retroreflective target". In: *Optical Engineering* 32.12 (1993), pp. 3316–3327. DOI: 10.1117/12.151296 (cit. on p. 56).

[Men16] Meng, Fangfang; Chen, Kun; Zhou, Tian; Wu, Tao; Wei, Haoyun and Li, Yan: "Point-specific self-calibration for improved characterization of thickness distribution". In: *Optical Engineering* 55.8 (2016), p. 084102. DOI: 10.1117/1.OE.55.8.084102 (cit. on p. 18).

[Neg20] Negara, Christian; Längle, Thomas and Beyerer, Jürgen: "Imaging ellipsometry for curved surfaces". In: *Journal of Vacuum Science & Technology B, Nanotechnology and Microelectronics: Materials, Processing, Measurement, and Phenomena* 38.1 (2020), p. 014016. DOI: 10.1116/1.5129654 (cit. on pp. 18, 20, 22, 140).

[Neg23] Negara, Christian Emanuel: Abbildende Ellipsometrie mit Lichtwegumkehrung für die optische Charakterisierung von gekrümmten Oberflächen. 2023. doi: 10.5445/KSP/1000158762 (cit. on pp. 57, 140).

[Neu03] Neuschaefer-Rube, U.; Holzapfel, W. and Wirth, F.: "Surface measurement applying focusing reflection ellipsometry: Configurations and error treatment". In: *Measurement* 33.2 (2003), pp. 163–171. doi: 10.1016/S0263-2241(02)00059-3 (cit. on p. 19).

[OBr36] O'Bryan, H. M.: "The Optical Constants of Several Metals in Vacuum*". In: *JOSA* 26.3 (1936), pp. 122–127. doi: 10.1364/JOSA.26.000122 (cit. on p. 16).

[Ots13] Otsuki, Soichi; Murase, Norio and Kano, Hiroshi: "Back focal plane microscopic ellipsometer with internal reflection geometry". In: *Optics Communications* 294 (2013), pp. 24–28. doi: 10.1016/j.optcom.2012.12.013 (cit. on p. 13).

[Ped82] Pedinoff, M. E. and Stafsudd, O. M.: "Multiple angle ellipsometric analysis of surface layers and surface layer contaminants". In: *Applied optics* 21.3 (1982), pp. 518–521. doi: 10.1364/AO.21.000518 (cit. on p. 2).

[Pil21] Pillarz, Marc; Freyberg, Axel von; Stöbener, Dirk and Fischer, Andreas: "Gear Shape Measurement Potential of Laser Triangulation and Confocal-Chromatic Distance Sensors". In: *Sensors (Basel, Switzerland)* 21.3 (2021). doi: 10.3390/s21030937 (cit. on p. 115).

[Rib22] Ribeiro, Laura Goncalves; Suominen, Olli J.; Bates, Philip; Peltonen, Sari; Morales, Emilio Ruiz and Gotchev, Atanas: Design and manufacturing of an optimized retro reflective marker for photogrammetric pose estimation in ITER. 2022. doi: 10.48550/arXiv.2205.05486 (cit. on p. 139).

[Rie79] Riedling, K.: "Evaluation of adjustment data for simple ellipsometers". In: *Thin Solid Films* 61.3 (1979), pp. 335–340. doi: 10.1016/0040-6090(79)90478-4 (cit. on p. 18).

[Ris02] Ristau, Detlev; Günster, Stefan; Bosch, Salvador; Duparré, Angela; Masetti, Enrico; Ferré-Borrull, Josep; Kiriakidis, George; Peiró, Francesca; Quesnel, Etienne and Tikhonravov, Alexander: "Ultraviolet optical and microstructural properties of MgF2 and LaF3 coatings deposited by ion-beam sputtering and boat and electron-beam evaporation". In: *Applied optics* 41.16 (2002), pp. 3196–3204. doi: 10.1364/AO.41.003196 (cit. on p. 132).

[Sar20] Sarkin, Ali Samet; Ekren, Nazmi and Sağlam, Şafak: "A review of anti-reflection and self-cleaning coatings on photovoltaic panels". In: *Solar Energy* 199 (2020), pp. 63–73. doi: 10.1016/j.solener.2020.01.084 (cit. on p. 3).

[See96] See, C. W.; Somekh, M. G. and Holmes, R. D.: "Scanning optical microellipsometer for pure surface profiling". In: *Applied optics* 35.34 (1996), pp. 6663–6668. doi: 10.1364/AO.35.006663 (cit. on p. 13).

[Seg03] Segre, Sergio E. and Zanza, Vincenzo: "Mueller calculus of polarization change in the cube-corner retroreflector". In: *Journal of the Optical Society of America A* 20.9 (2003), p. 1804. doi: 10.1364/JOSAA.20.001804 (cit. on p. 56).

[Sha19] Shan, Yao; Hu, Guohang; Grilli, Maria Luisa; He, Hongbo; Zhu, Meiping; Zhao, Yuanan and Shao, Jianda: "Measuring ultrathin metal coatings using SPR spectroscopic ellipsometry with a prism-dielectric-metal-liquid configuration". In: *Optics Express* 27.6 (2019), pp. 7912–7921. doi: 10.1364/OE.27.007912 (cit. on p. 3).

[Sha22] Shao, Mingqi; Xia, Chongkun; Duan, Dongxu and Wang, Xueqian: Polarimetric Inverse Rendering for Transparent Shapes Reconstruction. 2022. doi: 10.48550/arXiv.2208.11836 (cit. on p. 140).

[She22] Sheng, Quan et al.: "Enhancing the field of view of cat-eye retroreflectors by simply matching the mirror radius of curvature and the lens focal length". In: *Results in Physics* 37 (2022), p. 105558. doi: 10.1016/j.rinp.2022.105558 (cit. on p. 139).

[Shi97] Shirai, Hajime; Arai, Takeshi and Nakamura Takuya: "Control of the initial stage of nanocrystallite silicon growth monitored by in-situ spectroscopic ellipsometry". In: *Applied Surface Science* 113-114 (1997), pp. 111–115. doi: 10.1016/S0169-4332(96)00801-X (cit. on p. 2).

[Shu62] Shurcliff, William A.: Polarized Light: Production and Use. Cambridge, Mass.: Harvard University Press, 1962 (cit. on p. 38).

[Smi02] Smith, Matthew H.: "Optimization of a dual-rotating-retarder Mueller matrix polarimeter". In: *Applied Optics* 41.13 (2002), p. 2488. doi: 10.1364/AO.41.002488 (cit. on p. 138).

[Sta08] Stabo-Eeg, Frantz; Kildemo, Morten; Nerbo, Ingar and Lindgren, Mikael: "Well-conditioned multiple laser Mueller matrix ellipsometer". In: *Optical Engineering* 47.7 (2008), p. 073604. doi: 10.1117/1.2957047 (cit. on p. 138).

[Ste80] Stevens, D. W.: "A perpendicular-incidence microellipsometer". In: *Surface Science* 96.1-3 (1980), pp. 174–201. doi: 10.1016/0039-6028(80)90302-7 (cit. on p. 12).

[Ste85] Steel, W. H.: "Polarization-preserving retroreflectors". In: *Applied Optics* 24.21 (1985), pp. 3433–3434. doi: 10.1364/AO.24.003433 (cit. on p. 56).

[Sto52] Stokes, George Gabriel: "XXX. On the change of refrangibility of light". In: *Philosophical Transactions of the Royal Society of London* 142 (1852), pp. 463–562. doi: 10.1098/rstl.1852.0022 (cit. on p. 37).

[Stu00] Stutzman, Brooke S.; Huang, Hsu-Ting and Terry, Fred L.: "Two-channel spectroscopic reflectometry for in situ monitoring of blanket and patterned structures during reactive ion etching". In: *Journal of Vacuum Science & Technology B: Microelectronics and Nanometer Structures* 18.6 (2000), p. 2785. doi: 10.1116/1.1327301 (cit. on p. 80).

[Tho20] Thomas, Matthew; Su, Rong; Groot, Peter J. de and Leach, Richard K.: "Optical topography measurement of steeply-sloped surfaces beyond the specular numerical aperture limit". In: *Optics and Photonics for Advanced Dimensional Metrology*. Ed. by Groot, Peter J. de; Leach, Richard K. and Picart, Pascal. SPIE, 2020, p. 7. doi: 10.1117/12.2554568 (cit. on p. 21).

[Tom16] Tompkins, Harland G. and Hilfiker, James N.: Spectroscopic ellipsometry: Practical application to thin film characterization. Materials characterization and analysis collection. New York: Momentum Press, 2016 (cit. on p. 2).

[Wan04] Wang, Guoliang and Arwin, Hans: "Return-path ellipsometry in gas sensing". In: *Measurement Science and Technology* 15.1 (2004), pp. 216–220. doi: 10.1088/0957-0233/15/1/030 (cit. on p. 16).

[Wat10] Watkins, Lionel R. and Shamailov, Sophie S.: "Variable angle of incidence spectroscopic autocollimating ellipsometer". In: *Applied optics* 49.16 (2010), pp. 3231–3234. doi: 10.1364/AO.49.003231 (cit. on p. 16).

[Woo99] Woollam, John A.; Johs, Blaine D.; Herzinger, Craig M.; Hilfiker, James N.; Synowicki, Ron A. and Bungay, Corey L.: "Overview of variable-angle spectroscopic ellipsometry (VASE): I. Basic theory and typical applications". In: ed. by Al-Jumaily, Ghanim A. International Society for Optics and Photonics, 1999, p. 1029402. doi: 10.1117/12.351660 (cit. on pp. 80, 139).

[Wur10] Wurstbauer, Ulrich; Röling, Christian; Wurstbauer, Ursula; Wegscheider, Werner; Vaupel, Matthias; Thiesen, Peter H. and Weiss, Dieter: "Imaging ellipsometry of graphene". In: *Applied Physics Letters* 97.23 (2010), p. 231901. DOI: 10.1063/1.3524226 (cit. on p. 15).

[Yam74] Yamamoto, Masaki: "A new type of precision ellipsometer without employing a compensator". In: *Optics Communications* 10.2 (1974), pp. 200–202. DOI: 10.1016/0030-4018(74)90054-6 (cit. on p. 16).

[Yam76] Yamaguchi, T. and Takahashi, H.: "Autocollimation-type ellipsometer for monitoring film growth through a single window". In: *Applied optics* 15.3 (1976), pp. 677–680. DOI: 10.1364/AO.15.000677 (cit. on p. 16).

[Yan00] Yang, B. and Friedsam, H.: Ray-tracing studies for a whole-viewing-angle retroreflector. 2000 (cit. on pp. 57, 59).

[Yan12] Yang, Bing-jun; Chao, Keng-hsing and Tsai, Jui-che: "Modeling of micro cat's eye retroreflectors using a matrix-based three-dimensional ray tracing technique". In: *Applied optics* 51.25 (2012), pp. 6020–6030. DOI: 10.1364/AO.51.006020 (cit. on p. 57).

[Ye07] Ye, Sang-Heon; Kim, Soo Hyun; Kwak, Yoon Keun; Cho, Hyun Mo; Cho, Yong Jai and Chegal, Won: "Angle-resolved annular data acquisition method for microellipsometry". In: *Optics Express* 15.26 (2007), pp. 18056–18065. DOI: 10.1364/OE.15.018056 (cit. on p. 13).

[Zei74] Zeidler, J. R.; Kohles, R. B. and Bashara, N. M.: "Beam deviation errors in ellipsometric measurements; an analysis". In: *Applied optics* 13.8 (1974), pp. 1938–1945. DOI: 10.1364/AO.13.001938 (cit. on p. 18).

[Zha02] Zhan, Qiwen and Leger, James R.: "Microellipsometer with radial symmetry". In: *Applied optics* 41.22 (2002), pp. 4630–4637. DOI: 10.1364/AO.41.004630 (cit. on p. 13).

[Zha10] Zhang, Ji-Tao; Li, Luo, Yan; Zhi-Yong and Wu, Xue-Jian: "Determination of Mean Thickness of an Oxide Layer on a Silicon Sphere by Spectroscopic Ellipsometry". In: *Chinese Physics Letters* 27.5 (2010), p. 050601. doi: 10.1088/0256-307X/27/5/050601 (cit. on p. 105).

[Zha12] Zhang, Ji-Tao; Wu, Xue-Jian and Li, Yan: "Mixed polarization in determining the film thickness of a silicon sphere by spectroscopic ellipsometry". In: *Chinese Physics B* 21.1 (2012), p. 010701. doi: 10.1088/1674-1056/21/1/010701 (cit. on p. 20).

[Zha18] Zhang, Song; Gu, Honggang; Liu, Jiamin; Jiang, Hao; Chen, Xiuguo; Zhang, Chuanwei and Liu, Shiyuan: "Characterization of beam splitters in the calibration of a six-channel Stokes polarimeter". In: *Journal of Optics* 20.12 (2018), p. 125606. doi: 10.1088/2040-8986/aaef27 (cit. on p. 75).

[Zha20] Zhang, Song; Jiang, Hao; Gu, Honggang; Chen, Xiuguo and Liu, Shiyuan: "High-speed Mueller matrix ellipsometer with microsecond temporal resolution". In: *Optics Express* 28.8 (2020), pp. 10873–10887. doi: 10.1364/OE.389825 (cit. on p. 138).

[Zha21] Zhang, Zhongtao; Wang, Jiafu; Zhu, Ruichao; Jia, Yuxiang; Liu, Tonghao; Yan, Mingbao; Jiang, Jinming; Li, Yongfeng; Meng, Yueyu and Qu, Shaobo: "Multifunctional full-space metasurface controlled by frequency, polarization and incidence angle". In: *Optics Express* 29.5 (2021), pp. 7544–7557. doi: 10.1364/OE.419720 (cit. on p. 139).

[Zho11] Zhou, Bin; Liu, Bingqi and Wu, Dongsheng: "Research on echo energy of 'cat-eye' target based on laser's character of polarization". In: *Proceedings of 2011 International Conference on Electronics and Optoelectronics*. IEEE, 2011, pp. V2-302-V2–305. doi: 10.1109/ICEOE.2011.6013241 (cit. on p. 57).

[Zim19] Zimmer, Alexandre; Veys-Renaux, Delphine; Broch, Laurent; Stein, Nicolas and Rocca, Emmanuel: "In situ spectroelectrochemical ellipsometry using super continuum white laser: Study of the anodization of magnesium alloy". In: *Journal of Vacuum Science & Technology B, Nanotechnology and Microelectronics: Materials, Processing, Measurement, and Phenomena* 37.6 (2019), p. 062911. DOI: 10.1116/1.5122320 (cit. on p. 138).

Own publications

[1] Chen, Chia-Wei: "An Overview of Ellipsometric Measurements for Nonplanar Surfaces". In: *Proceedings of the 2019 Joint Workshop of Fraunhofer IOSB and Institute for Anthropomatics, Vision and Fusion Laboratory. Ed.: J. Beyerer; T. Zander*. Vol. 45. Karlsruher Schriften zur Anthropomatik / Lehrstuhl für Interaktive Echtzeitsysteme, Karlsruher Institut für Technologie ; Fraunhofer-Inst. für Optronik, Systemtechnik und Bildauswertung IOSB Karlsruhe. KIT Scientific Publishing, 2019, pp. 25–38. DOI: 10.5445/IR/1000126692.

[2] Chen, Chia-Wei: "An Overview of Return-Path Ellipsometry". In: *Proceedings of the 2018 Joint Workshop of Fraunhofer IOSB and Institute for Anthropomatics, Vision and Fusion Laboratory. Ed.: J. Beyerer, M. Taphanel*. Vol. 40. Karlsruher Schriften zur Anthropomatik / Lehrstuhl für Interaktive Echtzeitsysteme, Karlsruher Institut für Technologie ; Fraunhofer-Inst. für Optronik, Systemtechnik und Bildauswertung IOSB Karlsruhe. KIT Scientific Publishing, 2019, pp. 1–10. DOI: 10.5445/IR/1000097081.

[3] Chen, Chia-Wei; Hartrumpf, Matthias; Längle, Thomas and Beyerer, Jürgen: "Measurement of ellipsometric data and surface orientations by modulated circular polarized light / Messung von ellipsometrischen Daten und Oberflächenorientierungen durch moduliertes zirkular polarisiertes Licht". In: *tm - Technisches Messen* 86.s1 (2019), pp. 32–36. DOI: 10.1515/teme-2019-0047.

[4] Chen, Chia-Wei; Hartrumpf, Matthias; Längle, Thomas and Beyerer, Jürgen: "Retroreflex ellipsometry for isotropic substrates with nonplanar surfaces". In: *Journal of Vacuum Science & Technology B,*

Nanotechnology and Microelectronics: Materials, Processing, Measurement, and Phenomena 38.1 (2020), p. 014005. DOI: 10.1116/1.5121854.

[5] HARTRUMPF, Matthias; CHEN, Chia-Wei; LÄNGLE, Thomas and BEYERER, Jürgen: "Ellipsometric inline inspection of dielectric substrates with nonplanar surfaces". In: *tm - Technisches Messen* 87.6 (2020), pp. 383–391. DOI: 10.1515/teme-2019-0097.

[6] CHEN, Chia-Wei: "Characterization of Mueller matrices in retroreflex ellipsometry". In: *Proceedings of the 2020 Joint Workshop of Fraunhofer IOSB and Institute for Anthropomatics, Vision and Fusion Laboratory. Ed.: J. Beyerer; T. Zander*. Vol. 51. Karlsruher Schriften zur Anthropomatik / Lehrstuhl für Interaktive Echtzeitsysteme, Karlsruher Institut für Technologie ; Fraunhofer-Inst. für Optronik, Systemtechnik und Bildauswertung IOSB Karlsruhe. KIT Scientific Publishing, 2021, pp. 19–32. DOI: 10.5445/IR/1000135071.

[7] CHEN, Chia-Wei; HARTRUMPF, Matthias; LÄNGLE, Thomas and BEYERER, Jürgen: "Analytical determination of the complex refractive index and the incident angle of an optically isotropic substrate by ellipsometric parameters and reflectance". In: *Applied optics* 60.22 (2021), F33–F38. DOI: 10.1364/AO.423793.

[8] CHEN, Chia-Wei; HARTRUMPF, Matthias; LÄNGLE, Thomas and BEYERER, Jürgen: "Sensitivity enhanced roll-angle sensor by means of a quarter-waveplate". In: *tm - Technisches Messen* 88.s1 (2021), s48–s52. DOI: 10.1515/teme-2021-0069.

[9] CHEN, Chia-Wei; ZHOU, Bowen; LÄNGLE, Thomas and BEYERER, Jürgen: "Robustness estimation of simple lens systems by machine learning". In: *International Optical Design Conference 2021*. Ed. by PFISTERER, Richard N.; REHN, Henning; THIBAULT, Simon and CLARK, Peter P. SPIE, 2021, p. 46. DOI: 10.1117/12.2603658.

[10] CHEN, Chia-Wei; HARTRUMPF, Matthias; LÄNGLE, Thomas and BEYERER, Jürgen: "Retroreflex ellipsometry for isotropic three-phase systems with nonplanar surfaces". In: *Thin Solid Films* 769 (2023), p. 139732. DOI: 10.1016/j.tsf.2023.139732.

[11] Chen, Chia-Wei; Hartrumpf, Matthias; Längle, Thomas and Beyerer, Jürgen: "Sensitivity enhanced glucose sensing by return-path Mueller matrix ellipsometry". In: *OCM 2023 - Optical Characterization of Materials : Conference Proceedings*. Ed. by Beyerer, Jürgen; Längle, Thomas and Heizmann, Michael. Karlsruher Institut für Technologie (KIT), 2023, pp. 119–128.

List of Figures

List of Tables